Whispering gallery modes in layered microspheres: mode structure, thermal response, and reactive sensing

by

Yanyan Zhi

A thesis submitted in partial fulfillment of the requirements for the degree of

Doctor of Philosophy

Department of Physics
University of Alberta

Abstract

This thesis focuses on the physics of the whispering gallery modes (WGMs) of silica microspheres coated with a layer of fluorescent silicon quantum dots (Si QDs). The basic theory associated with these structures was explored, and we showed how the important physical parameters such as the quality factor (Q factor), resonance wavelengths, electric field profile, and thermal properties can be straightforwardly calculated. The QD coating plays a major role in controlling each of these key parameters. The QDs also provide a fluorescent source which can couple to the WGMs of the microsphere, avoiding the complexity and fragility associated with coupling via an "evanescent" field. After a thorough discussion of the experimental issues associated with the fabrication and measurement of these structures, we next showed how the cold-cavity modes are related to the WGMs observed in the fluorescence spectrum. Then we examined theoretically the basic properties of the WGMs, their thermal response, and the sensing capabilities associated with these structures. Based on the theory, a microsphere demonstrated extreme stability against local temperature fluctuations. Finally, the refractometric sensor response of the coated microsphere devices was studied. This required the design of different fluidic environments to test the sensor response. The detection limits approached 10^{-5} refractive index units, which appeared to be limited mainly by the wavelength shift resolution of the analysis method and by mechanical drift. Finally, outstanding issues and potential future directions were discussed.

Preface

This thesis is an original work by Yanyan Zhi. Chapters 2 to 6 are slightly modified from publications listed in the Appendix. I'm the main contributor to each of the papers and did most of the experimental work. All of the co-authors in the publications contributed either to the experiment or analysis. Jan Valenta did the cryogenic temperature experiment in Chapter 3. In Chapter 5, Kyle Manchee helped with part of the sensing experiments, Josh Silverstone helped with the Fourier analysis, and Zhihong Zhang did the FDTD simulation in Figure 39. In Chapter 6 Torrey Thiessen helped with part of the sensing experiments. My supervisor Al Meldrum contributed intellectually and to the writing and experiment concept of all publications.

Acknowledgements

I owe my deepest thanks to my supervisor Al Meldrum, without whom this thesis wouldn't have been completed. Thank you for your help and guide in my academic area, and for discussions and suggestions on questions coming out of the academia. Thank you for being a great supervisor, a friend, a mentor and a family. I can't imagine a better supervisor. Whether I would stay in academia, I only hope I could be someone like you.

Thanks to the technicians in the Department of Physics, Don Mullin, Paul Zimmermann, Greg Popowich and Dave Fortin. You can always find a solution to the problems I met in the experiments, and settle them quickly.

Thanks to all my friends for their accompany. You cheer me up when I'm in a low mood. You show me how to be strong by being strong youselves.

Last, but most importantly, I would like to thank my mother and my father for letting me to be whom I am, and doing what I like. You never push me to follow others' life paths. Thanks to my brother for always supporting me in any circumstance.

Contents

List of Figures

List of Abbreviations

2D	2-dimensional
AFM	atomic force microscopy
FDTD	finite difference time domain
FSR	free spectral range
FWHM	full-width-at-half-maximum
HSQ	hydrogen silsesquioxane
HWP	half wave plate
LoC	Lab-on-a-Chip
MIBK	methyl isobutyl ketone
PL	photoluminescence
QD	quantum dot
QE	quantum efficiency
RIU	refractive index unit
RMS	root-mean-square
SD	spectral diffusion
SEM	scanning electron microscopy
Si QDs	silicon quantum dots
TE	transverse electric
TEM	transmission electron microscopy
TIR	total internal reflection
TM	transverse magnetic
WGM	whispering gallery mode

List of Symbols

α	absorption coefficient
α_{abs}	loss coefficient due to material absorption
α_{ib}	loss coefficient due to inter-band absorption
α_{mie}	loss coefficient due to Mie scattering
α_{rough}	loss coefficient due to surface roughness
χ_{nl}	roots of the spherical Bessel functions with n being the number of the root and l being the order of the function
Δf_{FSR}	free spectral range in the frequency domain
Δf_{FWHM}	full-width-at-half-maximum in the frequency domain
ϵ	dielectric constant
ϵ_0	permittivity of free space, $\epsilon_0 = 8.85418782 \times 10^{-12}\,\mathrm{F/m}$
ϵ_r	relative permittivity of a material
γ	non-resonant decay rate or round-trip loss
$\Gamma(\lambda)$	confinement factor at wavelength λ
κ	extinction coefficient or cavity decay rate or power coupling ratio
κ_{abs}	extinction coefficient due to the material absorption
λ	wavelength
λ_0	resonant wavelength
$\mathbf{B}$	magnetic flux density
$\mathbf{D}$	electric displacement
$\mathbf{E}$	electric field
$\mathbf{H}$	magnetic field
$\mathbf{J}$	current density
$\mathbf{L}$	angular momentum
$\mathcal{F}$	finesse
μ_0	permeability of free space,$\mu_0 = 1.25663706 \times 10^{-6}\,\mathrm{N}/A^2$

μ_r	relative permeability
∇	Laplace operator
ω	angular frequency
ϕ	azimuthal direction
$\Phi(\phi)$	electric field distribution in the azimuthal direction
ψ	electron (or hole) wave function
$\psi_l(x)$	l^{th}-Riccati-Bessel function of argument x
ρ	free electron density
σ	electrical conductivity
$\sigma_{abs}(R)$	absorption cross section as a function of the quantum dot radius
σ_{mie}	scattering cross section
σ_{rms}	root-mean-square roughness
τ	ringdown time or quantum dot radiative lifetime
τ_{nr}	non-radiative recombination lifetime
τ_r	radiative recombination lifetime
θ	polar direction
$\Theta(\theta)$	electric field distribution in the polar direction
$\varphi^2(r)$	field intensity at the resonator surface
$\xi_l^{(1)}(x)$	l^{th}-Riccati-Hankel function of the first kind of argument x
$\xi_l^{(2)}(x)$	l^{th}-Riccati-Hankel function of the second kind of argument x
$\xi_l'^{(1)}(x)$	derivative with respect to the argument x of the Riccati-Hankel function of the first kind
a	total radius of a microsphere with a layer of QDs or radius of a quantum dot
b	radius of a bare microsphere
c	speed of light in free space, $c = 2.99792458 \times 10^8$ m/s
d	diameter or evanescent field length

E_0	electric field
E_{1e}	lowest excited state of an electron
E_{1h}	lowest excited state of a hole
$E_{eh}(a)$	electron-hole energy difference as a function of a quantum dot radius
E_g	band gap
E^e_{nl}	quantized energy levels of an electron
E^h_{nl}	quantized energy levels of a hole
$E_{PL}(d)$	lowest electron-hole energy difference as a function of a quantum dot diameter
E_p	perturbed field within V_P
f	frequency
$f_{nm,\,l-1}$	resonant frequency for a mode with quantum numbers $(n,\ m,\ l-1)$
$f_{nm,\,l}$	resonant frequency for a mode with quantum numbers $(n,\ m,\ l)$
F_P	Purcell factor
g_0	quantum dot-photon coupling rate in the cavity
H	Hamiltonian
$h^{(1)}_l(x)$	l^{th}-order spherical Hankel functions of the first kind of argument x
$h^{(2)}_l(x)$	l^{th}-order spherical Hankel functions of the second kind of argument x
I_{max}	maximum intensity
I_{min}	minimum intensity
$Im[k_0]$	imaginary part of the wave number k_0
J	total angular momentum including spin up and down states
$j_l(x)$	l^{th}-order spherical Bessel function of the first kind of argument x
k_0	resonant wave number

k_B	the Boltzmann constant, $k_B = 1.38064881 \times 10^{-23}$ J/K
l	azimuthal number for a whispering gallery mode
L_z	angular momentum component parallel to the z axis
m	polar number for a whispering gallery mode
m_e	effective mass of an electron
m_h	effective mass of a hole
n	radial number for a whispering gallery mode
$n(r)$	refractive index distribution in the radial direction
n_1	refractive index of a microsphere
n_2	refractive index of the layer coated on the surface of a microsphere
n_3	refractive index of the surroundings outside a microsphere
n_{cavity}	refractive index of a cavity
n_{eff}	effective refractive index
n_i	refractive index of the i-th layer
n_{QD}	refractive index of a quantum dot film
p	pixel number
$P_l^m(x)$	associated Legendre functions of the first kind of degree l and order m of argument x
Q	quality factor
Q_{abs}	quality factor limited by material absorption
Q_{ib}	quality factor limited by inter-band absorption
$Q_l^m(x)$	associated Legendre functions of the second kind of degree l and order m of argument x
Q_{mie}	quality factor limited by Mie scattering
Q_{rad}	quality factor limited by radiation loss
Q_{sca}	quality factor limited by surface-roughness-induced scattering loss
Q_{total}	total quality factor

r	radial direction
$R(r)$	electric field distribution in the radial direction
$R_{QD,max}$	radius of the largest nanocrystal in the sample
$R_{QD,min}$	radius of the smallest nanocrystal in the sample
$R_{QD}(\lambda)$	radius of a nanocrystal with an emission at wavelength λ
$Re[k_0]$	real part of the wave number k_0
S	refractometric sensitivity
s	spin number
$S_l(r)$	radial field function for the TE polarization
S_{TE}	sensitivity for TE polarized modes
S_{TM}	sensitivity for TM polarized modes
t	time or thickness
$T_l(r)$	radial field function for the TM polarization
$U(r)$	potential energy in the radial direction
V	volume
V_{eff}	effective mode volume
V_I	visibility
V_p	perturbation volume
W	spontaneous emission rate
Y_{lm}	spherical harmonic function
$y_l(x)$	l^{th}-order spherical Bessel function of the second kind of argument x

1. Introduction

1.1 Whispering gallery modes

The term "whispering gallery" was apparently coined by Lord Rayleigh about a century ago [1, 2, 3] to describe certain acoustic phenomena reported in one of the upper galleries of St. Paul's Cathedral in London. Whispers at one side of the gallery could be clearly heard at the opposite side approximately 32 meters away. The effect was so striking (especially for higher-pitched sounds like birdcalls) that it prompted Lord Rayleigh to perform an investigation into the effect [1]. Using a flickering candle flame as the measurement device, he reported that the sound intensity was concentrated near the edges of the chamber, with virtually none in the center. Rayleigh used the Bessel equations to show that this result is precisely to be expected on the basis of the circular acoustic resonances of the gallery. A further consequence is that sound at the resonant frequencies is amplified, although more sophisticated equipment than that available at the time was needed to detect this. These resonances are now called the whispering gallery modes (WGMs).

This concept can also be applied to electromagnetic waves. Even prior to Lord Rayleigh's work, Gustav Mie in 1908 discussed light scattering by spherical dielectric droplets [4] using Maxwell's electromagnetic theory. This work was built on even earlier studies by Joseph John Thomson [5], Alfred Clebsch [6], Ludvig Lorenz [7, 8], and Peter Debye [9]. A more detailed history of electromagnetic scattering theory can be found in the historical works of Horvath [10] and Wriedt [11]. Possibly the first luminescence-related observations of WGMs can be traced to 1961 when Garrett et. al. [12] demonstrated solid state lasing by coupling the luminescence of Sm^{2+} into the WGMs of a CaF_2 microsphere cavity. Since then, there have been numerous studies of fluorescence WGMs in different types of microcavities [13, 14]. Much of the work has aimed toward the development of low-threshold microcavity lasers [15, 16, 17], biosensors [18, 19, 20, 21, 22, 23, 24], super resolution imaging [25], and toward fundamental studies of cavity quantum electrodynamics [26].

This thesis will look at microspheres coated with silicon quantum dots (QDs) for sensing applications. The whispering gallery modes of a QD-coated-microsphere will be investigated by comparing the photoluminescence (PL) spectrum to the "cold cavity" modes of a microsphere. Subsequently we will examine the ability of a QD-coated microsphere to act as a refractometric sensor. This will be tested by building a fluidic environment around the microsphere. Methods will be developed that enable a single QD-coated microsphere to operate in a "sensorgram" mode. Finally, various means will be explored to improve and optimize the sensor performance.

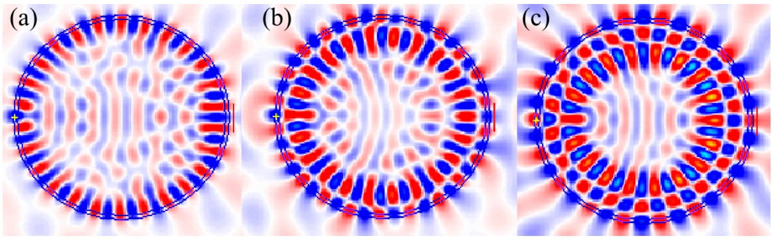

Figure 1. Simulated electric field amplitude for the equatorial TE-polarized WGMs in a 2-dimensional disk with a diameter of 3 µm. The radial and azimuthal mode numbers are (a) $n = 1$, $l = 26$; (b) $n = 2$, $l = 22$; (c) $n = 3$, $l = 18$.

1.1.1 Identification of the whispering gallery modes

The whispering gallery modes can be specified by three quantum numbers. The first one is the radial number n ($n = 1, 2, \ldots$) which represents the number of field intensity maxima in the radial direction (i.e., outward from the center of a microsphere). The azimuthal number l ($l = 0, 1, 2, \ldots$) is analogous to the azimuthal number in quantum mechanics that describes the orbital angular momentum. The "polar" number, m, can take integer values between $+l$ and $-l$. The number of intensity maxima in the polar direction is given by $l-|m|+1$ and in the equatorial direction the number of maxima is equal to $2|m|$. Thus a purely equatorial WGM has $l = |m|$, with one polar maximum and $2|m|$ intensity maxima around the circumference. The sign of m simply implies the propagation direction (e.g., a negative sign for clockwise propagation and a positive sign for counterclockwise propagation according to the usual convention).

These concepts can be well-illustrated by graphical means. Figure 1 shows the electric field distribution of a 2-dimensional (2D) disk with a diameter of 3 µm, simulated using a finite difference time domain (FDTD) software package (OmniSim from Photon Design). The color indicates the amplitude of the electric field from positive (red) to negative (blue) peak amplitude. Panels (a), (b) and (c) illustrate the first-, second-, and third-radial-order equatorial WGMs, respectively. The field extends outside the boundary to a degree that strongly depends on the radial number. Since there's no polar direction in a 2D structure, the "polar" number does not apply to a disk. The WGMs can be illustrated 3-dimensionally as well (Figure 2). An equatorial WGM with only one strong polar maximum is shown in Figure 2(a) with $l - |m| + 1 = 1$. When $l - |m| + 1 = 14$, the electric field has 14 intensity maxima in the polar direction (Figure 2(b)).

Modes with the same n and l but different m are degenerate in a perfect sphere.

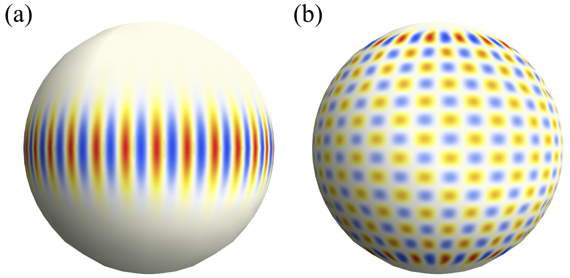

Figure 2. Calculated electric field amplitude for a 3 µm-diameter microsphere. In (a) we have $n = 1$, $l = 33$ and $m = 33$. Panel (b) shows the field for the same n and l values, but with $m = 20$. The resonant wavelength for (a) and (b) are the same (i.e., they are degenerate modes).

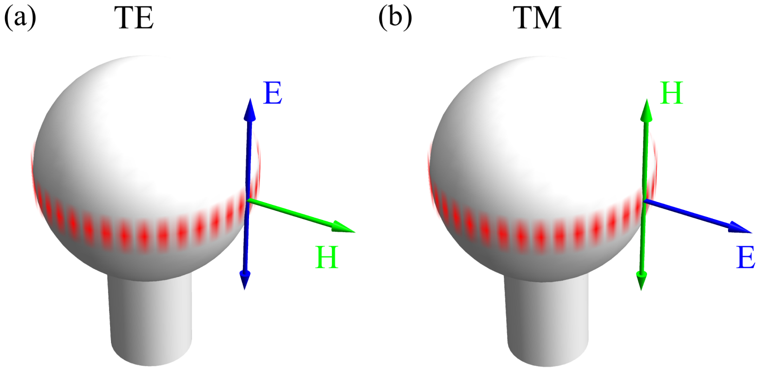

Figure 3. Diagram illustrating (a) the TE polarization, and (b) the TM polarization.

However, if the sphere is eccentric, this degeneracy is broken and modes with different m have a slightly different resonance frequency [17]. As well, scattering can break the degeneracy between the $+m$ and $-m$ modes (again, with the same n and l), a phenomenon that could potentially be used for single nanoparticle sensing applications [27].

In contrast to acoustic waves, optical WGMs have two polarizations (Figure 3). A transverse electric (TE) polarized WGM has its electric field transverse to the plane of propagation which is the equatorial plane; thus, its E-field is tangential to the interface between the microsphere and its surroundings. In the transverse magnetic (TM) case, the H-field is perpendicular to the plane of propagation and the E-field is thus normal to the interface between the dielectric microsphere and the surrounding environment (i.e., the E-field is radial). The resonant frequencies are slightly different in the two cases.

1.1.2 Derivation of electric field distribution for whispering gallery modes in a microsphere

To understand the resonant electromagnetic modes in a microsphere, we need to describe the electric field distribution associated with the cavity. For the sake of completeness, here we start with Maxwell's differential equations:

$$\nabla \cdot \mathbf{D} = \rho, \tag{1a}$$

$$\nabla \cdot \mathbf{B} = 0, \tag{1b}$$

$$\nabla \times \mathbf{E} = -\frac{\partial \mathbf{B}}{\partial t}, \tag{1c}$$

$$\nabla \times \mathbf{H} = J + \frac{\partial \mathbf{D}}{\partial t}, \tag{1d}$$

where **D** is the electric displacement, ρ is the free electron density, **B** is the magnetic flux density, **E** is the electric field, **H** is the magnetic field, **J** is the current density, t is time, and the Laplace operator, ∇, in Cartesian coordinates is:

$$\nabla = \frac{\partial}{\partial x}\hat{x} + \frac{\partial}{\partial y}\hat{y} + \frac{\partial}{\partial z}\hat{z}, \tag{2}$$

where $\hat{x}$, $\hat{y}$, and $\hat{z}$ are unit vectors in a Cartesian coordinate. We also have the relations:

$$\mathbf{J} = \sigma \mathbf{E}, \tag{3a}$$

$$\mathbf{D} = \epsilon \mathbf{E} = \epsilon_0 \epsilon_r \mathbf{E}, \tag{3b}$$

and

$$\mathbf{B} = \mu \mathbf{H} = \mu_0 \mu_r \mathbf{H}, \tag{3c}$$

where σ is the electrical conductivity, ϵ is the dielectric constant, ϵ_0 is the permittivity of free space, ϵ_r is the relative permittivity of the material, μ_0 is the permeability in free space, and μ_r is the relative permeability of the non-magnetic material. A convenient equation for the magnetic field, **H**, can be derived by using the relationships in Equations (1) and (3):

$$\begin{aligned}
\nabla\times\nabla\times\mathbf{H} &= \nabla\times(\mathbf{J}+\frac{\partial\mathbf{D}}{\partial t}) \\
&= \nabla\times\mathbf{J}+\nabla\times\frac{\partial\mathbf{D}}{\partial t} \\
&= \nabla\times(\sigma\mathbf{E})+\nabla\times\frac{\partial(\epsilon\mathbf{E})}{\partial t} \\
&= \sigma\nabla\times\mathbf{E}+\epsilon\nabla\times\frac{\partial\mathbf{E}}{\partial t} \\
&= \sigma(-\frac{\partial\mathbf{B}}{\partial t})+\epsilon\frac{\partial}{\partial t}(\nabla\times\mathbf{E}) \\
&= \sigma(-\frac{\partial\mathbf{B}}{\partial t})+\epsilon\frac{\partial}{\partial t}(-\frac{\partial\mathbf{B}}{\partial t}) \\
&= -\sigma\mu\frac{\partial\mathbf{H}}{\partial t}-\epsilon\mu\frac{\partial^2\mathbf{H}}{\partial t^2}. \qquad (4)
\end{aligned}$$

Dividing Equation (1b) by μ, we obtain $\nabla\cdot(\mathbf{B}/\mu)=0$. Since $\mathbf{B}=\mu\mathbf{H}$, the Laplacian operator gives $\nabla\cdot\mathbf{H}=0$. Therefore, the left side of Equation (4) has an alternative form:

$$\nabla\times\nabla\times\mathbf{H}=\nabla(\nabla\cdot\mathbf{H})-\nabla^2\mathbf{H}=-\nabla^2\mathbf{H}. \qquad (5)$$

By comparing Equation (4) and (5), we obtain a differential equation for the magnetic field $\mathbf{H}$ that is dependent on time t:

$$\nabla^2\mathbf{H}=\sigma\mu\frac{\partial\mathbf{H}}{\partial t}+\epsilon\mu\frac{\partial^2\mathbf{H}}{\partial t^2}. \qquad (6)$$

Similarly, $\nabla\times\nabla\times\mathbf{E}$ can be expanded as

$$\begin{aligned}
\nabla\times\nabla\times\mathbf{E} &= \nabla\times(-\frac{\partial\mathbf{B}}{\partial t}) \\
&= \nabla\times(-\frac{\partial\mu\mathbf{H}}{\partial t}) \\
&= -\mu\frac{\partial}{\partial t}(\nabla\times\mathbf{H}) \\
&= -\mu\frac{\partial}{\partial t}(\mathbf{J}+\frac{\partial\mathbf{D}}{\partial t}) \\
&= -\mu\frac{\partial}{\partial t}(\sigma\mathbf{E}+\frac{\partial\epsilon\mathbf{E}}{\partial t}) \\
&= -\mu\sigma\frac{\partial\mathbf{E}}{\partial t}-\mu\epsilon\frac{\partial^2\mathbf{E}}{\partial t^2}. \qquad (7)
\end{aligned}$$

Also, $\nabla\cdot\mathbf{E}=\rho=0$, since there are no free carriers in the dielectric sphere under consideration. Thus, we have

$$\nabla \times \nabla \times \mathbf{E} = \nabla(\nabla \cdot \mathbf{E}) - \nabla^2 \mathbf{E} = -\nabla^2 \mathbf{E}. \tag{8}$$

By comparing Equations (7) and (8), we can write a single equation that gives the time dependence of the electric field:

$$\nabla^2 \mathbf{E} = \sigma\mu \frac{\partial \mathbf{E}}{\partial t} + \epsilon\mu \frac{\partial^2 \mathbf{E}}{\partial t^2}. \tag{9}$$

If we assume that the electric field has a simple harmonic form given by

$$\mathbf{E} = \mathbf{E}_0 e^{-i\omega t}, \tag{10}$$

the first and second time derivatives are $\partial \mathbf{E}/\partial t = -i\omega \mathbf{E}$, and $\partial^2 \mathbf{E}/\partial t^2 = -\omega^2 \mathbf{E}$. Substituting these derivatives into Equation (9), we obtain

$$\begin{aligned} \nabla^2 \mathbf{E} &= \sigma\mu(-i\omega \mathbf{E}) + \epsilon\mu(-\omega^2 \mathbf{E}) \\ &= -i\omega\sigma\mu \mathbf{E} - \omega^2 \epsilon\mu \mathbf{E} \\ &= -\omega^2 \epsilon\mu(\frac{\sigma}{\omega\epsilon} i + 1)\mathbf{E} \\ &= -k^2 n_i^2 \mathbf{E}, \end{aligned}$$

which can be rewritten as

$$\nabla^2 \mathbf{E} + k^2 n_i^2 \mathbf{E} = 0, \tag{11}$$

According to Equation (8), Equation (11) is equivalent to

$$\nabla \times \nabla \times \mathbf{E} - k^2 n_i^2 \mathbf{E} = 0, \tag{12}$$

according to Equation (8), where k and n_i are the vacuum wave number and the refractive index, respectively.

Equation (11) is known as the Helmholtz equation. It takes its name from the German physicist Hermann von Helmholtz (1821-1894). The Helmholtz equation describes the spatial and temporal behavior of the electromagnetic field, and can be used to find frequency or time-harmonic solutions for electromagnetic waves. For example, the Helmholtz equation can be used to find the resonant frequencies in a waveguide, and to explore how electromagnetic waves propagate in real time. Along with the appropriate boundary conditions, the Helmholtz equation can also be used to investigate reflection [28] and diffraction problems [29]. Also, the Helmholtz equation finds applications in seismology as well in which the seismic waves are transverse [30].

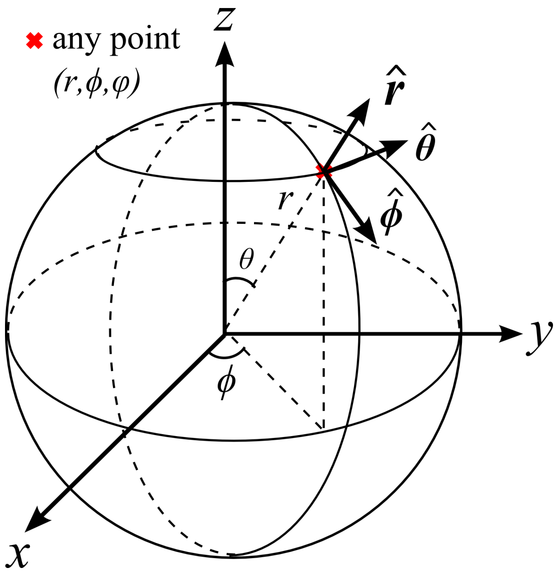

Figure 4. Any point can be specified in spherical coordinates by three numbers: r, θ and ϕ. The variable r is the distance from the origin to the point, θ is the angle projected onto the y-z plane relative to the z-axis (i.e., the latitude), and ϕ is the angle projected onto the x-y plane relative to the x-axis (i.e., the longitude).

Since we are dealing with resonances of a microsphere, it's easier to solve the Helmholtz equation in the spherical coordinate system. In spherical coordinates, by separating out the time dependence (see Equation (10)), Equation (12) can be written as [31]:

$$\frac{1}{r^2}\frac{\partial}{\partial r}(r^2\frac{\partial \mathbf{E}}{\partial r}) + \frac{1}{r^2 sin\theta}\frac{\partial}{\partial\theta}(sin\theta\frac{\partial \mathbf{E}}{\partial\theta}) + \frac{1}{r^2 sin^2\theta}\frac{\partial^2 \mathbf{E}}{\partial\phi^2} + (k_0 n_i)^2\mathbf{E} = 0, \tag{13}$$

where k_0 is the resonance wave number, r, θ, and ϕ denote the radial direction, the "polar" direction, and the azimuthal direction, respectively (Figure 4).

The method of separation of variables is typically applied to solve Equation (13). With this method, one assumes that the solution of Equation (13) can be written in the following product form:

$$\mathbf{E}(r,\theta,\phi) = R(r)\Theta(\theta)\Phi(\phi), \tag{14}$$

where $R(r)$, $\Theta(\theta)$ and $\Phi(\phi)$ are functions only dependent on r, θ and ϕ, respectively.

By substituting Equation (14) into (13), one obtains

$$\frac{sin^2\theta}{R}\frac{d}{dr}(r^2\frac{dR}{dr}) + \frac{sin\theta}{\Theta}\frac{d}{d\theta}(sin\theta\frac{d\Theta}{d\theta}) + (k_0 n_i)^2 r^2 sin^2\theta = -\frac{1}{\Phi}\frac{d^2\Phi}{d\phi^2}. \tag{15}$$

The angle ϕ appears only in the right side of Equation (15), while the left side contains r and θ. The three variables r, θ and ϕ are independent of each other. Since each side of Equation (15) is based on different independent variables, both sides must be constant in order to preserve the equality. If we write both sides as being equal to $-m^2$ (for reason of convenience, as further described below), we obtain

$$\frac{1}{\Phi}\frac{d^2\Phi}{d\phi^2} = -m^2. \tag{16}$$

Equation (16) has a well known solution given by

$$\Phi(\phi) = a_m cos(m\phi) + b_m sin(m\phi), \tag{17}$$

where a_m and b_m are proportionality constants. $\Phi(\phi)$ describes the electric field distribution in the azimuthal direction. Since for a spherical resonance the solutions for $\Phi(\phi)$ are the same for ϕ and $\phi + 2\pi$, i.e. $\Phi(\phi + 2\pi) = \Phi(\phi)$, we see that m must be an integer.

By substituting Equation (16) into Equation (15), one obtains

$$\frac{1}{R}\frac{d}{dr}(r^2\frac{dR}{dr}) + \frac{1}{\Theta sin\theta}\frac{d}{d\theta}(sin\theta\frac{d\Theta}{d\theta}) + (k_0 n_i)^2 r^2 - \frac{m^2}{sin^2\theta} = 0. \tag{18}$$

In Equation (18), the first and the third terms depend only on r and the other two terms depend only on θ, therefore, they can also be separated into two equations by equating both sides to another constant $l(l+1)$:

$$\frac{1}{R}\frac{d}{dr}(r^2\frac{dR}{dr}) + (k_0 n_i)^2 r^2 = l(l+1), \tag{19}$$

and

$$\frac{1}{\Theta sin\theta}\frac{d}{d\theta}(sin\theta\frac{d\Theta}{d\theta}) - \frac{m^2}{sin^2\theta} = -l(l+1), \tag{20}$$

These equations can be written in a slightly different form:

$$\frac{d}{dr}(r^2\frac{dR}{dr}) + [(k_0 n_i)^2 r^2 - l(l+1)]R = 0, \tag{21}$$

and

$$\frac{1}{sin\theta}\frac{d}{d\theta}(sin\theta\frac{d\Theta}{d\theta}) + [l(l+1) - \frac{m^2}{sin^2\theta}]\Theta = 0. \tag{22}$$

Equations (21) and (22) together represent the same WGM, and both must be simultaneously satisfied.

Equation (21) is known as the spherical Bessel equation, whose two linearly independent solutions are denoted as $j_l(n_i k_0 r)$ and $y_l(n_i k_0 r)$. These are l^{th}-order spherical Bessel function of the first and second kind, respectively. A general solution can be written as the linear combination of $j_l(n_ik_0r)$ and $y_l(n_ik_0r)$:

$$R(r) = c_lj_l(n_ik_0r) + d_ly_l(n_ik_0r), \tag{23}$$

where c_l and d_l are proportionality constants. $R(r)$ describes the electric field distribution in the radial direction. The spherical Bessel functions have the following properties:

$$\begin{aligned} j_l(n_ik_0r) &\rightarrow \text{finite}, \qquad \text{when}\, n_ik_0r \rightarrow 0, \\ y_l(n_ik_0r) &\rightarrow \infty, \qquad \text{when}\, n_ik_0r \rightarrow 0. \end{aligned} \tag{24}$$

Since the electric field is finite in the center of the microsphere, $y_l(n_ik_0r)$ should be excluded from the solution. Therefore, d_l is set to 0 inside the sphere.

In addition to the spherical Bessel functions, another solution is represented by the spherical Hankel functions of the first and second kind [31]. These are linear combinations of Bessel functions given by

$$h_l^{(1)}(n_ik_0r) = j_l(n_ik_0r) + iy_l(n_ik_0r), \tag{25}$$

and

$$h_l^{(2)}(n_ik_0r) = j_l(n_ik_0r) - iy_l(n_ik_0r), \tag{26}$$

respectively. When $n_ik_0r/l \gg 1$, which is true for typical microsphere dimensions (tens of micrometers) and wavelength range (hundreds of nanometers) being studied, an asymptotic expansion of the spherical Hankel functions yields

$$h_l^{(1)}(n_ik_0r) \approx \frac{1}{n_ik_0r}e^{i(n_ik_0r - l\pi/2 - \pi/2)}, \tag{27}$$

and

$$h_l^{(2)}(n_ik_0r) \approx \frac{1}{n_ik_0r}e^{-i(n_ik_0r - l\pi/2 - \pi/2)}. \tag{28}$$

Equation (27) is consistent with a spherical wave propagating in the positive r-direction (i.e., outward toward the microsphere), while Equation (28) represents the opposite direction (i.e., an inward traveling wave). The time dependences can be incorporated by multiplying Equations (27) and (28) by e^{-ickt}, if one wants to model the time evolution of the WGM.

As briefly described above, the function selected to model the electric field depends on a set of logical requirements for how the field must look in the different regions. Inside the microsphere, we simply require that the field not become infinite. This rules out the Bessel function of the second kind, which is infinite at the origin. Hence, the field inside the sphere is described by $j_l(n_i k_0 r)$. Any photon that escapes the microsphere can propagate to infinity (i.e., the "open boundary" situation); hence a Hankel function with the appropriate sign for an outward-radiating wave is required in that region.

After obtaining the radial field solutions from Equation (21), we can then proceed to look for the polar solutions. Equation (22) is known as Legendre's equation, whose two linearly independent solutions are $P_l^m(cos\theta)$ and $Q_l^m(cos\theta)$. These are called the associated Legendre functions of the first and second kind of degree l and order m, respectively. A general solution can be written as a linear combination of these two solutions,

$$\Theta(\theta) = e_{lm} P_l^m(cos\theta) + f_{lm} Q_l^m(cos\theta) \tag{29}$$

where e_{lm} and f_{lm} are proportionality constants. $\Theta(\theta)$ describes the electric field distribution in the "polar" direction. The associated Legendre functions have the following properties:

$$P_l^m(cos\theta)|_{\theta=0,\pi} \rightarrow \text{finite}, \qquad \text{when } l \text{ is an integer}, \tag{30}$$

and

$$Q_l^m(cos\theta)|_{\theta=0,\pi} \rightarrow \infty. \tag{31}$$

For non-integer l, the associated Legendre function of the first kind goes to infinity: i.e., $P_l^m(cos\theta)|_{\theta=\pi} \rightarrow \infty$ and $P_l^m(-cos\theta)|_{\theta=\pi} \rightarrow \infty$. Since the field is finite everywhere, l must therefore be an integer. Because the domain in the θ-direction is given by $0 \leq \theta \leq \pi$ and the solution is finite everywhere, f_{lm} is set to 0 to exclude $Q_l^m(cos\theta)$. The solution for $\Theta(\theta)$ is therefore

$$\Theta(\theta) = e_{lm} P_l^m(cos\theta). \tag{32}$$

Furthermore, for any value of l, the integer m can take values from $-l$ to l. The numbers l and m together describe the overall structure of the resonant electric field.

At this point we have examined all of the components of Equation (14), that completely describes the electric field of a spherical WGM. Equations (25) and (26) represent the radial part of the field, Equation (32) the "polar" part, and Equation (17) the azimuthal part. However, since the equatorial modes have the strongest electric field (i.e., see Figure 2), these modes will interact most strongly with the quantum dot fluorescent film and will dominate the microsphere WGM spectra to be described later. Thus, the remainder of this section will focus on the properties of the equatorial WGMs and we will therefore be concerned primarily with the radial profile of the electric field.

Here we will establish the basic functions for the radial component of the electric field. This leads naturally from the above discussion, where the requirements for the field inside and outside of the microsphere were briefly described. In the experiment the situation is slightly more complicated because we have three layers: the microsphere, a coating on the surface of the microsphere, and the surrounding environment. The refractive index distribution of a coated microsphere can be written as a piecewise function:

$$n(r) = \begin{cases} n_1, & r < b \\ n_2, & b \leq r \leq a \\ n_3, & r > a \end{cases} . \tag{33}$$

where b is the radius of the microsphere (index n_1) and a is the radius of the microsphere after it has been coated with a fluorescent layer of index n_2 (hence, the film thickness is simply $t = a - b$). The surroundings have refractive index n_3. A schematic cross sectional drawing of the structure is shown in Figure 5.

In a 3-layer structure, one can define a radial function $S_l(r)$ or $T_l(r)$ to model the electric field profile for TE and TM polarizations, respectively [31]. In the TE case, $S_l(r)$ is proportional to the electric field amplitude and can be written as:

$$S_l(r) = \begin{cases} A_l \psi_l(n_1 k_o r) & r < a - t \\ B_l \xi_l^{(2)}(n_2 k_0 r) + C_l \xi_l^{(1)}(n_2 k_0 r) & a - t \leq r \leq a \\ D_l \xi_l^{(1)}(n_3 k_0 r) & r > a \end{cases} , \tag{34}$$

where A_l, B_l, C_l and D_l are proportionality constants, $\psi_l = n_i k_0 r \cdot j_l(n_i k_0 r)$ is the l^{th}-Riccati-Bessel function, and $\xi_l^{(1)} = n_i k_0 r \cdot [j_l(n_i k_0 r) + i y_l(n_i k_0 r)]$ and $\xi_l^{(2)} = n_i k_0 r \cdot [j_l(n_i k_0 r) - i y_l(n_i k_0 r)]$ are the Riccati-Hankel functions of the first and second kind, respectively. Equation (34) represents the solution to Helmholtz equation in a coated

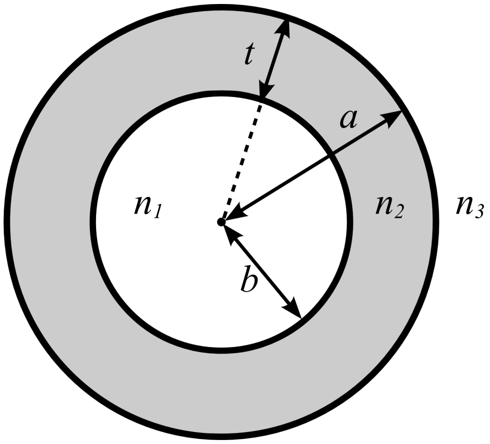

Figure 5. Distribution of the refractive index along the r-direction along an equatorial cross section of a microsphere of radius b. The sphere has index n_1, the grey shaded layer represents a coating of thickness t and index of n_2, and the surrounding index (e.g., air or water) is n_3.

microsphere with the following conditions in each layer: layer 1→microsphere with radius of b and refractive index of n_1, layer 2→coated layer with thickness of $t = a - b$ and refractive index of n_2, layer 3→outside medium with refractive index of n_3.

Here, we should make a note on the use of the Riccati-Bessel equations in Equation (34), as opposed to the spherical Bessel equations. Equation (21) can also be expressed in terms of Riccati-Bessel functions:

$$\frac{d^2}{dr^2}(n_i k_0 r R) + [(n_i k_0)^2 - \frac{l(l+1)}{r^2}](n_i k_0) r R = 0, \tag{35}$$

Equations (21) and (35) are identical. However, the Riccati-Bessel function, when squared and plotted as a function of r, is proportional to the energy density in the cavity. This is important because the refractometric sensitivity is proportional to the energy density in the different layers. Thus, in this section the radial functions are written in terms of the Riccati-Bessel functions, rather than the standard spherical Bessel equations.

The electric field must satisfy the appropriate boundary conditions [32]. The tangential component of the electric field must be continuous across the dielectric interfaces, and the same is true for the normal component of the electric displacement. A layered sphere has two interfaces: one is the glass-coating boundary and the second is the boundary between the coating and the outer medium. These are defined as interfaces b and a, respectively, where the layer thickness $t = a - b$. The boundary conditions will result in different solutions for the two polarizations.

For the TE polarization the boundary conditions must satisfy a modified log-derivative given by $[S'(r)/[k \cdot S(r)]$ [32]: this function must be continuous on each side of an interface. At interface b, the boundary conditions require that

$$A_l\psi_l(n_1k_0z) = B_l\xi_l^{(2)}(n_2k_0z) + C_l\xi_l^{(1)}(n_2k_0z), \tag{36}$$

and

$$A_ln_1\psi_l'(n_1k_0z) = B_ln_2\xi_l'^{(2)}(n_2k_0z) + C_ln_2\xi_l'^{(1)}(n_2k_0z). \tag{37}$$

At interface a, the boundary conditions for the TE polarization give

$$B_l\xi_l^{(2)}(n_2k_0a) + C_l\xi_l^{(1)}(n_2k_0a) = D_l\xi_l^{(1)}(n_3k_0a), \tag{38}$$

and

$$B_ln_2\xi_l'^{(2)}(n_2k_0a) + C_ln_2\xi_l'^{(1)}(n_2k_0a) = D_ln_3\xi_l'^{(1)}(n_3k_0a). \tag{39}$$

From the ratio of Equations (36) and (37), we can obtain B_l and C_l as

$$B_l = -n_1\psi_l'(n_1k_0z)\xi_l^{(1)}(n_2k_0z) + n_2\xi_l'^{(1)}(n_2k_0z)\psi_l(n_1k_0z), \tag{40}$$

and

$$C_l = -n_2\xi_l'^{(2)}(n_2k_0z)\psi_l(n_1k_0z) + n_1\psi_l'(n_1k_0z)\xi_l^{(2)}(n_2k_0z). \tag{41}$$

The remaining coefficients A_l and D_l can be calculated by substituting B_l and C_l into Equation (36) and (38), respectively:

$$A_l = \frac{B_l\xi_l^{(2)}(n_2k_0z) + C_l\xi_l^{(1)}(n_2k_0z)}{\psi_l(n_1k_0z)}, \tag{42}$$

and

$$D_l = \frac{B_l\xi_l^{(2)}(n_2k_0a) + C_l\xi_l^{(1)}(n_2k_0a)}{\xi_l^{(1)}(n_3k_0a)}. \tag{43}$$

To calculate the resonant frequency, Equation (38) is divided by Equation (39), which gives

$$\frac{n_2}{n_3}\frac{\xi_l^{(1)}(n_3k_0a)}{\xi_l'^{(1)}(n_3k_0a)} = \frac{\frac{B_l}{C_l}\xi_l^{(2)}(n_2k_0a) + \xi_l^{(1)}(n_2k_0a)}{\frac{B_l}{C_l}\xi_l'^{(2)}(n_2k_0a) + \xi_l'^{(1)}(n_2k_0a)}. \tag{44}$$

The resonance wave vectors, k_0, are the roots of Equation (44). These solutions can be obtained by numerical root-finding algorithms (such as Mathematica's FindRoot function). By substituting the root, k_0, into Equations (40)-(43), A_l, B_l, C_l and D_l can be obtained. At this point, the TE-polarized electric field in the radial direction can be fully described by simply plotting Equation (34).

For TM waves, the radial field function can be written as

$$T_l(r) = \begin{cases} a_l\psi_l(n_1k_or) & r < a-t \\ b_l\xi_l^{(2)}(n_2k_0r) + c_l\xi_l^{(1)}(n_2k_0r) & a-t \leq r \leq a \cdot \\ d_l\xi_l^{(1)}(n_3k_0r) & r > a \end{cases} \tag{45}$$

Here, the lower case a_l, b_l, c_l and d_l are proportionality constants for the TM polarization. The boundary conditions are given by a different log-derivative function $(T_l'(r)/[n_i^2k \cdot T_l(r)])$, that must be continuous on each side of an interface [32]. At interface b, this yields

$$a_l\psi_l(n_1k_0z) = b_l\xi_l^{(2)}(n_2k_0z) + c_l\xi_l^{(1)}(n_2k_0z), \tag{46}$$

and

$$a_l\frac{1}{n_1}\psi_l'(n_1k_0z) = b_l\frac{1}{n_2}\xi_l'^{(2)}(n_2k_0z) + c_l\frac{1}{n_2}\xi_l'^{(1)}(n_2k_0z) \tag{47}$$

At interface a, the boundary conditions require that

$$b_l\xi_l^{(2)}(n_2k_0a) + c_l\xi_l^{(1)}(n_2k_0a) = d_l\xi_l^{(1)}(n_3k_0a), \tag{48}$$

and

$$b_l\frac{1}{n_2}\xi_l'^{(2)}(n_2k_0a) + c_l\frac{1}{n_2}\xi_l'^{(1)}(n_2k_0a) = d_l\frac{1}{n_3}\xi_l'^{(1)}(n_3k_0a). \tag{49}$$

From the ratio of Equation (46) to (47), we can obtain b_l and c_l

$$b_l = -n_2\xi_l^{(1)}(n_2k_0z)\psi_l'(n_1k_0z) + n_1\psi_l(n_1k_0z)\xi_l'^{(1)}(n_1k_0z), \tag{50}$$

and

$$c_l = -n_1\psi_l(n_1k_0z)\xi_l'^{(2)}(n_2k_0z) + n_2\xi_l^{(2)}(n_2k_0z)\psi_l'(n_1k_0z). \tag{51}$$

As before, the remaining coefficients a_l and d_l can be calculated by substituting

b_l and c_l to Equation (46) and (48), respectively:

$$a_l = \frac{b_l \xi_l^{(2)}(n_2 k_0 z) + c_l \xi_l^{(1)}(n_2 k_0 z)}{\psi_l(n_1 k_0 z)}, \tag{52}$$

and

$$d_l = \frac{b_l \xi_l^{(2)}(n_2 k_0 a) + c_l \xi_l^{(1)}(n_2 k_0 a)}{\xi_l^{(1)}(n_3 k_0 a)}. \tag{53}$$

To calculate the resonant wave vector, k_0, Equation (48) is divided by Equation (49), which gives

$$\frac{n_3}{n_2} \frac{\xi_l^{(1)}(n_3 k_0 a)}{\xi_l'^{(1)}(n_3 k_0 a)} = \frac{\frac{b_l}{c_l} \xi_l^{(2)}(n_2 k_0 a) + \xi_l^{(1)}(n_2 k_0 a)}{\frac{b_l}{c_l} \xi_l'^{(2)}(n_2 k_0 a) + \xi_l'^{(1)}(n_2 k_0 a)}. \tag{54}$$

Equations (44) and (54) are slightly different, as a result of the different boundary conditions for TE and TM polarized waves. Again, the resonant wave vector k_0 and the coefficients a_l, b_l, c_l, d_l can be obtained from Equations (50–54). Thus the TM polarized magnetic field in the radial direction can be fully described by Equation (45).

To summarize, the electric field can be derived from Maxwell's equations for both TE and TM polarizations. The investigation of the mode properties (e.g., Q factors, loss mechanism which will be discussed in the next section) of the coated microspheres requires the field distribution information. The field distribution also enables one to calculate the refractometric sensitivity, as discussed in Chapter 1.4.

1.2 Properties of spherical microcavities

1.2.1 General properties: Q and V

The quality (Q) factor is one of the most important characteristics of an optical cavity. Fundamentally, the Q factor is the ratio of the energy stored in the cavity to the energy dissipated per oscillation of the field:

$$Q = 2\pi \times \frac{\text{Energy Stored}}{\text{Energy dissipated per cycle}}. \tag{55}$$

Large values of Q are thus associated with low-loss resonators. In the case of a microsphere, the highest experimental Q factor ever reported is $\sim 10^{10}$ [33]. The experimental limit is usually associated with scattering losses due to factors discussed further in Chapter 1.2.3.

The stored energy and the energy lost per cycle are difficult values to access experimentally. Cavity ringdown spectroscopy is one of the few examples where the energy decay out of a cavity is directly measured [34]. Thus, more practical but equivalent definitions of the Q factor are often used:

$$Q = \omega\tau, \tag{56}$$

where τ is the ringdown time and ω is the angular frequency. The Q factor can also be related to the resonance linewidth according to

$$Q = \frac{\omega_0}{\delta\omega} = \frac{f_0}{\delta f} = \frac{\lambda_0}{\delta\lambda}, \tag{57}$$

where ω_0, f_0, λ_0 are the resonant angular frequency, frequency, and wavelength, respectively, $\delta\omega$, δf, $\delta\lambda$ are the corresponding full-width-at-half-maximum. This definition can be obtained from Equation (55) via an analysis of resonant RLC circuits [35], and is the most common way to measure the Q factor experimentally.

Another important cavity characteristic is the effective mode volume V_{eff}. The mode volume is defined as the spatial integral of the optical energy density in the mode, normalized to its maximum value [13]:

$$V_{eff} = \frac{\int_V \varepsilon(\mathbf{r})|\mathbf{E}(\mathbf{r})|^2 d^3\mathbf{r}}{max[|\varepsilon(\mathbf{r})|\mathbf{E}(\mathbf{r})|^2]}, \tag{58}$$

where $\varepsilon(\mathbf{r})$ is the dielectric constant, and $|\mathbf{E}(\mathbf{r})|$ is the electric field amplitude. The integration volume V encompasses the resonator and its surroundings, so the integral in Equation (58) diverges as $r \to \infty$. Usually, some arbitrary integration limit (e.g., 100 times the sphere radius) is assumed [36]. Typical values of the mode volume for microsphere are a few hundred μm^3 [37] depending on the microsphere size, and they are smallest for the equatorial modes. The mode volume can be as small as a few cubic microns in micropillar [38] and photonic crystal cavities [39], which represents a particularly attractive feature of such structures.

The ratio Q/V_{eff} is an important overall property, because it effectively controls how strongly an emitter can be influenced by the microcavity. The larger this ratio, the more prominent the cavity effects will become. Microspheres have the advantage of high Q factors and ease of synthesis compared to other types of microcavities, but they also have a relatively large mode volume. Thus, “strong” cavity interactions (to be described briefly below) are often studied in photonic crystals or micropillars that feature moderate Q factors but small mode volumes [40]. Microsphere resonators can be especially useful in situations where the Q factor is the most important parameter, which can be the case for optical sensors [41].

There are two cavity-QD coupling regimes, known as "weak" and "strong" coupling [42]. Which regime the system is in depends on the "coupling parameter", g_0, the non-resonant decay rate of the quantum dot, γ, and the cavity decay rate, κ (i.e., the ringdown rate). The "coupling parameter" is a measure of the rate at which the photon is re-absorbed by the QD in the cavity. The cavity decay rate is given by $\kappa = \omega/Q$, so a high Q factor indicates a small loss rate. The non-resonant decay rate represents emission into non-cavity modes (e.g., free space, guided modes, etc.). When $g_0 > (\kappa, \gamma)$, where (κ, γ) indicates the larger of κ and γ, the cavity-QD interaction is in the "strong coupling" regime. This condition must be met for QD-cavity systems to be used for quantum information processing [43] which requires that the interaction of the photon and the QD is reversible.

In this work, the QDs will be in the weak coupling regime. The main physical effect is a modification of the radiative decay rate associated with the QDs. This phenomenon was named after physicist Edward Purcell [44], who was one of the first to report on cavity-rate-enhancement effect (Purcell's work was related to the nuclear magnetic moment transitions at radio frequencies). The Purcell factor, F_P, is the ratio of the emission rate in the cavity to that of the same emitter in free space. It is related to Q and V_{eff} according to [44]:

$$F_P = \frac{W_{cav}}{W_{free}} = \frac{\tau_{free}}{\tau_{cav}} = \frac{3Q(\lambda/n_i)^3}{4\pi^2 V_{eff}}, \tag{59}$$

where W is the spontaneous emission rate of the QD, τ is the QD radiative lifetime, n_i is the refractive index, and the subscripts indicate free space ("*free*") or cavity ("*cav*"). This formula applies specifically to the ideal case of a narrow-linewidth emitter that is exactly centered on a cavity resonance. If these conditions are not exactly satisfied, the effective Purcell factor will be smaller [45].

For quantum dots in a microcavity, the emission rate can be enhanced at the cavity resonant frequencies (i.e. $F_P > 1$), and the emission rate for QDs having off-resonant emission frequencies can be suppressed (i.e., $F_p < 1$) [46]. There are several examples in the literature in which the Purcell factor has been measured for the emission of a quantum dot in a microcavity. For example, the spontaneous emission rate was enhanced by a factor of 4.6 for a single InAs QD embedded in a micropost cavity [46]. A Purcell factor of 5 was reported for the same type of QD in another micropost cavity [47]. Other work reported a 32-fold increase of the spontaneous emission rate in a similar system [48], and others estimated theoretically that F_p could be as high as 190 for InAs QDs on microdisk cavities [49]. From Equation (59), for a microsphere with a radius of 25 µm and a Q factor of 10^9, F_P would be approximately 480 at a wavelength of 750 nm, assuming that the mode volume is equal to the microsphere volume (in reality V_{eff} would be significantly smaller). This suggests that large Purcell factors might be achievable for microspheres, but in reality F_p is usually found to be much smaller due to several deleterious effects (i.e., positioning of the QD away from the field antinode, polarization mismatch for the dipole and the cavity, and lower Q factors for QD-coated microspheres, and the finite linewidth of the emitter).

1.2.2 Ensemble properties

While Q and V are the most important cavity-related properties, the fluorescence WGM spectrum can be described by an additional set of parameters when an ensemble of emitters is coupled to a cavity. These properties are common in laser and grating physics: the free spectral range (FSR), the cavity Finesse ($\mathcal{F}$), and the WGM visibility (V_I). In a microsphere, the FSR is defined as the frequency difference between two modes with the same radial and polar numbers but differing by one azimuthal number, and can be estimated as [50, 51]:

$$\Delta f_{FSR} = f_{nm,\,l} - f_{nm,\,l-1} \approx \frac{c}{2\pi a}\frac{tan^{-1}\sqrt{n_i^2-1}}{\sqrt{n_i^2-1}}, \tag{60}$$

where Δf_{FSR} is the free spectral range, $f_{nm,\,l}$ is the resonant frequency for a mode with quantum numbers $(n,\, m,\, l)$, $f_{nm,\,l-1}$ is the frequency of a mode one angular unit smaller, c is the speed of light in vacuum, a is the radius of the cavity, and n_i is its refractive index. The FSR depends inversely on the size of the microsphere: the smaller the radius, the greater the frequency separation between modes. Experimentally, the FSR is a measure of how well-separated the WGMs are; a small FSR implies that the WGMs may significantly overlap and that they may be experimentally difficult to resolve.

The finesse of the cavity is defined as the ratio of the free spectral range to the full-width-at-half-maximum (FWHM) of a resonance and is given by

$$\mathcal{F} = \frac{\Delta f_{FSR}}{\Delta f_{FWHM}} = Q\frac{\Delta f_{FSR}}{f_0}. \tag{61}$$

In a small microcavity, the free spectral range can be similar to the cavity mode frequency. In this case, the finesse is similar in magnitude to the Q factor and is thus also a measure of the ability of the cavity to store energy. In a large cavity, $\Delta f_{FSR} << f_0$, so the Q factor is much larger than the finesse. The finesse also characterizes the resolving power or spectral resolution of the cavity [52].

Finally, the visibility of a whispering gallery mode is defined as

$$V_I = \frac{I_{max} - I_{min}}{I_{max} + I_{min}}, \tag{62}$$

where I_{max} and I_{min} are the maximum and minimum intensity in the mode structure, respectively. The visibility essentially quantifies the intensity contrast between the WGM resonances and the background. A good visibility helps to distinguish the WGMs from experimental noise.

1.2.3 Loss mechanisms

There are several effects that can limit the maximum achievable Q factor for any given microsphere. These include radiation losses due to the curved surfaces of the cavity (sometimes called “diffraction” losses), scattering due to surface roughness, and losses due to material absorption. Since these effects can all be important in the microcavities to be studied in this thesis, each of these loss mechanisms will be discussed briefly.

The observable cavity Q factor can be described as a “resistors in parallel” summation of the limiting Q factors due to each individual loss mechanism [53]:

$$Q^{-1}_{total} = Q^{-1}_{rad} + Q^{-1}_{sca} + Q^{-1}_{abs} + \cdots, \tag{63}$$

where Q_{total} is the total Q factor, Q_{rad} is the Q factor limited by radiation loss, Q_{sca} is the Q factor limited by the roughness-induced scattering loss, and Q_{abs} is the limiting value due to material absorption. Separating the individual contributions to the total cavity Q in this way is useful, since the dominant loss mechanism can be different for differently-sized microspheres, for microspheres with a quantum-dot-coating, or even for samples that have been stored in the lab for a long period of time.

Radiation loss

Radiation loss is due to the curvature of the microsphere surface. When a plane electromagnetic wave is incident on the curved interface between the microsphere and its surroundings, part of the energy is lost in the form of a radiating wave. In order to estimate the radiation-limited Q factor, one can find the complex root, k_0, of Equations (44) and (54). The Q factor is then obtained from k_0 via

$$Q_{rad} = \frac{Re[k_0]}{2Im[k_0]}, \tag{64}$$

where $Re[k_0]$ and $Im[k_0]$ are the real part and imaginary part of the wave number, respectively.

Surface Roughness

Surface roughness can cause light to be scattered out of the cavity. In previous work, the loss coefficient, α_{rough}, has been estimated using theories developed to model light scattering from optical waveguides [53, 54]. Accordingly, the loss coefficient due to surface roughness was estimated as

$$\alpha_{rough} = \varphi^2(r)({n_{cavity}}^2 - 1)\frac{k_{vac}^2}{8n_{cavity}}\sigma_{rms}^2\sqrt{\frac{\pi}{n_{eff^2-1}}}, \tag{65}$$

where $\varphi^2(r)$ is the field intensity at the resonator surface, normalized such that $\int_0^\infty = \varphi^2(r)dr = 1$, n_{eff} is the effective refractive index of the mode, n_{cavity} is the refractive index of the cavity material, $k_{vac} = 2\pi/\lambda_{vac}$ is the vacuum wave vector, and σ_{rms} is the root-mean-square roughness. As we showed in Chapter 1.1.2, the electric field intensity along the radial direction can be calculated. The effective index can be estimated as a weighted average calculated from the fraction of the field energy in each layer [55, 56]. Once all this has been done, the roughness limited Q factor can be estimated according to:

$$Q_{sca} = \frac{2\pi n_{eff}}{\lambda\alpha_{rough}} \tag{66}$$

Absorption-related loss

The material used to fabricate the microcavity may be absorbing, thereby limiting the total Q factor due to absorption-related loss. For example, the absorption coefficient, α_{abs}, of high-quality silica limits the ultimate achievable Q factor to approximately 10^{10} at a wavelength of 633 nm [33]. Ellipsometry is often used to measure the extinction coefficient, κ_{abs}, where $\alpha_{abs} = 4\pi\kappa_{abs}/\lambda$, and this value can be used to calculate the absorption-limited Q factor.

In order to estimate Q_{abs}, we can use the same mode-solving procedure as outlined above, except that the imaginary part of the material refractive index is not zero (i.e., the extinction coefficient $\kappa_{abs} > 0$). This lowers the total calculated Q factor from the radiation limited value to one limited by both absorption and radiation losses:

$$(\frac{1}{Q_{abs}} + \frac{1}{Q_{rad}})^{-1} = \frac{Re[k_0]}{2Im[k_0]}, \tag{67}$$

where $Re[k_0]$ and $Im[k_0]$ denotes the real part and the imaginary part of the complex resonant wave vector, as before. Since the radiation-limited Q factor can be calculated from Equation (64) (without the absorber), the absorption-related Q factor can be deduced from Equation (67).

The Q factors due to radiation loss, absorption, and roughness-induced scattering can be estimated as a function of microsphere radius (Figure 6). For these calculations, the absorption coefficient of silica was assumed to be 10^{-9} µm^{-1} [57]. We see that Q_{rad} increases exponentially as a function of the radius, and for radii larger than $\sim$ 6 µm, the radiation limited Q factor quickly becomes much larger than the maximum Q factors observed experimentally. Therefore, the radiation loss becomes negligible compared to other losses for large microspheres. The absorption-limited Q factor decreases only slightly on the sphere radius, mainly because the electric field becomes better confined within the absorbing silica. Q_{sca} is larger than Q_{rad} for spheres with radii smaller than $\sim$ 4 µm, assuming a root-mean-square roughness of 3.4 nm, as reported for the quantum-dot films used in the present work [53]. Thus, when the sphere radius exceeds $\sim$ 4 µm, scattering loss becomes more important and eventually becomes the Q-limiting loss mechanism. Given that the microspheres fabricated in this thesis will have radii in the range of 30 µm to 100 µm, surface roughness is thus expected to be the main limiting effect on the measured Q factors.

Inter-band absorption

One other loss mechanism could be important in the case of quantum-dot-coated microspheres like those synthesized in the present work. The QDs can themselves absorb cavity photons, exciting a carrier from the valence to the conduction band (i.e., inter-band absorption). The limiting Q factor due to this process can be estimated as well [58]. Accordingly, the loss coefficient, α_{ib}, is

$$\alpha_{ib} = \Gamma(\lambda) \int_{R_{QD,min}}^{R_{QD,max}} \sigma_{abs}(R_{QD}) \rho(R_{QD}) dR_{QD}(\lambda), \tag{68}$$

where $\Gamma(\lambda)$ is the confinement factor (the fraction of the mode energy stored within the QD-coating), $R_{QD}(\lambda)$ is the radius of a nanocrystal emitting with a bandgap corresponding to λ, $R_{QD,max}$ and $R_{QD,min}$ is the radius of the largest and smallest

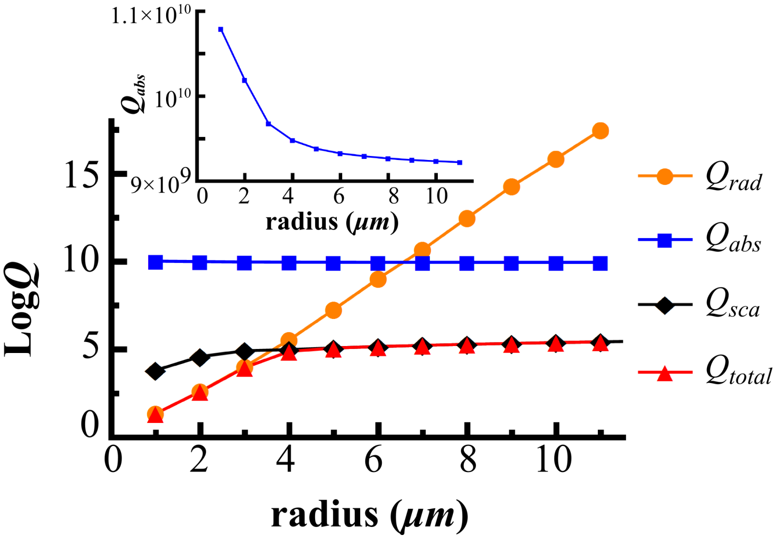

Figure 6. Limiting Q factors due to radiation loss, material loss (silica), and surface roughness for pure silica microspheres with radii varying from 1 μm to 11 μm. The WGM wavelength is around 750 nm in all cases. The outside medium is air. The inset shows Q_{abs} on a different vertical scale. The surface-roughness-induced scattering will be the most significant loss that limits the Q factor for large microspheres.

nanocrystal in the sample, respectively, $\sigma_{abs}(R)$ is the absorption cross section as a function of the nanocrystal radius, and $\rho(R_{QD})$ is the nanocrystal size distribution function. The integral term is simply meant to sum the effect of inter-band absorption across a known size distribution, when there is a variation of σ_{abs} with the particle radius. Q factors limited by inter-band absorption of the Si QDs are give by

$$Q_{ib} = \frac{2\pi n_{eff}}{\lambda \alpha_{ib}}. \tag{69}$$

A simple "back-of-the-envelope" estimate will be applied here to calculate the Q factor limited by the inter-band absorption of the Si QDs. One can use a QD radius and number density of 1.5 nm and 2.4×10^{18} cm^{-3}, respectively, as appropriate for QDs synthesized by the same methods as in this thesis [53]. The absorption cross section used in this work has not been studied yet, however, for an easy approximation, one could use 3.8×10^{-18} cm^2 measured for Si-rich silicon oxide layers from Ref. [59]. The confinement factor is calculated using equations developed in Chapter 1.1.2, for microspheres radius of 1 μm to 11 μm and a QD film thickness of 0.05 μm, at resonant wavelength of $\sim$ 750 nm which is around the peak wavelength of the fluorescence spectrum. Using those values, Q_{ib} associated with the Si-QD coating is plotted in Figure 7. This is on the same order of magnitude as Q_{sca} when the microsphere

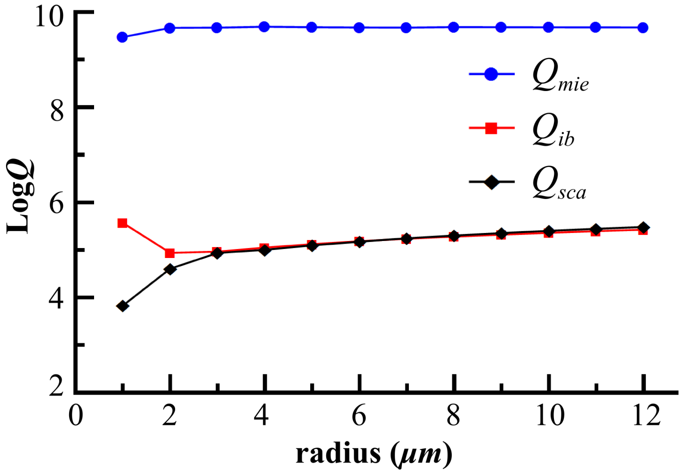

Figure 7. Limiting Q factors due to inter-band absorption and Mie scattering for the Si-QD-film, for microspheres with radii varying from 1 µm to 12 µm. The WGM wavelength is around 750 nm in all cases. The outside medium is air, and the thickness of the QD film is 50 nm.

radius $\sim$ 4 µm, suggesting that interband absorption in the QD films can represent significant loss mechanism. This conclusion is slightly different from the results of Ref. [58] for the case of a microdisk. The microdisk was fabricated lithographically and was much rougher than our QD films (rms roughness $\sim$ 17 nm vs $\sim$ 3 nm). Thus, surface roughness effects dominated over inter-band absorption for a microdisk; where here the effects are comparable.

Mie scattering

Finally, Mie theory can be used to describe the scattering of electromagnetic field by the (spherical) QDs that coat a microsphere. The loss coefficient due to Mie scattering can be estimated according to Ref. [53]

$$\alpha_{mie}(R_{QD},\lambda) = \Gamma(\lambda)\int_{R_{QD,min}}^{R_{QD,max}} \sigma_{mie}(R_{QD},\lambda)\rho(R_{QD})dR_{QD}(\lambda), \tag{70}$$

where the variables have the same meaning as in Equation (68). The integral again sums the scattering effect over the QD size distribution. The $\sigma_{mie}(R_{QD},\lambda)$ term represents the scattering cross-section associated with the QDs and is given by the Rayleigh formula [60]

$$\sigma_{mie}(R,\lambda) = \frac{8\pi}{3}(\frac{2\pi n_{cavity}}{\lambda})^4 R^6 (\frac{n_{QD}^2 - n_{cavity}^2}{n_{QD}^2 + 2n_{cavity}^2})^2, \tag{71}$$

where n_{cavity} and n_{QD} are the refractive index of the microcavity and QDs, respectively.

Again, for a simple estimation, the "back-of-the-envelope" calculation is applied. For the Si-QDs relevant to this thesis, one can take $R = 1.5$ nm and $\rho = 2.4\times10^{18}$ cm^{-3} [53], $n_{cavity} = 1.452$, n_{QD}=1.67 [61], and $\lambda = 750$ nm, leading to $\sigma_{Mie} \sim 1.98 \times 10^{-22}$ cm^2. The Q factor due to the Mie scattering is estimated as usual:

$$Q_{mie} = \frac{2\pi n_{eff}}{\lambda\alpha_{mie}}. \tag{72}$$

The estimated Mie-scattering-limited Q factor is calculated and plotted in Figure 7. Q_{mie} is almost 4 orders of magnitude higher than Q_{sca}; thus Mie scattering is insignificant compared to the other loss mechanisms.

Loss mechanism summary

Scattering due to surface roughness and the inter-band absorption appear to be the main Q-limiting loss mechanisms for microspheres with radii larger than $\sim$ 4 µm. Q_{rad}, Q_{abs} and Q_{mie} are all a few orders of magnitude larger than Q_{sca} and Q_{ib} for microspheres larger than this. Since Q_{sca} and Q_{ib} are comparable for the samples used in our work (generally on the order of 50 μm in diameter), there would probably not be much benefit to attempting to produce smoother films, because of the inter-band absorption losses. Interestingly, as discussed further in Chapter 2.3, the ultimate observable Q factors in our microspheres are typically in the range of a few times of $\sim 10^5$, which is reasonably close to the calculated Q_{total} shown in Figure 6.

1.2.4 Applications of optical microspheres

Microspheres have several potential applications that are currently being explored. "Tagged" or labeled fluorescent microspheres are already available commercially and are used in the biomedical field (e.g., for in vivo imaging) [62]. Here we will review more specifically the potential applications associated with microcavity effects.

- Low-threshold microlasers. As discussed in Chapter 1.2.1, microspheres have high Q factors and a reasonably high Q/V_{eff} ratio, which could make them attractive for low-threshold microlaser applications. The threshold of a laser is the power needed to balance optical gain and the loss in the laser cavity. In a microsphere, a high Q factor implies a low-loss cavity. Furthermore, the moderate mode volume implies that the total energy needed to achieve inversion is quite small. Microspheres with emitters, such as Er [63], Er:Yb [64], Er:Yt

[65], Nd [66], HgTe QDs [15], have thus been investigated as possible microlasers, with lasing thresholds as low as a few hundred nW [66].

- Thermo-optic switch. In a thermo-optic switch, one has two light sources: a "signal" beam that is to be switched, and a pump beam to control the switch. A microsphere can be coated with an absorbing layer (e.g., QDs [67] or a polymer [68] film), and both beams are evanescently coupled to the sphere through a taper or waveguide. When the pump beam is turned off, the signal beam is scanned on resonance with a WGM and a low intensity is detected at the output of the tapered fiber or waveguide. When the pump is switched on, the temperature of the microsphere increases, the refractive index changes via the thermo-optic effect, and the cavity WGM shifts away from the signal wavelength. Therefore, the signal beam does not couple efficiently into the microsphere and the output increases. Since microspheres have high Q factors (i.e., a sharp linewidth), the switching power required can be as low as 3.4 µW[67].

- Absorption microspectrometer. The intensity of light in a WGM is affected by losses arising from the absorbance in the analyte surrounding the microsphere. A clever way to utilize this property by constructing a microsphere-based microfluidic-absorption spectrometer was devised in Ref. [69]. The basic idea is that incident "white light" radiation is directed evanescently into a microsphere through a prism. The microsphere is eccentric rather than perfectly spherical, leading to the formation of nondegenerate, higher-order polar WGMs (i.e., $l \neq |m|$) which are not in the equatorial plane. Some of the incident light is coupled into these modes and is emitted at an angle away from the equatorial plane. Light in these "elliptical modes" can be collected by a detector located near the sphere. Since the evanescent light source consists of white light, many closely-spaced WGMs are excited simultaneously. Although the FSR was too small to observe individual resonances, by admitting a fluid analyte in a channel around the microsphere the absorption spectrum could be measured by comparing the spectrum obtained with and without the analyte.

- Refractive index sensors. Another potential application of the microsphere relates to the field of microfluidic-type sensors. This application will be directly relevant to the work done in this thesis. Essentially, the electric field of WGMs extends slightly outside the sphere and "samples" the surrounding medium. A change in the local refractive index will result in a WGM wavelength shift.

This shift represents the transduction mechanism. In this application, one is measuring changes in the local refractive index of the analyte fluid.

- Biosensors. Silica microspheres are amenable to a myriad of surface functionalization chemistries [70, 71, 72, 73]. Silane-based functionalization schemes are probably the most common but other types are widespread as well [74]. When bio-molecules attach specifically to the surface of the microsphere, they can be detected via a shift of the WGM resonance wavelength [75, 76]. The basic transduction method is the same as in the above case; the main difference is that the WGM shift should now be specific to a target analyte. Several examples have been shown in the literature; for example for protein detection [23], single virions [77], and E. coli bacteria [78].

1.2.5 Getting light in and out of a microsphere

All of the previous applications have a “simple” requirement: light must go into a microsphere and at some point it must be emitted into the surroundings. Thus, the means of getting light to couple into (and out of) the modes of a microsphere is a critical part of the experiment. There are two common methods to couple light into a microsphere: the first uses evanescent coupling through a tapered fiber or waveguide, and the second requires the excitation of a fluorophore placed on the microsphere surface. Both methods will be used in this work; therefore these two methods will be discussed briefly in this section.

Evanescent coupling

Evanescent coupling is based on the overlapping of the evanescent fields of the microsphere WGMs and a nearby fiber taper. Essentially, light is injected into a fiber, and the fiber (which must be tapered for reasons to be discussed shortly) is brought close to the microsphere so that light can be coupled into the sphere via the evanescent fields of the two structures. Thus, the length scale of the evanescent field is an important parameter that governs how close together the fiber (or waveguide) and the microsphere have to be in order to have efficient coupling of light between the two structures.

The length scale of the evanescent field can be readily estimated for a flat surface, as is commonly done in many optics textbooks [79]. A very brief review will be provided here, because the characteristic length is an important experimental parameter in this work. In Figure 8, ray-a and ray-b pass from medium 1 with refractive index n_1

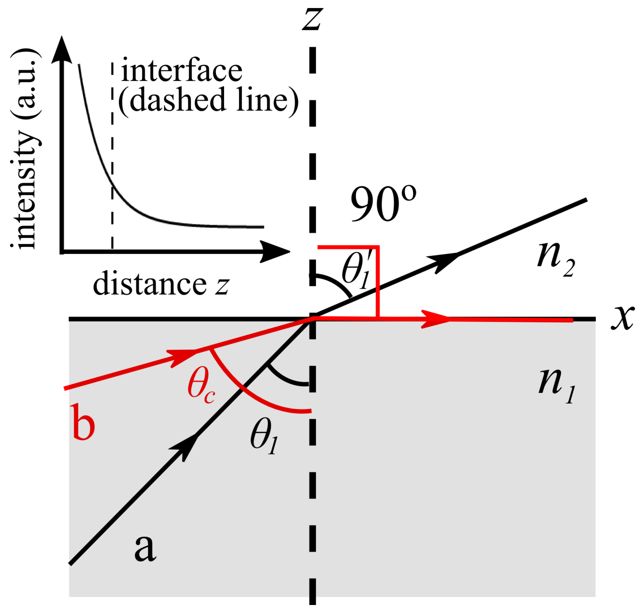

Figure 8. Total internal reflection at the interface $z = 0$ between two media with refractive indices n_1 (shaded area) and n_2 ($n_1 > n_2$). TIR occurs at critical angle θ_c. The inset shows how the intensity decreases in the low-index medium when the incident angle is equal to or larger than θ_c.

to medium 2 with index n_2, with $n_1 > n_2$. Total internal reflection (TIR) occurs when the incident angle, θ_1, is equal or larger than the critical angle, $\theta_c = sin^{-1}(n_2/n_1)$.

To study the amplitude of electric field in medium 2, the transmitted wave can be represented as [79]

$$E_t = E_{0t}e^{i(\mathbf{k}_t \cdot \mathbf{r} - \omega t)}, \tag{73}$$

where E_{0t} is the amplitude of the electric field, ω is the angular frequency, and $\mathbf{k}_t \cdot \mathbf{r}$ is expressed as

$$\mathbf{k}_t \cdot \mathbf{r} = k_t(-xsin\theta_t - zcos\theta_t), \tag{74}$$

where θ_t is the transmitted angle and the incident angle is θ_i. $\mathbf{k}_t \cdot \mathbf{r}$ in Equation (74) can be rewritten as a function of θ_i, since θ_t is dependent on θ_i,

$$cos\theta_t \equiv \sqrt{1 - sin^2\theta_t} = \sqrt{1 - (\frac{n_1}{n_2})^2 sin^2\theta_i}. \tag{75}$$

At the critical angle θ_c, $cos\theta_t = 0$. When $\theta_i > \theta_c$ (i.e., total internal reflection), Equation (75) becomes complex and $cos\theta_t$ can be written as

$$cos\theta_t = i\sqrt{(\frac{n_1}{n_2})^2 sin^2\theta_i - 1}. \tag{76}$$

Therefore, the exponential factor in Equation (73) is given by

$$\mathbf{k}_t \cdot \mathbf{r} = \quad -k_t x \frac{n_1}{n_2} sin\theta_i - ik_t z\sqrt{(\frac{n_1}{n_2})^2 sin^2\theta_i - 1}. \tag{77}$$

Finally, by substituting Equation (77) into Equation (73), we obtain:

$$E_t = E_{0t} e^{-i\omega t} e^{ik_t x(n_1/n_2) sin\theta_i} e^{-\alpha|z|}, \tag{78}$$

where $\alpha \equiv k_t\sqrt{(n_1/n_2)^2 sin^2\theta_i - 1}$. This leads directly to the characteristic evanescent field length:

$$d = \frac{1}{\alpha} = \frac{\lambda}{2\pi\sqrt{(\frac{n_1}{n_2})^2 sin^2\theta_i - 1}}. \tag{79}$$

Equation (79) can provide a simple estimation of how far the evanescent field extends from a silica glass interface into the surrounding medium. For the glass-air interface, the critical angle is $\theta_c = 44°$ and the penetration depth is $d = 114$ nm when the incident angle is 90°. From an experimental perspective this is a short distance and it means that the fiber and the microsphere have to be close together, requiring the use of nanometric positioning equipment, in order for efficient coupling to occur.

The calculation of the penetration depth in Equation (79) is based on a flat interface. However, a microsphere has a curved interface in which the field outside the sphere follows a Hankel function (see Equation (34)). Thus, the field outside the microsphere is not technically “evanescent” (i.e., lossless) but the term is widely used in the literature anyway, because at large nk_0r the field is nearly exponential (see Equation (27)). One might use the point at which the field has decayed to $1/e$ of its amplitude at the interface to describe the evanescent field “length”, as for the case of a flat surface. However, this is somewhat complicated by the fact that by the time that the field has reached the $1/e$ distance (compared to its amplitude at the interface), it is not yet behaving exponentially (i.e., the distance is still too short for the asymptotic approximation to be accurate).

In practice, however, the coupling efficiency between a microsphere and a taper (e.g., measured as power transferred per round trip) requires a calculation of the overlap integral for the two fields (sphere and taper). Ref. [80] showed how to do

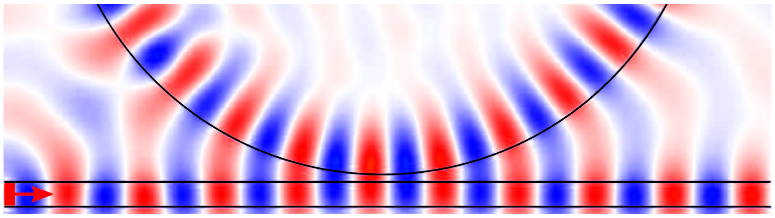

Figure 9. Finite difference time domain (FDTD) simulation showing 731.8 nm-light propagating along a taper (from left to right) and coupling into a WGM of a microsphere. The WGM and the taper modes are phase matched: that is, the position of the amplitude maxima and minima are coincident in both structures.

this, and found that the coupling could be reasonably effective even up to distance of ~ 1 µm.

The need for efficient coupling between the sphere and the fiber establishes some requirements on the optical fiber from which light is to be coupled into and out of the microsphere. First, the fiber must have a narrow waist, which generally requires tapering. A narrow waist can ensure that the taper supports only a few fiber modes, or even a single one. A single-mode fiber is desirable for coupling light into a microsphere, because it avoids having losses from the sphere into higher-order fiber modes. Second, the taper should be nearly adiabatic, so that there is no energy transfer into surroundings as the fiber waist narrows. Third, the taper and the microsphere should ideally be "phase matched". This means that the propagation constant of the taper must match that in the microsphere, in order to ensure constructive interference between light propagating within the two structures (Figure 9). While an adiabatic taper can be made fairly easily [81], a single mode fiber at wavelengths around $800nm$ is fragile and difficult to prepare. The phase matching condition can also be difficult to meet exactly.

There are three regimes that are often defined for light coupling between a taper and a microsphere. These regimes depend on the round-trip resonator loss and the amount of power coupled to the microsphere from the taper. The round-trip cavity loss, γ (i.e., caused by the loss mechanisms discussed in Chapter 1.2.3) is approximately equal to the product $2\pi a\alpha$ [82], where $2\pi a$ is the microsphere circumference and α is the absorption coefficient. The power coupling ratio, κ, is the ratio of power coupled into the sphere to the total power in the taper. The transmittance of the taper, T, at resonance ω_0 is given by [82]

$$T(\omega_0) = (\frac{1-\kappa/\gamma}{1+\kappa/\gamma})^2. \tag{80}$$

When $\kappa < \gamma$, the taper-microsphere system is in the "under-coupled" regime. In this case, the transmission through the taper at the resonant frequency cannot reach zero (in other words, the "dip" in the transmission spectrum is small). However, the Q factor of the microsphere is preserved because light loss back into the taper is minimal. When $\kappa > \gamma$, the system is overcoupled and the transmission once again does not go to zero on the resonance, since the optical power in the sphere couples very effectively back into the taper. However, the Q factor can be significantly lowered due to excessive loss from the sphere into the taper. Finally, if $\kappa = \gamma$, the transmittance goes to zero on resonance and the system is "critically coupled". This ensures a good signal strength (i.e., the transmission dip is large) while at the same time maintaining a good Q factor. When moving the sphere closer to the taper, the coupling regime will transfer from being under-coupled to critically-coupled and then to over-coupled.

Fluorescence coupling

First, let us discuss some definitions. Luminescence is light induced at normal or lower temperatures, i.e., the light is not induced from heat energy. Photoluminescence is generally the light emission after excitation by another shorter-wavelength light source. If this re-emission-light process happens fast (on the order of $10^{-7}\,s$), it is called fluorescence. In contrast, it is called phosphorescence if the process time lasts longer (e.g., seconds or even hours). The life time of Si QDs is ~µs [83]. Therefore, the term photoluminescence and fluorescence can both be used associated with the work in this thesis.

Exciting the WGMs via fluorescence presents a different experimental situation, with its own advantages and disadvantages. In this method, a fluorophore (i.e., quantum dots, as in this thesis) has to be placed as near as possible to the electric field maximum of the WGM. Since the field maximum is near the surface of the microsphere, this type of cavity is reasonably easy to fabricate by simply placing the fluorescent species directly onto the surface of the sphere. When the fluorophore is excited with a short-wavelength laser or LED, a fraction of the spontaneous emission couples into the WGMs, as discussed in Chapter 1.2.1. The WGMs then appear as intensity maxima in the resulting fluorescence spectrum.

Fluorescence measurements have a few key advantages. First, and probably most important, there is no need for the fabrication of a delicate fiber taper or waveguide, and there is no requirement for specialized positioning equipment. These are probably the most "finicky" aspects of the evanescent coupling method, and sidestepping them presents a significant experimental simplification. Second, there is also no need for a narrow-band tunable light source, which as yet presents a considerable experimental cost. Third, many WGMs can be collected simultaneously, whereas the evanescent method involves scanning over the modes in series.

However, there are a few drawbacks of the fluorescence method as well. First, the emitted light must enter a spectroscopy system, which implies a significant loss of intensity. Indeed, while the microWatt (or even milliWatt) range is easily possible in the evanescent technique described above, nanoWatt (or even picoWatt) intensities will be more common in a fluorescence system. Second, placing an emitter onto the microsphere surface can lower the Q factor due to roughness-induced scattering or absorption, as discussed in Chapter 1.2.3.

In this thesis, the fluorophore will be silicon quantum dots deposited onto the microsphere surface. The use of quantum dots, as opposed to conventional organic dyes, presents some advantages in terms of the stability (and utility) of the fluorescent cavity structure. The technique developed in this work has several useful features, as will be shown further in the main body of the thesis. In order to better understand the fluorophore, a brief review of the energy levels of of quantum dots generally, and then silicon more specifically, can be of value. This will give some basic information on the luminescence spectrum associated with the materials used here. For a full description of quantum dot physics, the reader is referred to References [42], [84], and [85]; here some of the key points will be reviewed in order to provide a basic understanding of the emitter used in this work.

1.3 Quantum dots

1.3.1 Particle in a spherical box

Quantum dots are nanometer-scale semiconductor crystallites that are, in many cases, excellent fluorophores compared to conventional organic dyes. The optical properties of QDs, such as the absorption and emission spectra, can be tuned by controlling their size. QDs are also chemically stable and inert, while organic dyes often show the effects of photobleaching [86]. They have a large transition dipole moment compared to atomic or molecular species [87], which are important for cavity-QD interactions. Furthermore, QDs can be fabricated by a variety of different methods, which can be important in fine-tuning their chemical and physical properties [88, 89, 90]. Direct-gap QDs have been commercially available in various sizes and compositions for many years. In this work, the fluorescence spectrum of optical microspheres will be inves-

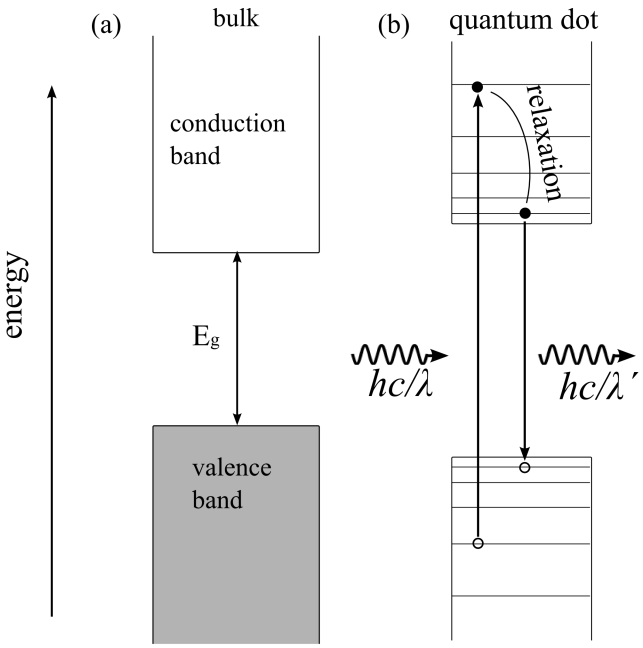

Figure 10. Schematic energy band diagram of bulk semiconductor materials (a) and quantum dots (b). The continuous energy bands become quantized in the case of QDs, increasing the electron-hole recombination energy.

tigated, using a layer of Si QDs as the fluorophore.

In order to understand the size-tuneability associated with the optical properties of QDs, one can briefly review the energy level structure of a "generic" bulk semiconductor with that of the corresponding quantum dot. In the bulk, the momentum-energy states in the valence and conduction bands are continuous. There is, of course, a forbidden energy gap between these bands, which is a fundamental property of all semiconductors. The band gap, E_g, depends on the crystal symmetry and composition, and is in the range of $0.5 - 3$ eV for most conventional semiconductors. However, when the material dimension decreases to the nanometer scale, the energy levels in the conduction and valence bands become quantized (see Figure 10). This so-called *quantum confinement* effect determines the energies at which the QD can absorb and emit radiation. Because of its importance, we will give a brief overview of quantum confinement and then provide a specific look at silicon, before closing this introduction with an overview of refractometric sensing mechanisms for QD-coated silica microspheres.

To calculate the energy quantization effect in a quantum dot, one typically starts from a simple "particle in a spherical box" model. In this model, a quantum dot is considered as a three dimensional spherically symmetric potential well $U(r)$ with an infinite barrier. The potential energy is thus, in the simplest sense, a straightforward piecewise function [85]:

$$U(r) = \begin{cases} 0, & \text{for}\, r \leq a \\ \infty, & \text{for}\, r > a \end{cases}, \tag{81}$$

where a is the radius of the quantum dot and r is the radial coordinate. In this approximation, charge carriers will be confined within the spherical potential barrier and cannot appear outside the barrier. The wave equation for electron (or hole) motion is given by the Schrödinger equation

$$H\psi = E\psi, \tag{82}$$

where E is the electron energy, ψ is the electron (or hole) wave function, and the Hamiltonian in the spherical coordinates is [85]

$$H = -\frac{\hbar^2}{2m_e r^2}\{\frac{\partial}{\partial r}(r^2\frac{\partial}{\partial r}) + \frac{1}{sin\theta}[\frac{\partial}{\partial\theta}(sin\theta\frac{\partial}{\partial\theta}) + \frac{1}{sin\theta}\frac{\partial^2}{\partial\phi^2}]\} + U(r). \tag{83}$$

where r, θ, ϕ are as indicated in Figure 4 and m_e is the electron effective mass (m_h is the hole effective mass). The solutions can be expressed as [91]

$$\psi_{n,l,m}(r,\theta,\phi) = R_{nl}(r)Y_{lm}(\theta,\phi), \tag{84}$$

where Y_{lm} is the spherical harmonic function, and $R_{nl}(r)$ satisfies the equation

$$\frac{d^2R_{nl}}{dr^2} + \frac{2}{r}\frac{dR_{nl}}{dr} + [k^2 - \frac{l(l+1)}{r^2}]R_{nl} = 0. \tag{85}$$

By setting $z = kr$, Equation (85) can be written as

$$\frac{d^2R_{nl}}{dz^2} + \frac{2}{z}\frac{dR_{nl}}{dz} + [1 - \frac{l(l+1)}{z^2}]R_{nl} = 0. \tag{86}$$

Due to the spherical symmetry of the problem (similar to the case for the WGMs described earlier), the solutions are again given by the spherical Bessel functions of the first and second kinds, denoted $j_l(kr)$ and $y_l(kr)$. The Bessel functions of the second kind are excluded because they are infinite at the origin, which would be unphysical. The three quantum numbers in Equation (84) are the radial number n, the azimuthal number l, and the "polar" number m. Again, we observe the similarity between this result and the one for the spherical WGMs in Chapter 1.1.2. The azimuthal number gives the angular momentum value **L**:

$$\mathbf{L}^2 = \hbar^2 l(l+1),\ l = 0,\ 1,\ 2,\ 3, \ldots, \tag{87}$$

and the polar number gives the **L** component parallel to the z axis:

$$L_z = \hbar m,\ m = 0,\ \pm 1, \pm 2, \ldots, \pm l. \tag{88}$$

For each integer l, the number m can take on integer values between $\pm l$. Therefore, each state is $2l+1$ degenerate. Energy levels with $l = 0,\ 1,\ 2,\ 3, \ldots$ are denoted as *s*-, *p*-, *d*-, and *f*- states, and so forth in alphabetical order. The spin quantum number s can take values of $1/2$ and $-1/2$, to indicate the spin up and down states, as usual. The total angular momentum associated with a confined electron or hole is then given by

$$J = \hbar\sqrt{j(j+1)}, \tag{89}$$

where $j = |l - s|,\ |l - s| + 1, \cdots |l + s|$. Thus, one can describe the confined electron states completely with four quantum numbers: the radial number n, the azimuthal number l, the polar number m and the spin number s.

The energy of the electron (or hole) states can be derived from the boundary condition requiring that $R_{n,l}(kr) = 0$ at $r \geq a$. This means that the wave number associated with the charge carriers must satisfy $ka = \chi_{n,l}$, where χ_{nl} are roots (i.e., the zeros) of the spherical Bessel functions with n being the number of the root and l being the order of the function. The allowed energy values for a confined electron can then be calculated from the formula:

$$E^e_{nl} = \frac{\hbar^2 k^2}{2m_e} = \frac{\hbar^2 \chi^2_{nl}}{2m_e a^2}. \tag{90}$$

The confinement energy is inversely proportional to the square of the QD radius. The same formula applies to confined holes, with m_e replaced by m_h (the hole effective mass). The energy states are classified by the radial and azimuthal number with $2l+1$ degeneracy. When the angular momentum is zero (i.e., $l = 0$), Equation (90) reduces to

$$E_n = \frac{\hbar^2(\pi n)^2}{2m_e a^2}. \tag{91}$$

The lowest energy levels are $E_{1e} = \hbar^2\pi^2/2m_e a^2$ and $E_{1h} = \hbar^2\pi^2/2m_h a^2$ for the electron and the hole, respectively.

The total electron-hole energy difference is given by

$$E_{eh}(a) = E_g + E^e_{nl}(a) + E^h_{nl}(a), \tag{92}$$

which, ideally, corresponds to the photon energy that can be absorbed by the quantum dot. E_g is the band gap of the bulk material. Although QDs may absorb to higher-energy states, they can relax thermally (see Figure 10) to the lowest excited states (i.e., E_{1e} and E_{1h}) prior to emitting (this is especially true for the valence band (hole) states, since they tend to be close together in energy).

1.3.2 Silicon QDs

The model described above allows one to obtain a simple picture of the quantum confinement effect. However, it is a rather gross simplification, especially as concerns silicon QDs. Several additional effects can modify the overall absorption and emission spectra, including but not limited to: i) the finite potential barriers; ii) electron-hole Coulomb and spin interactions; iii) phonon effects including quantization (silicon has an indirect gap thus requiring phonons for momentum conservation); and, iv) the spread of momentum states due to the uncertainty principle, which can lead to direct-gap behavior [92]. While it is beyond the scope of this thesis to consider all of these effects, several authors have reported alternative formulas (essentially modified versions of Equation (92)) that more accurately model the size dependence of the absorption or emission spectra [93, 94, 95, 96, 97, 98, 99, 100, 101].

One example is given in Ref. [94], in which the lowest electron-hole energy difference is given by

$$E_{PL}(a) = \sqrt{E_g^2 + \frac{D_1}{a^2}}, \tag{93}$$

where E_{PL} is the lowest electron-hole energy difference (i.e., the energy difference between E_{1e} and E_{1h}), a is the QD radius, E_g is the band gap of the bulk silicon, and $D_1 = 4.8\ \mathrm{eV}^2\cdot\ \mathrm{nm}^2$. In this equation, the lowest-energy transition is smaller than that calculated by Equation (92). The derivation of Equation (93) included the effects of the finite potential barriers and the discontinuity of the effective mass of the electron inside and outside the QD.

A similar size dependence was also reported in Ref. [96]:

$$E_{PL}(d) = E_0 + \frac{3.73}{d^{1.39}} - 3.572 \cdot \frac{e^2}{\varepsilon d}, \tag{94}$$

where d is the QD diameter. The derivation of Equation (94) included Coulomb

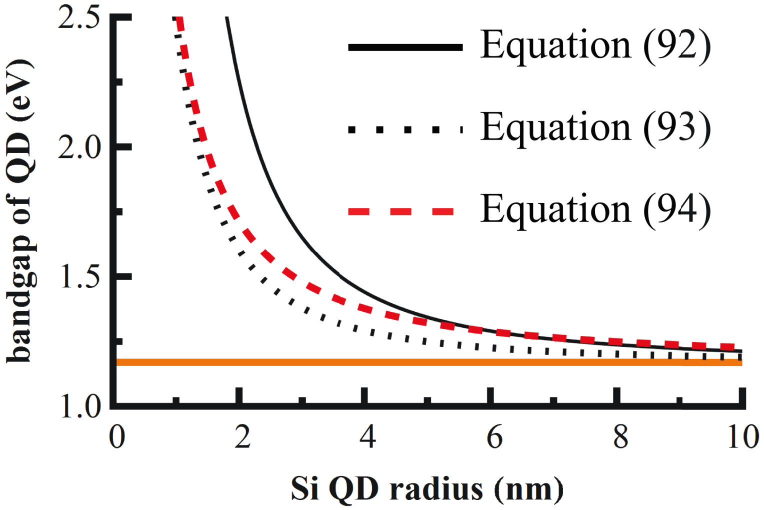

Figure 11. Silicon QD band gap as a function of the dot radius. The solid curve, dotted curve and dashed curve are plotted from Equations (92), (93), and (94), respectively. The horizontal orange line represents the band gap of bulk silicon.

interactions (as evident in the third term on the right). Those formulas are plotted in Figure 11 for a band gap in bulk silicon of 1.17 eV, as used in Ref. [102]. While there is still no general consensus on which equation is the best one to model the silicon QD PL spectrum, the larger band gap for smaller QDs has been experimentally proven. One example is given in Figure 12, which shows that the emission wavelength decreases with smaller particle size [103].

One interesting property of oxide-embedded Si-QDs is the large energy difference between the absorption onset and the luminescence peak, which can approach 2 eV in some reports [96]. This is illustrated in Figure 12 , where we see that the absorbance at the photoluminescence energies is very low. This implies that the absorbing and emitting states may not be the same ones. One possible explanation is that absorption occurs mainly to higher quantized energy levels further up in the valence and conduction bands, followed by thermalization to the lowest excited level before recombination occurs [104]. The attraction of this model is that it is relatively simple and does not require the existence of defect-related emissive centers. However, such centers may also play a significant role in the luminescence spectrum, as suggested by numerous Si-QD oxidation experiments [105, 106, 107, 108, 109, 110, 111].

For Si-QDs, the effect of a surface oxide on the luminescence can be profound [61, 112, 113]. Numerous investigations have shown that oxidation can red-shift the luminescence spectrum, especially in the case of smaller QDs [109, 114]. Considerable

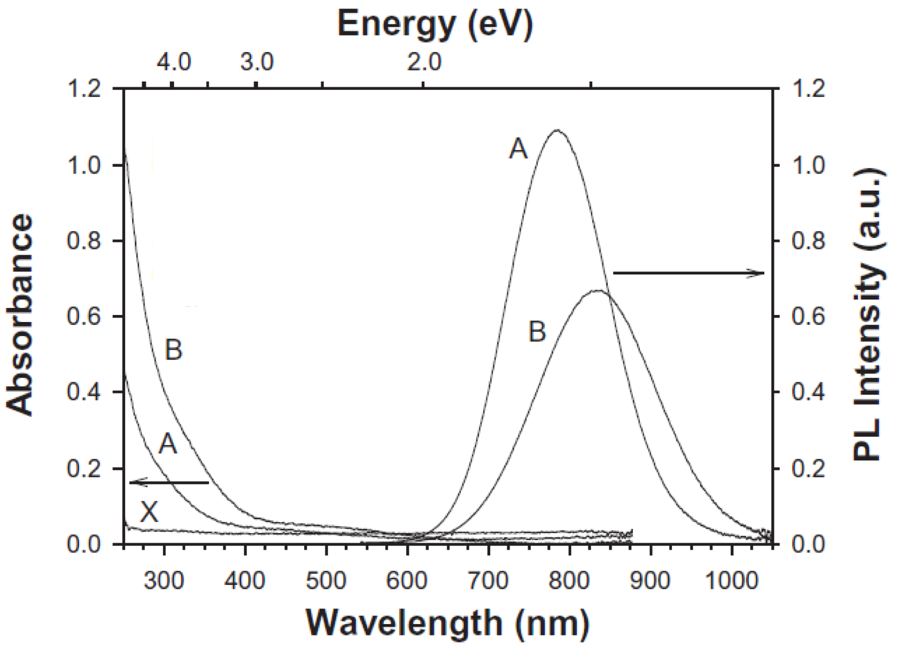

Figure 12. An example of the absorption and luminescence spectra of silicon quantum dots with average diameter of ~ 1.5 nm (A) and ~ 2.4 nm (B). The reference absorption spectrum is marked as X. The absorption and emission energies are quite different. (adapted from Ref. [103]).

experimental and theoretical efforts have been devoted to finding the oxide-related sub-gap states supposed to be responsible, with Si=O-related (double-bond) states suggested as the main culprit in some of the earlier works [109]. More recent investigations have shown that Si-O-Si bridges can also provide luminescent sub-gap centers in the red and near-IR part of the spectrum [114], and these states seem to be more physically stable than Si=O double bonds [110, 115]. While the effects of oxide-related luminescence of Si-QDs are still debated, there seems to be at this point a large amount of evidence that oxidation plays an important role in the emission mechanism [61, 112, 113, 109, 110, 115, 114]. This would cause increasing disagreement between the theoretical models and the experimental results, especially for smaller particles [109].

The quantum efficiency (QE) is another important characteristic of QDs generally. The QE is simply the ratio of emitted photons to absorbed ones, or equivalently, the fraction of the total recombination rate that is purely radiative:

$$\mathrm{QE} = \frac{\text{number of photons emitted}}{\text{number of photons absorbed}} = \frac{1/\tau_r}{1/\tau_{non} + 1/\tau_r}, \tag{95}$$

where τ_r and τ_{nr} are the radiative and non-radiative recombination lifetime, respectively. In the case of Si QDs, the QE is typically 5-6 orders of magnitude higher than that of bulk silicon [116]. One reason for this is that the electron-hole wavefunctions overlap extensively in small QDs, leading to larger radiative rates for smaller particles [117]. A second factor is the lack of spatial connectivity between the particles, which minimizes the effect of nonradiative traps. While the "capture volume" in bulk silicon can be quite large [118], in truly isolated QDs a defect can only quench the one particle in which it is located. Although QDs are probably not truly isolated (i.e., fluorescence resonance energy transfer and tunneling can occur between particles [119]), nonradiative recombination is nevertheless minimized in comparison to bulk silicon. While the quantum efficiency of the particles fabricated in this thesis hasn't been measured, the QE of oxide-embedded Si QDs has been reported to be a few percent [120, 121]. This value is probably limited by Auger recombination, thermal relaxation via phonons, and other nonradiative processes. Some studies have claimed a QE as high as several tens of percent for surface-functionalized Si QDs [122, 123, 117].

In conclusion, Si QDs can be excellent fluorophores for a variety of reasons. First, the fluorescence quantum efficiency can be comparatively high. Second, because the emission spectrum shifts into the visible range (due to quantum confinement), Si-QDs tend to be fairly easy to work with (e.g., infrared detectors are not necessary). Third, Si QDs appear to be biocompatible and show limited toxicity [124, 125, 126], and can be used for drug delivery [127]. In comparison, II-VI (e.g., CdSe) and III-V (e.g., GaAs) compound semiconductors are comprised of toxic elements that can require special procedures during synthesis and analysis. Fourth, Si-QDs show minimal photobleaching compared to conventional organic dyes [128]. Fifth, they may be amenable to silica surface functionalization chemistry [70, 71, 72, 73]. Sixth, an additional attractive feature, although not directly related to this work, is that Si QDs are inherently compatible with silicon-based microphotonic systems and could find applications as a microphotonic light emitter [129]. For many of these reasons (combined with the more practical fact that our group can easily make uniform nonplanar Si-QD coatings) silicon QDs were considered as a good fluorophore for utilization with the microsphere optical cavities investigated in this thesis.

1.4 Refractometric sensing with QD-coated microspheres: basics

1.4.1 Refractometric sensitivity of a coated microsphere

The basis of the sensing mechanism results from the fact that part of the electric field energy extends outside the microsphere and into the surrounding medium. The resonant frequency therefore shifts when the refractive index of the medium is changed; it redshifts if the index increases, and vice versa. Furthermore, absorption or scattering losses in the surrounding medium can decrease the resonance Q factors. These changes represent the transduction mechanisms by which the optical properties of the surrounding medium can be sensed.

At least two figures of merit describe the refractometric sensing ability: (i) the refractometric sensitivity, S, represents the magnitude of the wavelength shift per refractive index change of the outside medium; and (ii) the detection limit describes the minimum detectable change in the external index. Here, we will briefly discuss the basic mechanisms that control the sensitivity. This description is based on the work of Teraoka and Arnold, who, in a series of four papers [75, 76, 130, 131], developed a perturbation-theory approach to quantify the sensitivity of layered microspheres.

The basis of the theory is to calculate the effect of a "perturbation" in the surrounding medium. Essentially as the refractive index of the medium shifts by an amount dn, one wishes to calculate the fractional resonance wave vector shift δk with respect to the initial resonance wavevector k_0. If the perturbation can be represented by a uniform change of the refractive index, the fractional wavevector shift can be written as [75, 76, 130, 131]:

$$\frac{\delta k}{k_0} = \frac{d\lambda}{dn} = -\frac{\text{energy perturbation}}{2 \times \text{electric energy}} = \frac{\int_{V_p} \delta\epsilon_r \mathbf{E}_0^* \cdot \mathbf{E}_p d\mathbf{r}}{2\int_V \epsilon_r \mathbf{E}_0^* \cdot \mathbf{E}_0 d\mathbf{r}}, \tag{96}$$

where V is the volume of the surroundings, V_p is the perturbation volume where the refractive index changes, $\mathbf{E}_0$ is the electric field before the perturbation, and $\mathbf{E}_p$ is the perturbed field within V_p. This integral can be taken to some arbitrary limit (e.g., spherical volume corresponding to 100 times the radius of the microsphere) to avoid the divergence. Teraoka and Arnold showed how Equation (96) can be solved for a microsphere with a high-index layer [130, 131]. The refractometric sensitivity is then given by:

$$S_{TE} = \frac{d\lambda}{dn} = \frac{\lambda n_3 I_3}{n_1^2 I_1 + n_2^2 I_2 + n_3^2 I_3}, \tag{97}$$

and

$$S_{TM} = \frac{\lambda}{dn_3} \cdot \frac{2n_3 dn_3}{2n_3^4 k^2 (I_1 + I_2 + I_3)} n_3 k [d_l^2 \xi_l^{(1)}(n_3 kz) \xi_l'^{(1)}(n_3 kz) + n_3 k I_3], \tag{98}$$

for the TE and TM polarization, respectively, where I_i is the energy density in the i^{th} layer, and $d\lambda$ is the resonant wavelength difference due to the index change dn. The refractive indices are n_1, n_2 and n_3, and $\xi_l'^{(1)}(x)$ is the derivative with respect to the argument x of the Riccati-Hankel function of the first kind. The energy density terms I_1, I_2, and I_3 can be found by numerical integration of the following expressions:

$$I_1 \equiv \int_0^{a-t} A_l^2 [\psi(n_1 k r_0)]^2 dr \tag{99}$$

$$I_2 \equiv \int_{a-t}^{a} [B_l \xi_l^{(2)}(n_2 k_0 r) + C_l \xi_l^{(1)}(n_2 k_0 r)]^2 dr, \tag{100}$$

and

$$I_3 = \int_a^{\infty} [D_l \xi_l^{(1)}(n_3 k_0 r)]^2 dr, \tag{101}$$

where A_l, B_l, C_l, D_l, and k_0 are defined by solving Equations (40-44). The capital letters in Equations (99)-(101) can be replaced by small ones to indicate the TM polarization. The sensitivity is dependent on the refractive index and size of the microsphere, as well as on the optical properties of the coating and the external medium.

1.4.2 Effect of high index layers

The refractive index and thickness of the coating applied to the microsphere will influence the sensitivity and detection limit. The microspheres used in this thesis will be made of silica glass ($n_1 = 1.452$). The refractive index of the Si QDs coated on the microsphere is $n_2 = 1.67$ and the extinction coefficient is $\kappa = 0.0006$ [132] in the spectral range of 700-900 nm. To investigate the effect of the thickness on the

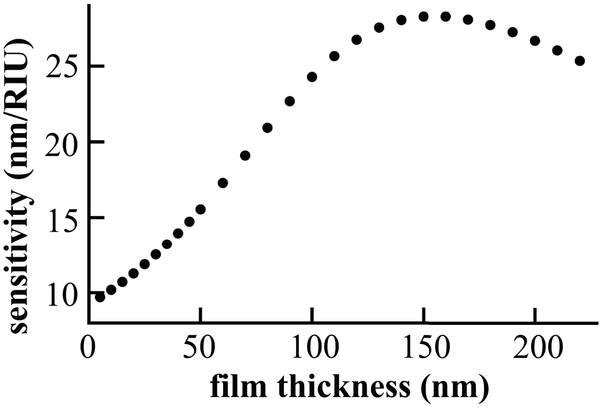

Figure 13. The refractometric sensitivity for a 10-µm-radius microsphere, as a function of the coating thickness. The radial number and azimuthal number of the TE polarized WGM is $n = 1$ and $l = 112$, respectively. The optimal film thickness to obtain the highest sensitivity for this microsphere is $\sim$ 150 nm.

sensitivity of the microsphere, the sensitivity was calculated for QD layer thicknesses ranging from 5 nm to 200 nm, on a 20-µm-diameter microsphere (Figure 13). The sensitivity curve is not linear as a function of QD layer thickness, but reaches a maximum when $t \sim 150$ nm. This effect was discussed in Teraoka and Arnold's work [130], and is attributed to the way the high-index layer affects the field distribution inside and outside the microsphere. The important point, however, is that control of the layer thickness can, in principle, be used to maximize the refractometric sensitivity of a QD-coated microsphere.

1.5 Thesis organization

This thesis will discuss the fundamental properties of the photoluminescence whispering modes in a microsphere coated with silicon quantum dots. Sensing applications for these structures will also be studied. The format of the thesis will be arranged as follows:

- Chapter 2 will outline the experimental methods used to synthesize the microspheres and to coat them with a layer of Si QDs. The optical characterization methods will also be discussed in detail, as well as the data analysis techniques.

- Chapter 3 will focus on a detailed comparison of the luminescence WGMs with the "cold cavity" mode structure. In other words, using evanescent coupling techniques, the true mode structure of the microsphere will be measured. This result will be compared to what is observed in a fluorescence spectrum from the same microsphere, and the reasons for the (large) differences will be discussed.

- Chapter 4 will be a thermal characterization of the fluorescence WGM shifts. Thermal drift (due to laser-induced heating or laboratory temperature fluctuations) can be an important factor that controls the ultimate detection limit of WGM-based sensor devices. This effect will be quantified by varying the temperature around a microsphere and measuring the thermal shifts for different solvents.
- Chapters 5 and 6 will focus on refractometric measurements. Two different setups will be used: in one case a QD-coated microsphere will be inserted directly into a cuvette in which different solutions are added, and the mode shifts will be measured. The second setup developed in this work involves inserting the microsphere into a square capillary, into which analyte solutions are injected with a syringe pump. The results will be compared with theory and the optimal detection limits for these devices will be investigated.
- Chapter 7 will consist of a short conclusion and look toward the future for WGM-based sensors.

Chapters 2-6 form the basis of several published papers. However, revisions were done in order to bring the work into a more “cohesive” thesis-based format.

2. Experimental methods

This chapter was modified from the paper published in the proceedings of the SPIE 9288, 92880Y (2014) by Y. Zhi and A. Meldrum.

2.1 Fabrication of microspheres coated with Si-QDs

In this section, the methods used to fabricate single silica microsphere will be illustrated. A step-by-step procedure will be provided in detail, as many of the methods had to be developed “in house”.

2.1.1 Fabrication of microspheres

The basic process used to fabricate a microsphere involved melting an optical fiber. Standard OZ Optics 780-nm-single mode fiber (SMF-780-5/125-0.25-L) was used for most samples, although the exact type of fiber used didn't affect the final product. Approximately 10-cm-long sections were cut from the spool, and then the fiber jacket and buffer were stripped off. The bare fibers were then cleaned with denatured alcohol to remove residual debris, and were transferred to an optical setup used for melting glass fiber (Figure 14(a)).

A single piece of cleaned fiber was next prepared for the melting process. The fiber was attached to a linear translation stage (MT-XYZ from Newport) so that it could be moved into the focus of the laser. One end of the fiber was inserted into a groove that was machined into a small clamp made for holding the fiber. A thin metal sheet covers the groove and is tightened by a screw to fix the fiber vertically in place (inset of Figure 14(a)). A metal washer was affixed with scotch tape to the bottom of the fiber, to be used as a weight. The grooved clamp can be screwed onto an optical post and attached to the linear translation stage. A webcam was placed nearby in order to observe the fiber during the melting process.

To fabricate the microsphere, a CO_2 laser was used to melt a small region of the fiber. The laser employed in this work is the ULR-10 by Universal Laser Systems, which has a maximum average power of 10 W at a pulse frequency of 5 kHz. To begin, one needs the beam of the CO_2 laser to be incident around the middle of the fiber length. A set of gold mirrors and chalcogenide lenses compatible with the 10.6 µm radiation of the laser was used to focus the beam near the correct location on the fiber. To achieve sufficient heating and melting of the glass fiber, this laser needs to be operated fairly close to full power. Initially, the fiber translation stage and alignment mirrors were used to bring the beam incident roughly in the middle of the fiber. The CO_2 laser is equipped with a visible red diode laser to mark the beam path. When the guiding laser beam was centered, the pulsed CO_2 beam was turned on and small positioning adjustments were made by finely tuning the translation stage. Once the fiber is at the focus of the laser light, it starts melting and begins to stretch (Figure

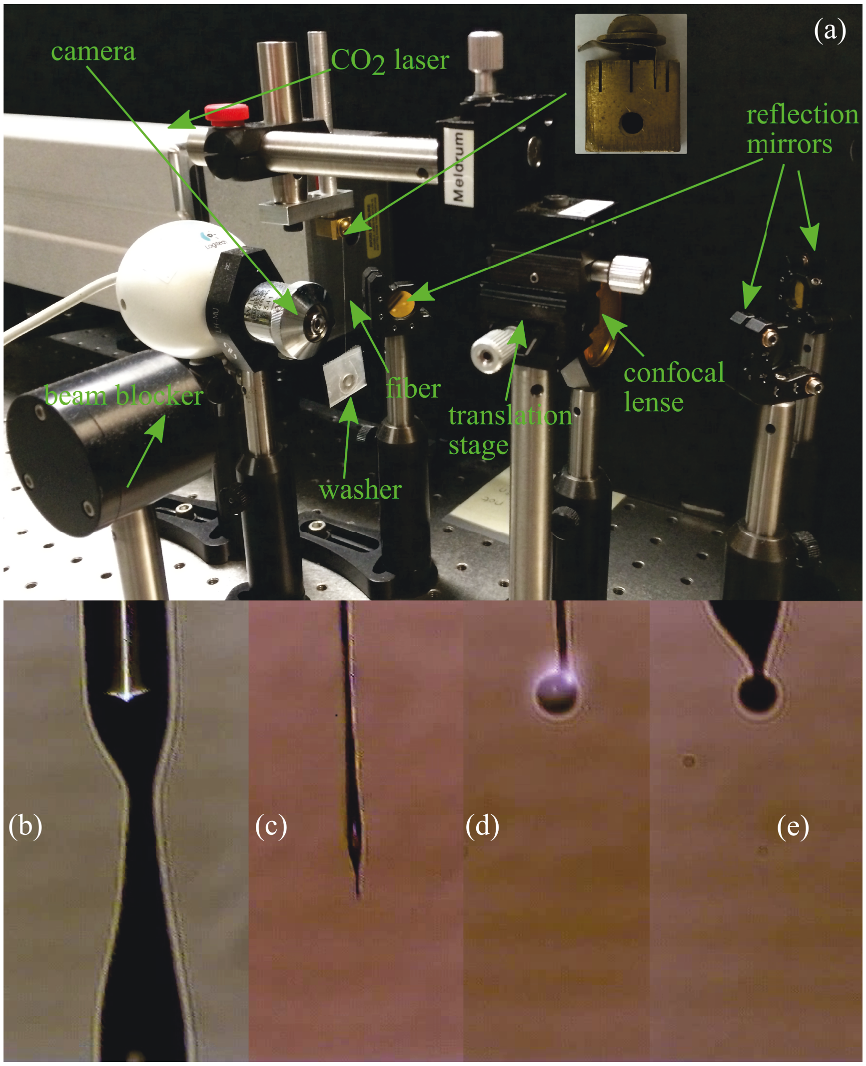

Figure 14. (a) Optical setup for making a microsphere. A CO_2 laser beam is focused on a bare fiber using a simple optical setup. A webcam is used to monitor the fabrication process. (b) The fiber starts stretching when the beam strikes the fiber. (c) A fiber taper is fabricated. (d) A melt region forms on the end of the taper. (e) A solid microsphere is formed.

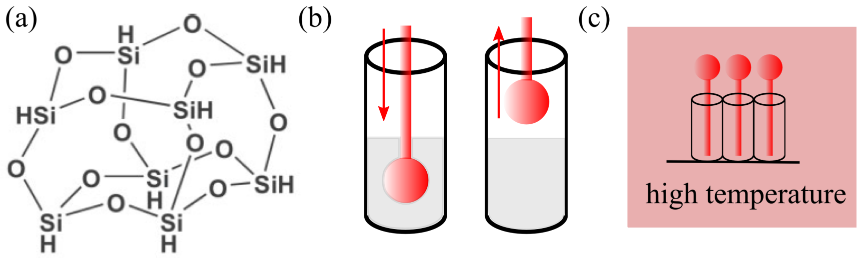

Figure 15. (a) Diagram showing the structure of hydrogen silsesquioxane, adapted from Ref. [134]. (b) Graphic illustrating a microsphere being dipped into the HSQ solution for ∼ 30 s; and (c) then annealed in a furnace at 1100 °C for 1 hour.

14(b)).

Once the fiber stretched or tapered by ∼ 5 cm, the laser power is increased in order to cut the fiber in half (see Figure 14(c)), dropping the washer part onto the table. Next, the end of the taper is brought into the focus of the laser by using the linear translation stage to move the fiber holder. Once the taper is within the laser focus, a spherical shape begins to form on the end of the taper as it starts to melt (Figure 14(d)). One then slowly lowers the taper using the translation stage, thereby adding material to the melt until the desired sphere size is achieved. When the sphere reaches the desired size, the laser is turned off and the melt forms a solid microsphere which remains attached to the leftover fiber via a narrow neck (Figure 14(e)). The remaining fiber can be carefully removed from the holder, taking care not to allow the sphere to touch any external objects, as the neck region is fragile.

2.1.2 Quantum dot fabrication

Si QDs can be chemically synthesized on the surface of a microsphere using the "HSQ-method". This method is based on thermal annealing of hydrogen silsesquioxane (HSQ), using a technique developed in Ref. [133]. HSQ is the name given to the cage-like $H_8Si_8O_{12}$ molecule (Figure 15(a)) , which forms a translucent solid at room temperature and can be dissolved in a variety of solvents. The most common form of HSQ is trademarked under the name FOx-## from the Dow Corning company, which is sold as a negative resist for electron beam lithography. The name stands for "Flowable Oxide" followed by a two-digit number. The FOx 1# series uses methyl isobutyl ketone (MIBK) as a solvent. In this work, FOx-15 (HSQ concentration of 15–35% in weight in MIBK) was used to coat the microspheres.

Unfortunately, FOx solutions are fairly difficult to work with. First, they are expensive (typically ∼ CA\$ 1000 for a 125 mL bottle); second, the solution is highly sensitive to air, heat, and moisture. If the bottle is left open to the atmosphere, it tends to thicken and gel in the space of a few hours or days, depending on humidity levels. Thus, for the present work, the bottle of FOx was always stored in a glove box filled with argon. In order to coat the microsphere, a small aliquot was transferred into a sealed vial in the glove box. The vial was transported to the furnace and opened (in air). The microsphere was dipped to a depth of ∼ 1 cm by manually holding the end of the fiber stem. After holding the sphere in the solution for ∼ 30 s (Figure 15(b)), it was then withdrawn and transferred immediately to the annealing furnace (Figure 15(c)). If the FOx solution spends much time in air, the microsphere tended to have weak fluorescence, possibly due to chemical changes that occur when HSQ is exposed to moisture.

Annealing at temperatures of 1000 °C or higher is known to drive off the MIBK solvent and collapse the cage structure of the HSQ molecules [133], forming a thin solid coating. The coating is nominally SiO_x with x close to 1.5. The exact composition depends on the amount of silane driven off during annealing, which seems to be dependent on the heating rate [135]. At high temperatures the $SiOx$ phase segregates into a mixture of Si nanoparticles in an SiO_2-like matrix. In this work the samples were heated at a ramp rate of 55 °C/minute up to a temperature of either 1000 or 1100 °C. Forming gas (a mixture of 95% N_2 with 5% H_2) was used as the annealing atmosphere, as hydrogen is known to passivate the QDs and produce a brighter fluorescent film [136]. A glass crucible with slots was fabricated to hold the fibers vertically as they were raised into the hot zone of a vertically-oriented furnace (Figure 15(c)) (A tube furnace, in contrast, requires some means of holding the fibers vertically without allowing the sphere end to come in contact with any surface). After one hour at high temperature, the samples were allowed to cool back to room temperature over a period of about 2 hours.

If a thicker QD coating is required, the dipping and annealing process can be repeated. When the films approach ∼ 2 µm in thickness, they begin to peel and delaminate from the glass surface [133]. Up to four sequential coatings were used without degradation of the WGMs (see Chapter 6). Other means to control the film thickness include chemical etching and varying the HSQ concentration in the FOx solution, but we have not investigated these in detail. The lower annealing temperature was ultimately found to produce less “drooping” of the fibers, but also resulted in a slightly weaker fluorescence.

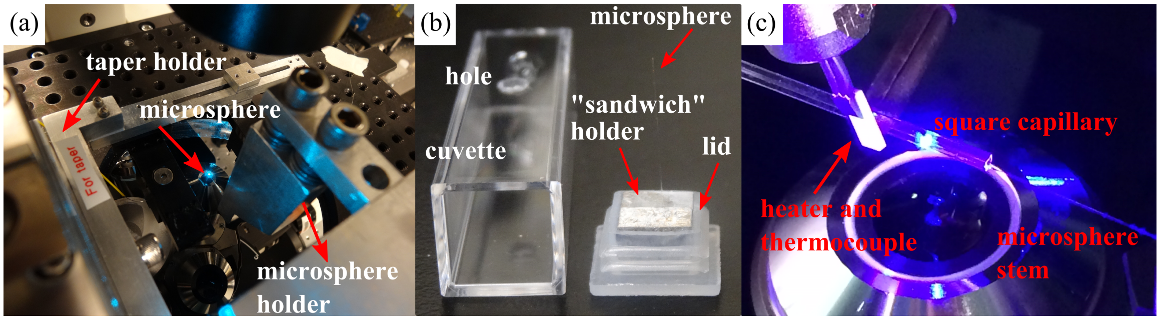

Figure 16. Basic setup for the fluorescence measurements. (a) A microsphere is held in air on the microscope stage, and an Ar^+ laser (Coherent Inc. Innova 70C) is focused onto the sphere (the bright blue dot in the center of the photograph). (b) The cuvette lid with the metal "sphere holder", for inserting the sample into a cuvette. The microsphere may be barely visible extending vertically upward from the center of the holder. (c) A microsphere is inserted into a square capillary into which the analyte solution can be pumped. A heater and thermocouple are placed beside the capillary for investigating the thermal response of the WGMs. In this setup, a HeCd laser (Omnichrome LC-500) passes through one face of the capillary and is incident on the microsphere.

2.2 Photoluminescence spectroscopy

In this section, the apparatus used to collect the luminescence spectrum on a microscope stage will be described. Next, the various calibrations and corrections will be discussed, followed by the methods used to obtain the WGM spectral shifts.

2.2.1 Data collection

For photoluminescence (PL) spectroscopy, the coated microsphere was mounted onto a microscope stage. For experiments conducted in air, a simple stage was built to hold the microsphere over the objective lens of the inverted Nikon TE2000e epifluorescence microscope (Figure 16(a)). The stage is made of aluminum, with a hole drilled into one end and threaded to hold a magnetic steel screw. A straight groove was cut in the center of the stage, directly above the threaded hole, for holding the fiber stem. A small rare-earth magnet was affixed to a rubber pad and was used to hold the stem in the groove, with the microsphere end of the fiber extending horizontally over the objective lens. A few tapped and threaded holes were added to the holder so that it could be attached to an XYZ piezo-controlled optics stage.

For experiments in which the medium outside the microsphere needed to be a solution, the microsphere was placed inside a 3.5 mL cuvette. To do this, a "sandwich" holder was machined to hold the microsphere horizontally in the cuvette. Essentially, an aluminum block was fixed into the lid of the cuvette. The block was cut in two pieces and grooved such that it would clamp the fiber stem and hold it securely without breaking it. A mounting wax (Quickstick$^{\text{TM}}$ 135 from South Bay Technology Inc.) was used to help ensure that the sphere "stuck" into the groove. The holder, with the microsphere extending from it, was pushed into the cuvette in order to form a sealed cap, and the whole apparatus was mounted "horizontally" above the objective lens. A hole was drilled on one of the side surfaces of the cuvette, at the end far away from the microsphere, through which fluids could be added or removed from the cuvette using a pipette or syringe (Figure 16(b)). Since the cuvette was held horizontally above the objective, this hole would be on the "top" face.

To build up a microfluidic system for sensorgram-type measurements, a square capillary (catalog# 8270-050 from VitroCom) with an inner cross-sectional length of ~ 700 µm was used instead of the cuvette. The idea was to insert the microsphere into the capillary, and then pump fluids inside. Since the capillary surfaces are flat, one avoids lensing effects that were found to be especially problematic when using round capillaries (Chapter 5). The square capillary and the microsphere were mounted onto 3-axis motion controllers (Newport 562 series and Thorlabs RB13MP), with the sphere held as described above for the "air" experiments (Figure 16(c)). One end of the capillary was then glued to a polyethylene tube (Becton Dickinson PE190) which was connected to a syringe attached to a micro-pumping system (Chemyx NanoJet). The microsphere was then carefully inserted into the other end of the capillary. This requires some care, since it is easy to "crash" the sphere into a capillary wall, which usually breaks it off the fiber stem.

Obviously this geometry presents a problem with respect to fluid disposal. We could not find a very satisfactory solution to this problem; here, we simply used a "waste cuvette" taped to the side of the objective lens and positioned the capillary so that the fluid waste would drop into the cuvette. A heater and a thermocouple, which were connected to Thorlabs TC200 temperature controller, were placed close to the capillary for experiments characterizing the WGM thermal response.

2.2.2 Calibration of the PL spectra

In order to obtain the fluorescence WGM spectrum, we use a spectrograph with a "mirrored slit" geometry. The basic idea is that the entrance slit is held at 45° with respect to the spectrometer entrance. Part of the image passes through the slit and goes into an imaging spectrometer; the part that is reflected is simultaneously collected by

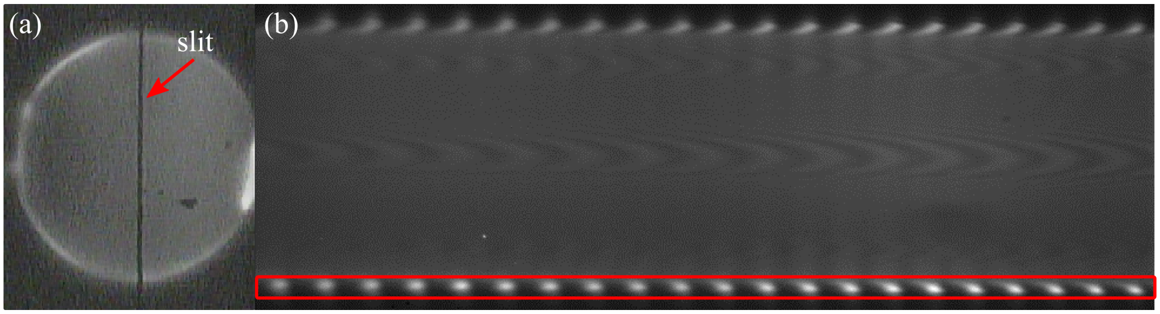

Figure 17. (a) A fluorescence image captured by the TV camera, on which the "slit" bisects a microsphere. (b) The corresponding spectral image of the microsphere. A 1-dimensional spectrum was extracted from the lower "edge" of the sphere by vertical binning of the region within the red box.

a TV camera. The camera image thus contains a dark line (the slit) superimposed on the microscope image. This geometry was particularly advantageous, since it permits fluorescence imaging and spectroscopy at the same time (Figure 17). The stage can be moved until the slit bisects the microsphere perpendicular to the stem direction (Figure 17(a)). A spectral image can then be collected, which represents a "spectral cross section" through the center of the sphere (Figure 17(b)). Typically, 5-30 seconds are needed to collect a reasonably bright spectrum. The resulting spectral image shows a periodic intensity variation (Figure 17(b)), predominantly in the regions corresponding to the "edges" of the sphere, as viewed in the fluorescence image. These are the WGMs.

To extract a 1-dimensional spectrum, one can either take a line intensity profile across the spectrum, or a box profile (e.g., vertical binning of a portion of the spectral image in Figure 17). Wavelength calibration was then done using an HgAr lamp to convert the horizontal axis to a wavelength scale. For detecting small shifts in the WGMs, care must be taken to ensure that the wavelength calibrations are always performed on the same pixel "box" on the calibration image from which the data on the spectral image is taken. This avoids systematic shift errors arising from the fact that the imaging system cannot project the spectrum perfectly horizontally on the CCD (i.e., there is typically a small, mostly vertical curvature due to the spectrograph optics).

In order to calibrate the wavelength, we start with the spectral image of an HgAr source, relating the observed spectral lines to a table of known lines (Figure 18). Since the grating within the spectrograph unit can be rotated, it was generally necessary to first ensure that the grating was centered within the wavelength range of the

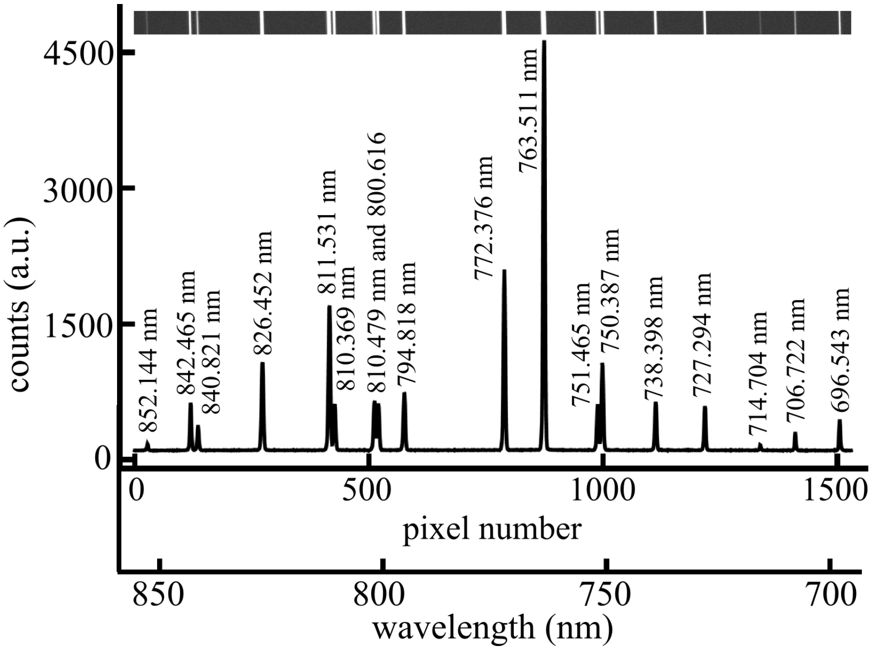

Figure 18. The top spectral image shows the spectral lines for the HgAr lamp, taken by the spectrometer. The extracted 1-dimensional profile are plotted for both pixel and wavelength scales. The wavelength are converted from the pixels via Equation (102).

photoluminescence. Then a calibration image was taken, and the observed spectral lines were identified. The spectrum on the CCD is actually reversed from its usual "orientation" (i.e., longer wavelength on the left of the spectral image). The horizontal pixel number on the spectral image is nearly linear with wavelength, so all wavelengths between the observed spectral lines were obtained by a simple linear interpolation:

$$\lambda(p) = m_p \cdot p + b_p \tag{102}$$

where m_p and b_p are the slope and intercept of the linear relationship between wavelength and pixel number, p. The slope is extrapolated from two spectral lines according to $m_p = [\lambda(p_1) - \lambda(p_2)]/(p_1 - p_2)$, where $\lambda(p_1)$ and $\lambda(p_2)$ are the two known calibration wavelengths on pixel p_1 and p_2, respectively. The intercept b_p is the wavelength corresponding to the first pixel in the spectrum. For this work, the conversion was $\lambda(p) = -0.105 \cdot p + 855.666$ in nm obtained from the spectrometer (SBIG SGS) (Figure 18). The negative sign reverses the spectrum (from short to long wavelength).

The second correction concerns the efficiency of the spectral system. The intensity correction isn't strictly necessary for characterizing the WGMs, which appear as sharp peaks, but it does affect the overall shape of the spectrum. The efficiency of the

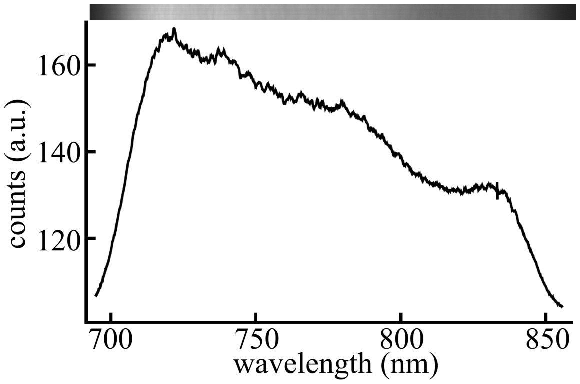

Figure 19. The spectral image of the blackbody source with a color temperature of $T = 3100$ K (average of 400 spectra). The 1-dimensional profile is extracted from the spectral image using the method illustrated in Figure 17.

spectroscopy system can be accounted for by calculating a "corrected" spectrum $I(\lambda)$ according to:

$$I(\lambda) = B(\lambda) \cdot \frac{I_s(\lambda) - I_b(\lambda)}{I_{bb}(\lambda) - I_b(\lambda)}, \tag{103}$$

where $I_s(\lambda)$, $I_{bb}(\lambda)$, $I_b(\lambda)$ represent the sample luminescence intensity, the intensity of a standard blackbody source, and the background intensity, respectively. $B(\lambda)$ is simply obtained from Planck's law for the known color temperature of a standard blackbody radiator (The LS1 blackbody light source: color temperature of 3100 K):

$$B(\lambda) = \frac{2hc^2}{\lambda^5} \cdot \frac{1}{e^{\frac{hc}{\lambda k_B T}} - 1}, \tag{104}$$

where k_B is the Boltzmann constant, h is the Planck's constant, c is the speed of light, and T is the temperature.

One difficulty was encountered in the blackbody corrections. For much of the present work, the integration time for the PL spectra was on the order of $\sim$ 20 s. Since the blackbody light source was much brighter than the luminescence, the pixel counts were much higher than they were in the samples. In several tests, the response of the spectrograph proved to be not perfectly linear with intensity. This means that an accurate correction requires the standard blackbody source and the sample spectra to have similar intensities. To deal with this issue, the blackbody lamp was turned down to match the intensity levels of the sample. However, the signal-to-noise ratio (SNR) then becomes quite low. To improve the SNR, the final blackbody spectral image was taken by averaging 400 spectra with intensities similar to that of the sample to maximize the SNR ratio in the blackbody spectrum (Figure 19).

2.2.3 Data analysis

Fourier shift theorem

For refractometric sensing with a microsphere, one needs to measure the frequency or wavelength shift associated with changes in the refractive index of the surrounding medium (see Chapter 1.4). Thus, one must identify the peak wavelength, λ_0, of the resonance, and observe how it "shifts" when the composition of the external medium changes. In the past, this was usually accomplished by curve fitting to a single WGM peak [137] (e.g., a Lorentzian fitting). Sometimes the method used to find the peak isn't stated in the literature [138, 139, 140]. In the present work, Fourier methods were used to track the resonance phase shifts instead [141]. The fluorescence WGM spectrum is periodic and therefore lends itself naturally to Fourier analysis methods.

The WGM spectrum is periodic in frequency, and nearly periodic in wavelength for high angular orders. For a periodic spectrum in which the number of data is N, and $I(f_p)$ is the intensity at frequency f_p, the spectrum can be modeled as the sum of its Fourier components. Ultimately, wavelength shifts obtained by using the Fourier shift theorem are much smaller than the pitch of the CCD.

The discrete Fourier transform (DFT) theorem is given by,

$$I(f_p) = \frac{1}{N}\sum_{n=0}^{N-1} F_p \cdot e^{i2\pi \frac{p}{N\cdot\Delta f} f_p}, \tag{105}$$

where $p = 0, 1, \cdots, N-1$ is pixel number in the 1D spectrum, Δf is the sampling rate, and

$$F_p = \sum_{p=0}^{N-1} I(f_p) \cdot e^{-i2\pi \frac{p}{N\cdot\Delta f} f_p}. \tag{106}$$

$|F_p|^2$ is called the power of the p^{th} Fourier component, which represents the weight of this component in the spectrum.

When the spectrum remains identical except for a uniform shift, f_s, in frequency, F_p becomes

$$F_p = \sum_{p=0}^{N-1} I(f_p + f_s) e^{-i2\pi \frac{p}{N\cdot\Delta f} f_p}. \tag{107}$$

If we let $x = f_p + f_s$, Equation (107) can be written as

$$F_p = \sum_{p=0}^{N-1} I(x) e^{-i2\pi \frac{p}{N\cdot\Delta f}x} \cdot e^{i2\pi \frac{p}{N\cdot\Delta f}f_s} \tag{108}$$

Comparing Equation (106) to (108), the only difference is a phase shift included in the last term $e^{i2\pi \frac{p}{N\cdot\Delta f}f_s}$. The phase shift can be expressed as

$$\Delta\varphi = 2\pi p f_s/(N\cdot\Delta f). \tag{109}$$

Therefore, the frequency shift can be obtained:

$$f_s = \frac{N\cdot\Delta f}{2\pi p}\Delta\varphi. \tag{110}$$

Since $N\cdot\Delta f = f_{max} - f_{min}$, where f_{max} and f_{min} are the maximum and minimum frequency in the spectrum, Equation (110) becomes

$$f_s = \frac{f_{max} - f_{min}}{2\pi p}\Delta\varphi = \frac{f_{max} - f_{min}}{2\pi}\cdot\Delta\varphi_p \tag{111}$$

where $\Delta\varphi_p = \Delta\varphi/p$. $\Delta\varphi$ is linearly dependent on p, so $\Delta\varphi_p$ is a constant, and can be obtained from the linear fitting of the plot of $\Delta\varphi$ versus p. $\Delta\varphi_p$ is directly related to the phase shift over the whole spectrum.

Shift theorem on WGMs

If we assume that the only spectral change is a "pure shift" when the external refractive index is changed, then the shift theorem will exactly trace the phase shift. In real data, of course, there will be noise; as well, the assumption of a "pure shift" may not be strictly valid since the WGM visibility and Q factor can be affected by changes in the medium. However, these effects are very minor when the refractive index changes are small.

Since the method required to extract the wavelength shifts in the WGM spectrum is a multi-step process, it is given here as a step-by-step procedure. The shift theorem is applied on a PL spectra of a Si-QD-coated microsphere (Figure 20) as an example.

1. The experimental spectra are converted from wavelength units to frequency units. This is to ensure a constant FSR, although for high angular orders the FSR is virtually constant in wavelength in any case. The frequency axis can be simply converted to wavelength by $f = c/\lambda$, and the spectral intensity is given by $I(f) = (\lambda^2/c)\cdot I(\lambda)$.

2. The discrete Fourier transform requires a uniform data sampling. Since the CCD uniformly samples in wavelength, the conversion to frequency will not produce

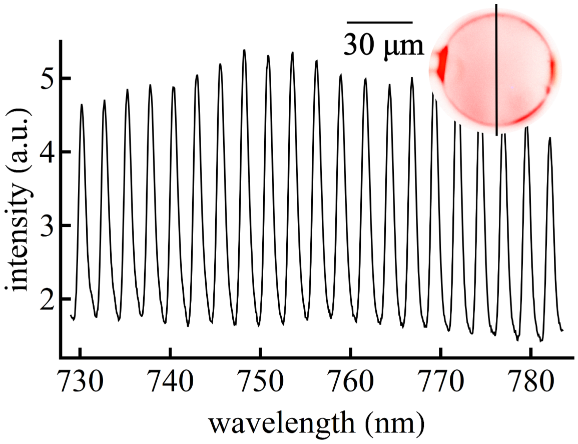

Figure 20. Fluorescence spectrum (TE polarized) of a microsphere with a diameter of 50 µm, showing sharp, periodic WGMs. The inset is the PL image captured by an HD color camera (from Retiga Exi Fast 1394), with the background color inverted from black to white.

uniform sampling. Thus, the frequency spectra are interpolated linearly in order to obtain a uniform sampling rate.

3. The first WGM spectrum is chosen as the reference spectrum from which all shifts are measured.

4. The phase differences $\Delta\varphi$ and the power $|F_p|^2$ for all the p components are obtained (Figure 21). The components with both high frequencies (component with large p) and low frequencies (component with small p) are filtered out, because they represent noise and uncoupled PL background, respectively (Figure 21). Only a few components with $|F_p|^2$ larger than 25% of the strongest one are used to find $\Delta\varphi_p$ (Figure 21). $\Delta\varphi_p$ is then found using a weighted linear fit of $\Delta\varphi$ versus p, with the weighting proportional to the power in that component.

5. The frequency shifts, f_s, calculated via Equation (111) can be converted to wavelength shifts simply by the relationship $\lambda_s = c \cdot f_s/f^2$, where f is the average frequency over the spectra.

2.3 Evanescent measurements

In this section, the apparatus used to fabricate a tapered fiber and a sample "recipe" will be presented. Next, the setup for the evanescent measurement will be described, followed by the fitting methods used to find λ_0 for a transmission WGM.

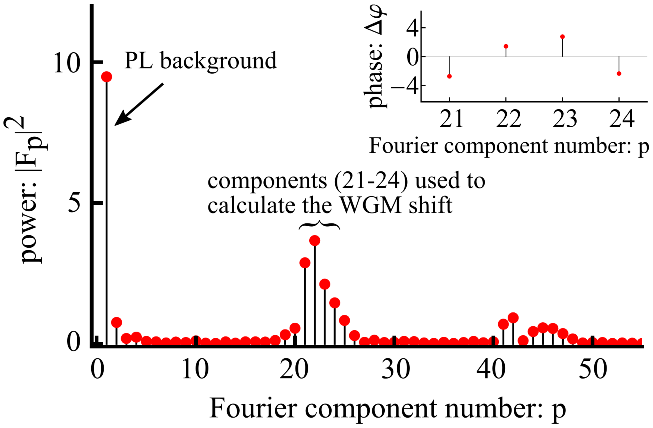

Figure 21. Power spectra corresponding to the PL WGM spectrum in Figure 20. The inset shows the phase spectrum for the components with at least 25% of the power in the main one (#22 in this case).

2.3.1 Fabrication of tapered fibers

Tapered fibers were fabricated using standard heating and pulling methods. The fiber to be tapered was cleaved to a length of ~ 5 cm, stripped and cleaned, and was placed into a set of motorized clamps used to pull or stretch the fiber (Figure 22). A hydrogen torch (MG-25 from Arizona HydroGen Manufacturing Inc.) was used to heat a section of the fiber while the motors pulled the fiber. Light from a tunable laser (e.g., New Focus TLB-6700) was coupled into the fiber during the pulling process, and the transmission was monitored with a photodiode interfaced to an standard oscilloscope (Tektronix TDS5032B). When the heating and pulling begins, the transmission through the fiber oscillates fairly wildly and overall starts to decrease. These oscillations are likely due to multiple mode interference which evolves as the fiber thins. When the fiber gets thin enough that it can support only a single mode, these oscillations stop and the net transmission remains quite weak. At this point, the torch is turned off and the motors are stopped.

During the tapering procedure, the hydrogen torch moves “back and forth” along the length of the taper (Figure 22), while the motors pull the taper at a certain speed. The torch motion and pulling speed are both controllable parameters. While the exact speeds and torch motions to produce the best taper vary over time (e.g., due to gradual changes in the torch as the electrolyte solution ages, or other external factors), the “recipe” tended to work well for most cases is shown in Figure 23.

The parameters in Figure 23 need some explanation. The x-axis is parallel to the fiber. The shortest distance between the fiber and the torch defines the y-axis (where

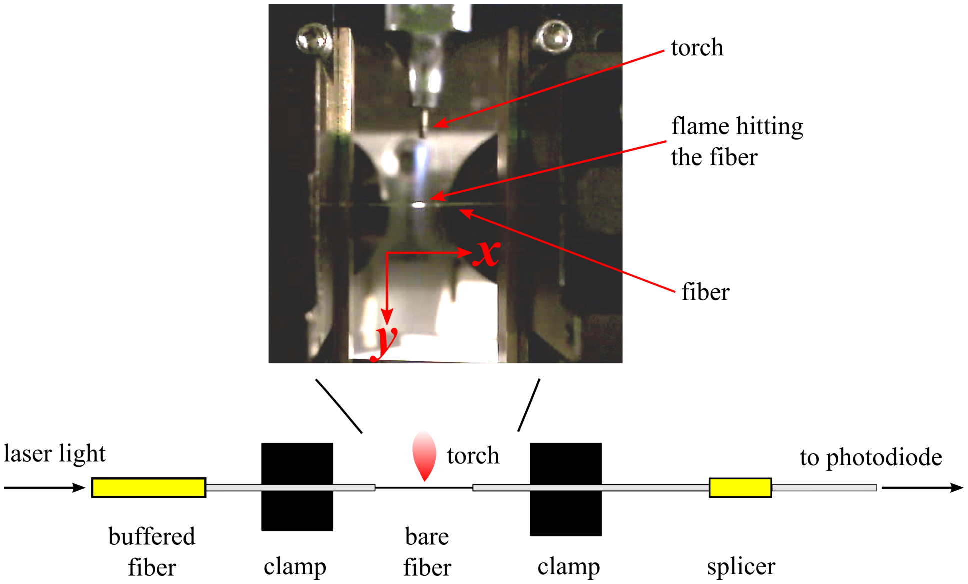

Figure 22. Illustration of the fiber pulling setup. The upper part of the figure is a photograph of the torch as it hits a fiber.

the initial distance is marked as $y = 0$ cm). The pulling parameters in this recipe (Figure 23) are set as follows. The "Pulling speed" is 0.0200 mm/s, and the "Torch speed" as it sweeps along the fiber is 4.50 mm/s. The "Torch Y base position" is 6.90 cm away from the initial position (i.e., closer to the fiber by 6.90 cm). The "Torch Y relative position" (in cm) is added to set a time-variable torch position relative to the "torch Y base position"; it is represented by a formula:

$$y = \begin{cases} 6.90 - 0 = 6.90 & 0 < t < 350 \\ 6.90 - 0.2 = 6.70 & 350 \leqslant t \leqslant 400 \\ 6.90 - 0.3 = 6.60 & t > 400 \end{cases}, \tag{112}$$

where t is the elapsed time since the pulling process started.

The next set of parameters is as follows. The "Torch X center" (in cm) locates the central point along the fiber length. This may take some trial and error to set. The "Torch X relative position" (in cm) is a distance away from the "Torch X center". The "Initial hot zone length" (in mm) defines the x-distance over which the motors will sweep the torch as it heats the fiber. It is set here to 5.0 mm. The entry under "Hot zone length" allows the hot zone to be changed as a function of time. Here it is set to start at the "Initial hot zone length", and will shrink an amount given by $t/8$ (measured in mm) with t in seconds. The "Hot zone length" can never go smaller than the "Minimum torch amplitude" (in mm), irrespective of what value the "Hot

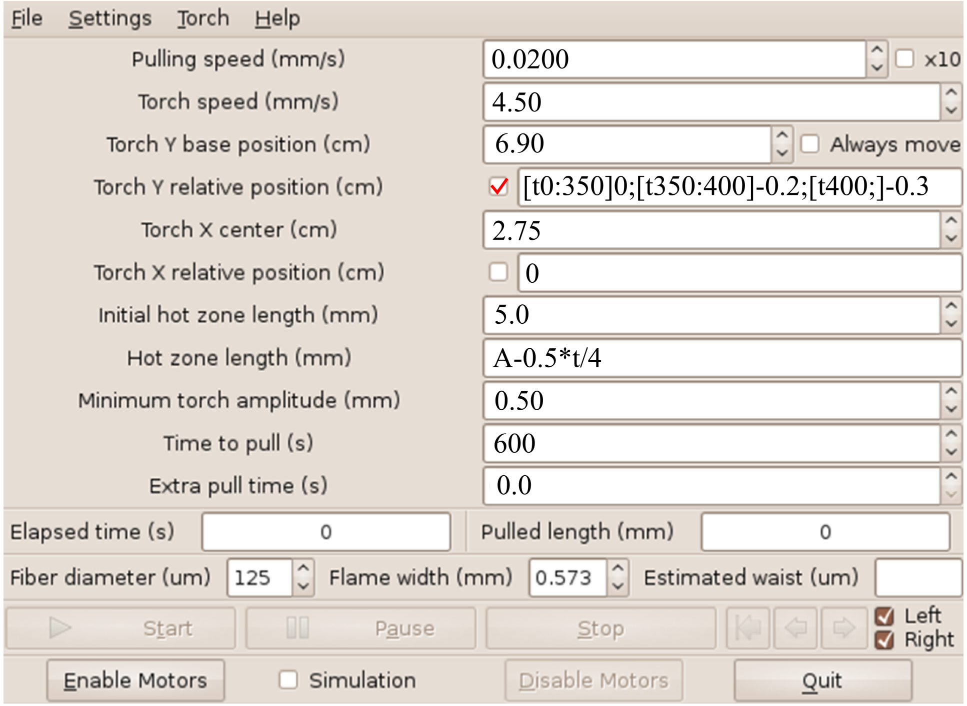

Pulling speed (mm/s)	0.0200 ☐ x10
Torch speed (mm/s)	4.50
Torch Y base position (cm)	6.90 ☐ Always move
Torch Y relative position (cm)	☑ [t0:350]0;[t350:400]-0.2;[t400;]-0.3
Torch X center (cm)	2.75
Torch X relative position (cm)	☐ 0
Initial hot zone length (mm)	5.0
Hot zone length (mm)	A-0.5*t/4
Minimum torch amplitude (mm)	0.50
Time to pull (s)	600
Extra pull time (s)	0.0

Elapsed time (s) 0 Pulled length (mm) 0

Fiber diameter (um) 125 Flame width (mm) 0.573 Estimated waist (um)

☑ Left ☑ Right ☐ Simulation

Figure 23. The software window used to control the fiber pulling. The parameters show recipe for making a single-mode-taper.

zone length" entry holds. Finally, "Time to pull" (in s) sets a time limit on the pulling process; this will stop the pulling motors and move the torch away from the fiber. "Extra pull time" (in s) specifies the time the pulling motors will continue pulling after the torch is retracted. After the pulling period, the torch is retracted away from the fiber.

Once the taper has the desired transmission properties, it must be removed from the tapering station, moved to the microscope, and interfaced to a microsphere. A special clamping system was built for holding the taper over the objective lens. Considerable care must be taken in transporting the taper from the tapering station to the microscope, as it is very fragile. The tunable laser must again be coupled into the taper, using fiber splicers. A beam splitter was used to pick off $\sim 10\%$ of the beam, which was sent to a wavemeter (Burleigh WA-100) in order to confirm proper calibration of the laser's wavelength reading (Figure 24). The remaining 90% of the beam was "inserted" into a single-mode fiber using a fiber-coupling apparatus (Thorlabs MBT610D), before which a half wave plate was used to control the polarization. One splicer was used to couple this fiber to the taper. A second splicer was used to link the other end of the taper that led to a photodiode for transmission measurements. This part of work is fairly painstaking, as it can be difficult to tell which of the two

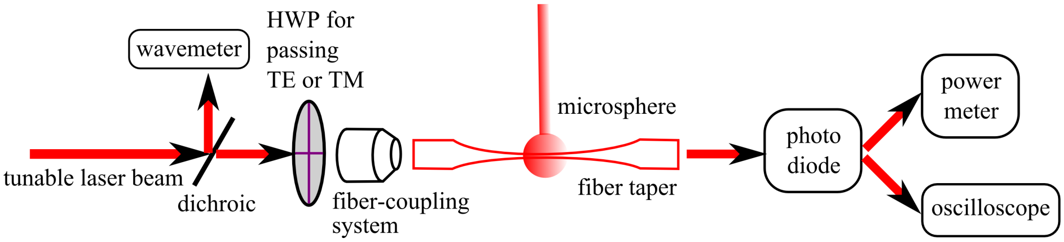

Figure 24. A drawing of the evanescent setup. The laser wavelength is swept across the desired range. A dichroic mirror reflects part of the laser light into the wavemeter. A half wave plate (HWP) is used to control the polarization. The microsphere is ~ 1 µm away from the taper. The transmission spectrum is collected by a photodiode whose signal is analyzed by a power meter or an oscilloscope.

splicers is misaligned if one does not see any transmission at the photodiode.

2.3.2 Evanescent measurements

Once the taper has been placed on the microscope stage, it must be brought into close proximity with the microsphere. The microsphere is attached to a moveable piezo stage (Thorlabs RB13MP) and placed above the taper. The laser is swept over a selected range of wavelengths (e.g., 765-781 nm) at a chosen speed while the transmission is measured with an oscilloscope or a powermeter. The sphere was then lowered down using the piezo stage, approaching the tapered fiber, until the WGM-dips appeared in the transmission spectrum. There are two basic modes of laser operation. In the “coarse” mode, the tuning mirror is moved by a DC motor-driven screw. In the “fine” mode, the mirror is moved by a piezoelectric transducer (PZT). In the latter case, the available wavelength range is quite narrow but the frequency sampling rate is larger. The laser used for most of the measurements in this work were the New Focus TLB-6700, which has a nominal bandwidth of $\leqslant 200$ kHz with a integration time over 50 ms.

2.3.3 Data analysis

The WGMs obtained from the evanescent measurement described above appear as dips in the transmission spectrum. In order to find the peak position and width (i.e., λ_0 and Q), the resulting dips were inverted and then fit to a Lorentzian waveform (Figure 25) given by:

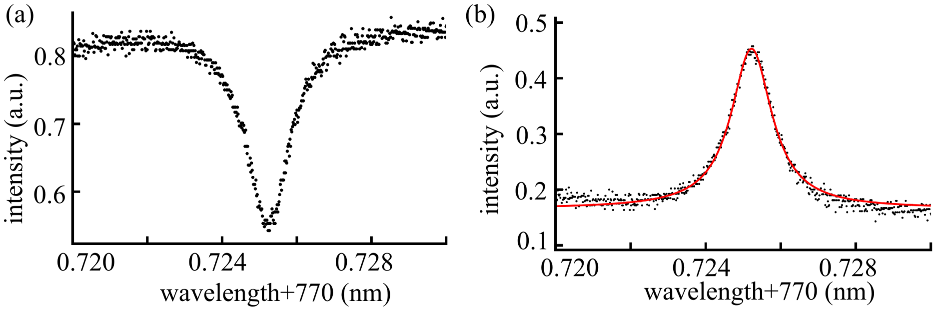

Figure 25. (a) An "evanescent" WGM (raw data). (b) The same data inverted, with a Lorentzian fit.

$$I(\lambda) = 2A \cdot \frac{1}{\pi \cdot \Delta\lambda_{FWHM} \cdot [1 + 4(\frac{\lambda - \lambda_0}{\Delta\lambda_{FWHM}})^2]} + DC, \tag{113}$$

where A is a scaling parameter, λ_0 is the central wavelength, $\Delta\lambda_{FWHM}$ is the full-width-at-half-maximum, and DC is the offset. One WGM in a "typical" transmission spectrum and the corresponding Lorentzian fit are shown in Figure 25. Here, the central wavelength λ_0 and the width $\Delta\lambda_{FWHM}$ obtained from the fitting were 770.725 nm and 1.33 pm, respectively (Figure 25(b)). Thus, the Q factor of this WGM is 5.8×10^5.

3. Structure of whispering gallery mode spectrum of microspheres coated with fluorescent silicon quantum dots

A slightly modified version of this chapter was published in the Journal of the Optical Society of America B 30(11), 3079-3085 (2013) by Y. Zhi, J. Valenta and A. Meldrum.

Abstract

Whispering gallery modes (WGMs) in microspheres containing embedded fluorophores (e.g., organic dyes or quantum dots) may find refractometric sensing or microlasing applications. However, there have been relatively few investigations on the relationship between the intrinsic microsphere resonances and the WGMs observed in fluorescence spectra for emitters coupled to the microsphere. Here we find that an apparently simple fluorescence WGM spectrum can mask a much more complicated underlying microcavity mode structure and that the observed fluorescence spectra are controlled by the emitter linewidth. By examining the cavity structure, we also verify that an effective ensemble emitter linewidth can be extracted from the fluorescence data. Finally, spectral diffusion is suggested as a possible origin of the periodic fluorescence WGM spectra observed in many microsphere cavities, without which these resonances might be unobservable.

3.1 Introduction

Optical microcavities provide a means to control the luminescence of semiconductor quantum dots (QDs). In the strong cavity-coupling regime, QDs may be used as photon sources for quantum computation experiments [142, 143, 144, 145]. However, strongly coupled systems in which single QDs interact with a microcavity are difficult to realize experimentally. In contrast, weak dissipative cavity coupling for ensembles of QDs is simple to achieve. In this regime, the spontaneous emission rates are modified by the optical density of states in the cavity. These system are currently being explored for the development of microlasers [15, 146, 147, 148], sensitive optical [149] and chemical microsensors [150, 151, 138, 19], and microfluidics [152, 132, 153]. Weakly coupled systems may even find specific applications in quantum logic [154]. Thus the basic physics of ensemble QD-cavity interactions in the weak-coupling regime is of fundamental and technical importance. Nevertheless, there are relatively few examples in which the fluorescence spectrum is clearly related to the intrinsic cavity modes. This relationship can lead to a better understanding of the fluorescence whispering gallery mode (WGM) structure, as well illustrated in one recent example [155].

Here we explore the interactions of an ensemble of silicon QDs (Si QDs) coupled to the WGMs of a microsphere cavity. The WGMs are characterized by a radial mode number, n, which defines the number of intensity maxima in the radial direction, and angular numbers l and m ($m = -l, -l+1, \ldots, +l$), which define the number of maxima in the azimuthal and polar directions. The initial motivation was provided by observations that the WGM quality (Q) factors ($Q\,\text{factor} = \lambda_{peak}/\Delta\lambda$, where λ_{peak} is central wavelength and $\Delta\lambda$ is spectral linewidth) observed in the fluorescence spectrum for modes with different l were apparently lower than the bare cavity Q factors, an observation that we [45] and others [156] previously attributed to the effect of the QD homogeneous linewidth. However, these recent efforts left open some important questions. First, the dot linewidth required to produce the observed fluorescence spectra was much narrower ($1-3$ meV) than the linewidths observed experimentally from single Si QDs at room temperature (~ 150 meV). This problem is similar to that initially reported in studies of dye-doped droplets, over 20 years ago [157]. Second, the fluorescence free spectral range (FSR) was orders of magnitude larger than the 30 GHz scan width of the tunable lasers used in previous experiments [53]. Thus the cavity modes observed via evanescent coupling could not be directly related to the resonances in the fluorescence spectrum.

The purpose of the present work is to achieve a better understanding of the fluorescence WGM structure, especially as it relates to the mode structure of the “cold” cavity. The effects of the intrinsic QD linewidth, the transfer function of the spectroscopy system, and intra-QD processes, such as spectral diffusion, tunneling, and resonance energy transfer can all contribute to the observed fluorescence WGMs.

3.2 Experimental

Microspheres were fabricated by melting the end of a fiber taper using a CO_2 laser. They were then coated with a layer of Si QDs embedded in a silicon oxide matrix, using previously described methods [158]. In short, the microspheres were dipped vertically into a solution of hydrogen silsesquioxide (HSQ) in a methyl isobutyl ketone solution. They were then dried in nitrogen and annealed at a temperature of 1100 ^{o}C for 1 hour in flowing N_2+4%H_2 gas to produce oxide film with embedded Si QDs.

Fluorescence spectroscopy was performed by pumping the QDs with an Ar^+ ion laser operated at a wavelength of 488 nm. The fluorescence was collected by a microscope objective and imaged onto the entrance slit of a spectrometer with a pitch of 0.066 nm/pixel (the Lhires from Shelyak Instruments). Fluorescence experiments were performed also at cryogenic temperatures using another micro-spectroscopy setup. For these measurements, the pump source was a 405 nm diode laser, which was coupled to an optical cryostat (Janis ST-500) and an imaging spectrometer (Acton SP-2300i) with a LN-cooled CCD camera.

Bare cavity transmission measurements were performed using the standard method by tapering an optical fiber and bringing the microsphere within the evanescent field of the taper. Light from a New Focus TLB-series tunable laser was injected into the taper, evanescently coupled to the microsphere, and the transmission intensity was measured using a photodiode. Part of the beam was picked off with a splitter and sent to a Burleigh 1000 wave meter. The laser can mechanically scan between 765 and 781 nm without mode hops, thus minimizing unpredictable wavelength jumps. A half-wave plate was used to control the polarization of the light in the fiber taper.

3.3 Results and analysis

A representative microsphere is shown in Figure 26. Its diameter is about 50 µm, and it exhibits the red fluorescence, which is typical of Si QDs. The PL intensity is somewhat nonuniform along the polar directions, possibly due to thickness variations caused by the vertical dipping during sample preparation. However, the intensity

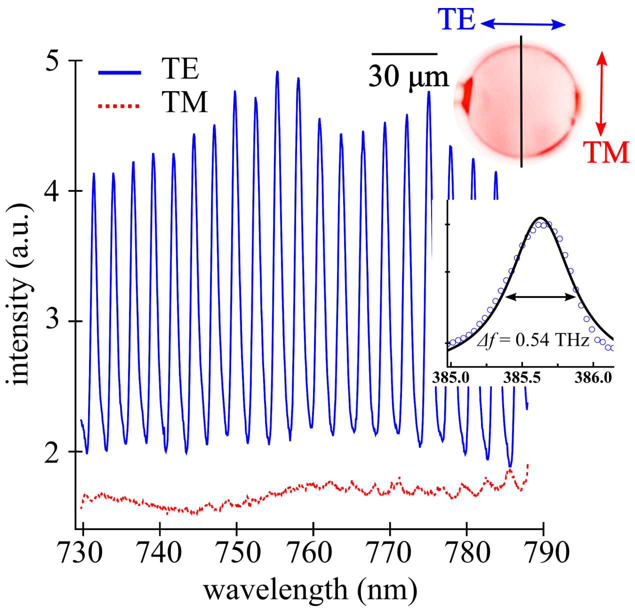

Figure 26. TE- and TM-polarized fluorescence spectra of the QD-coated microsphere. The upper inset shows a fluorescence image of the microsphere, with the orientation of TE and TM polarization directions shown. The vertical line indicates the entrance slit position of the spectrometer. The lower inset shows one mode cropped from the spectrum and the corresponding best-fit Lorentzian curve. The inset scale is converted to THz units.

around the equator is fairly constant, suggesting that the film is uniform in the regions used for data collection. The mode structure from fluorescence measurement in both TE and TM polarizations is also shown, where the TE/TM polarization corresponds to the electric field perpendicular/parallel to the WGM plane. The TE modes are characterized by Q factor of up to ~ 1000, a visibility of ~ 0.6, and a FSR of 2.87 nm, and a finesse of 7.4. The modes appear asymmetric (Figure 26 inset), with a slight skewing toward longer wavelengths. The TE polarized fluorescence WGMs appear much stronger than the TM ones, but this was mainly a result of a strong difference in the polarization efficiency of the optics in the microscope and spectrometer. By direct imaging on a different system, the two polarizations were found to have a roughly similar intensity. For TM modes, the Q factor, visibility, FSR, and finesse is ~ 840, 0.15, 3.06 nm, and 6.7, respectively. Normally, one might assume that these are first-radial-order $(n = 1)$ resonances and identify them by solving the characteristic equations [130, 131] for a coated sphere of the observed radius of ~ 25 µm. However, as we will show below, this may not represent an adequate mode identification.

The transmission WGM structure (from evanescent measurements on the same microsphere) depended on the distance between the fiber taper and the sample (Figure 27). When the sphere and the taper were well-separated (under-coupled), the Q factor for this mode was$\sim 6.0 \times 10^5$, as measured by fitting a Lorentzian curve to the data. As the sphere and the taper were brought closer together, the transmission minima first deepened and then became wider as the system transitioned to the overcoupled regime. Finally, when the taper and the sphere were in physical contact, the Q factor of the individual mode shown in Figure 27 decreased to $\sim 2 \times 10^5$, while the overall background transmission level also decreased strongly. Attractive forces caused the taper to suddenly "snap" into contact with the sphere when they were close together, which made it difficult to accurately determine the absolute distance between them. Therefore, Figure 27 uses a relative distance scale.

Figures 26 and 27 are consistent with previous results that appeared to show a considerable difference between the fluorescence and transmission mode structure [153, 159]. The mode shown in the transmission scan has a Q factor that is orders of magnitude greater than that observed in the fluorescence spectrum. However, the 30 GHz piezo-scan limitation restricts the number of observable cavity modes, making it difficult to unambiguously identify them or establish their relationship with the WGMs shown in Figure 26.

In order to establish the relationship between the cavity and fluorescence WGM spectra more clearly, a set of mechanical scans were taken in the range between 765 and 781 nm at a sampling rate of 0.2 pm per point. These spectra were acquired in the undercoupled regime, so as to minimize taper-induced losses from the cavity. A half-wave plate was used to control the polarization of the light entering the taper. Video images taken of light scattered from the taper and passed through an analyzer unambiguously determined the polarization (TE or TM) with respect to the plane of the microsphere's equator.

The transmission spectra indicated that the cavity mode structure is more complicated than would be expected on the basis of the fluorescence WGMs alone (Figure 28). In both polarizations, the spectra consisted of closely spaced families of modes. Individual WGMs within these families were separated by approximately 45 pm (see Figure 28(a2) and 28(b2)). The Q factors were estimated by performing Lorentzian fits and were found to be generally in the range of 10^5 for both sets of mode families. The maximum achievable Q factor is probably limited by surface roughness, as well as scattering and absorption in the QD film, since we have measured values approaching 10^9 in uncoated microspheres fabricated with the same method [159].

The observed modes were identified by first modeling the spectrum using the per-

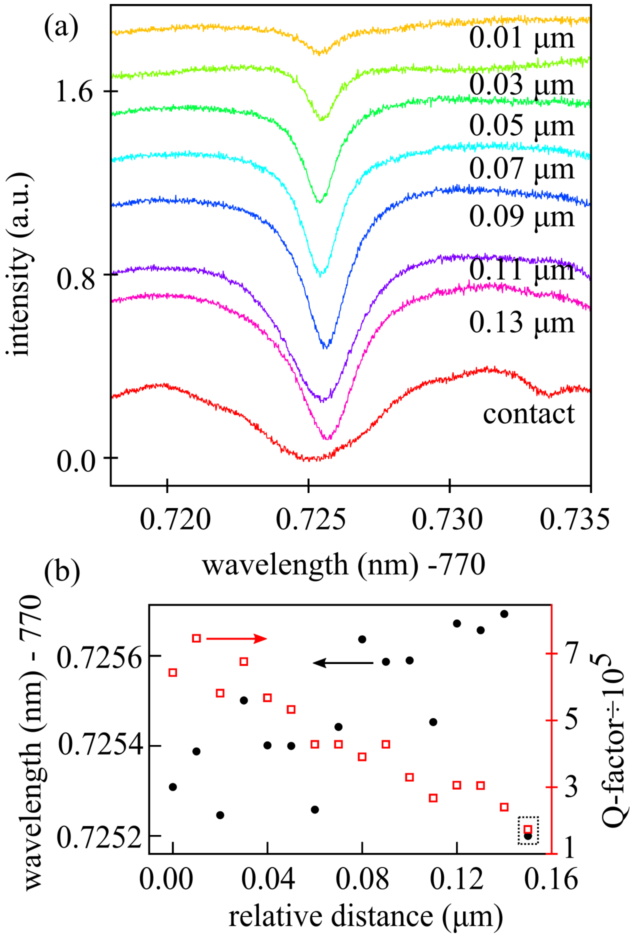

Figure 27. (a) Subset of transmission spectra taken as the distance between the taper and the microsphere was reduced. (b) The central wavelength (circles) and Q factor (squares) as a function of distance, as the taper approached the microsphere. The two points inside the dashed square indicate sphere-taper contact. Because the taper eventually snaps into contact with the microsphere, the horizontal axis indicates the distance moved relative to the location of the initial spectrum. Graphs (b) show the full data set; in (a) only a subset is shown for space reasons.

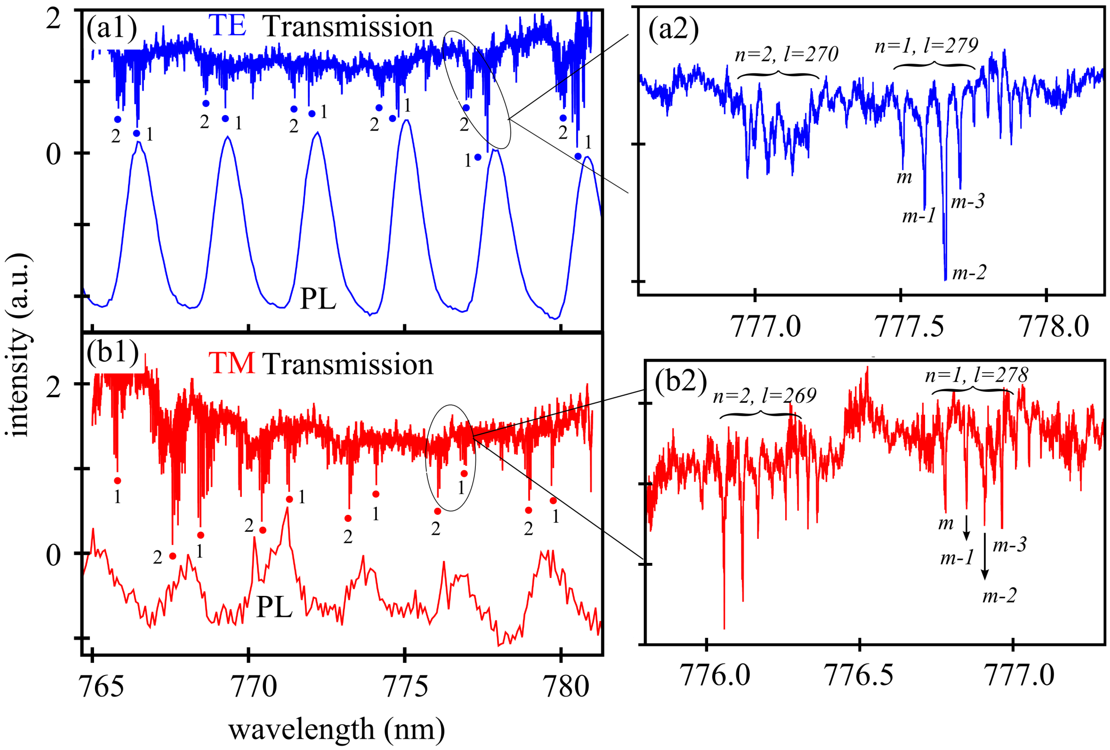

Figure 28. Transmission and photoluminescence (PL) spectra for the QD-coated microsphere. Both (a) TE and (b) TM polarizations are shown. The fluorescence WGMs correspond to groups of transmission modes. The slight wavelength mismatch may be due to the difference calibration procedures required to obtain the two types of spectra. The zoom-ins (a2) and (b2) show an expanded view of two of the transmission mode families.

turbation theory methods developed by Teraoka and Arnold [130, 131]. Accordingly, for the TE case

$$S_l(r) = \begin{cases} A_l\psi_l(n_1kr) & r < a-t \\ B_l\psi_l(n_2kr) + C_l\xi_l^{(1)}(n_2kr) & a-t < r < a\,. \\ D_l\xi_l^{(1)}(n_3kr) & r > a \end{cases} \tag{114}$$

In Equation (114), n_1, n_2 and n_3 are the refractive indices of the microsphere ($n_1 = 1.452$), the QD film ($n_2 = 1.670$), and outside air ($n_3 = 1.000$), respectively, and ψ_l and ξ_l^1 are the lth spherical Riccati-Bessel and Riccati-Hankel functions, and A_l, B_l, C_l and D_l are proportionality constants. $\psi_l(n_2kr)$ can be replaced by $\xi_l^2(n_2kr)$ to model the incoming wave in the middle layer, but it has a negligible effect on a structure of this size. The boundary conditions for TE polarization (the field amplitude and its derivatives must be continuous) lead to the solutions for the resonance wave vectors k. These are given by the roots of the expression [130]

$$\frac{n_3\xi_l'^{(1)}(n_3ka)}{n_2\xi_l^{(1)}(n_3ka)} = \frac{(B_l/C_l)\psi_l'(n_2ka) + \xi_l'^{(1)}(n_2ka)}{(B_l/C_l)\psi_l(n_2ka) + \xi_l^{(1)}(n_2ka)} \tag{115}$$

in which the primes indicate the derivative with respect to the argument, as usual. Here, the ratio of the pre-factors is given by

$$(B_l/C_l) = \frac{n_2\psi_l(n_1k(a-t))\xi_l'^{(1)}(n_2k(a-t)) - n_1\psi_l'(n_1k(a-t))\xi_l^{(1)}(n_2k(a-t))}{-n_2\psi_l(n_1k(a-t))\psi_l'(n_2k(a-t)) + n_1\psi_l'(n_1k(a-t))\psi_l(n_2k(a-t))}. \tag{116}$$

The solutions for Equation (115) were found using a numerical solver written in Mathematica [160]. Thus it is straightforward to find the mode Q-factors ($Q = Re[k]/2Im[k]$) associated with the radiation losses or with lossy materials. The TM case is mathematically very similar (with different boundary conditions) [131], so those equations will not be repeated here.

A good match to the data was found for a sphere radius of 24.7 µm and a film thickness of 50 nm. Considering only radiation losses, one would expect the highest Q factors to be associated with the first radial order ($n = 1$) modes, but the presence of a lossy surface layer can alter this relationship. Figures 29(a) and 29(b) show the electric field radial functions for the TE and TM polarized WGMs, respectively. In both cases, the main Q-limiting mechanism was found to be associated with the QD layer. For example, in the TE case (Figure 29(a)) both $n = 1$ and $n = 2$ radial mode

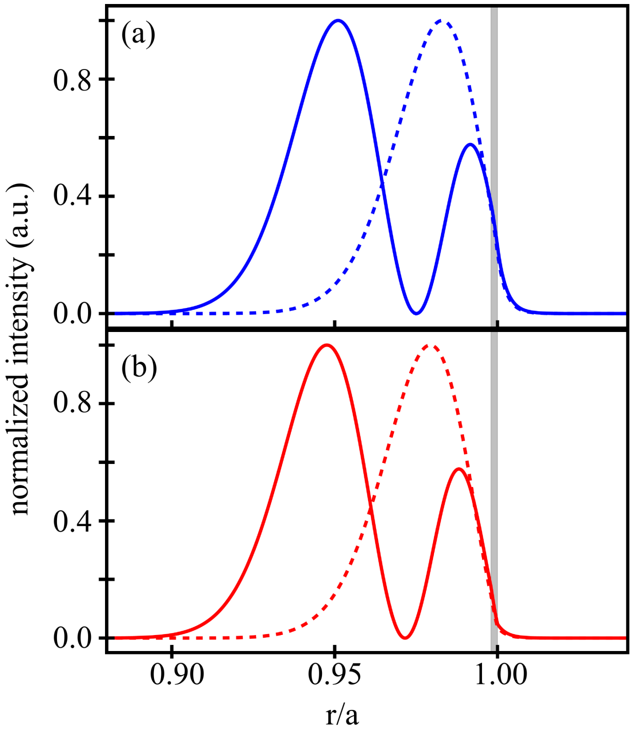

Figure 29. (a) Squared radial field functions of the first- and second-order radial TE modes with angular orders $l = 279$ and $l = 270$, respectively, where r and a on the horizontal axis represent the radial distance from the center of the sphere and the sphere's radius, respectively. Resonant wavelengths are 777.58 and 777.04 nm. (b) Intensity profiles of the first- and second-order radial TM modes with $l = 278$ and $l = 269$, respectively. Resonant wavelengths are 777.46 and 777.05 nm. In both (a) and (b), the dashed line represents the first-order-radial mode, and the solid line represents the second-order-radial mode. The QD film is represented by the vertical shades line.

fields overlap to a roughly similar extent with the QD layer, so the Q factors for both modes are similarly limited by absorption and scattering losses. They also both experience a similar surface-roughness-induced scattering. The theoretical results yielded Q factors close to 10^5 for the $n = 1$ and $n = 2$ WGMs, which is consistent with the observations in Figure 28. The modeling also gave a higher Q factor for the TM polarization, owing to a smaller overlap with the QD layer (Figure 29(b)), also in agreement with the results shown in Figure 28 (the experimental TM Q factors averaged about 1×10^5, compared to 6×10^4 for the TE case). The resonance shown in Figure 27 is likely a higher-radial-order TM mode, which for these conditions can have Q factors closer to 10^6.

Surface roughness also can affect the ultimate cavity Q factors achievable in these coated structures. While $Q = 10^6$ is an approximate upper limit in Si-QD-coated microspheres, in the uncoated case we have measured values of about 4×10^8. While atomic force microscopy (AFM) is rather difficult due to the fragility of these structures, Bianucci *et al.* [53] found an RMS roughness of 3.4 nm, using AFM on a flat QD film made by the same technique. This leads to a (very approximate) roughness limited Q factor of about 10^5 for a microsphere of this radius, according to the methods used in [58].

The splitting of these resonances into families of closely spaced modes is attributed to a very slight prolate distortion of the microsphere, which breaks the degeneracy of modes having a different number of polar maxima (i.e., modes with different values of m) [161]. An image analysis of the microsphere taken in transmitted light suggested a very slight prolate eccentricity of about 0.01. This is in agreement with previous work on uncoated microspheres fabricated using the same method [162, 17]. Given a mode degeneracy splitting of ~ 45 pm, the distortion amplitude can be estimated as [17] $e = l \cdot \Delta f / f = 0.016$, corresponding to an eccentricity of approximately 0.008, in reasonable agreement with observation.

The cavity mode structure was then compared to the fluorescence spectra (see Figure 28). While the scaling is imperfect due to the different wavelength calibrations used in each type of measurement, the fluorescence WGMs are mainly coincident with the groups of mode families observed in the transmission results for both polarizations. The fluorescence spectra therefore consist of a nearly equal mixture of both radial orders. Thus, the apparently single WGMs in the fluorescence spectrum correspond to multiplets of overlapping cavity modes with much higher Q factors. The asymmetry of the fluorescence WGMs, which hinders the Lorentzian line fitting (e.g., see Figure 26) could arise from the structure of the underlying families of cavity modes. The similarity of the Q factors for the first and second order modes is in contrast to previous experiments [153] in which the first-order modes dominated the fluorescence spectrum. However, the previous work used water as the external medium, in which case Equations (114-116) do predict that the first-order modes would have a much higher Q factor.

The results confirm that the fluorescence Q factors are lower than the cold cavity values in the same microsphere. In fact, much of the WGM substructure is totally washed out in the fluorescence spectra, leaving what appears to be only a single broad WGM at each apparent resonance. This effect could arise from two sources: (1) the transfer function of the spectrometer system may wash out the high-resolution mode structure (i.e., the fine structure really exists in the emitted fluorescence but cannot be resolved) or (2) the finite QD linewidth may lead to a spectrally broadened Purcell enhancement causing extensive mode overlap (i.e., the bare cavity mode structure is intrinsically washed out, due to the QD linewidth).

The first possibility was investigated by measuring the spectrometer transfer function using a spectral line from an HgAr calibration lamp. The transmission spectrum in Figure 28(a2) was then convolved with the transfer function to produce the resulting simulated fluorescence spectrum (Figure 30). While the fine mode structure is indeed washed out, the result does not resemble the real fluorescence WGM data. The first- and second-order mode families appear as a broad but clear doublet, which is not observed in the fluorescence spectrum. In contrast, convolving a 1.6 meV QD linewidth (i.e., the calculated linewidth based on [45], as discussed further below) causes the entire set of cavity modes around 777 nm to appear as a single peak, similar to the actual fluorescence spectrum. Thus one can conclude that the fluorescence WGM linewidth is not limited by the spectrometer transfer function, but is indeed due to the QD-cavity coupling.

The QD linewidth required to produce fluorescence WGMs with $Q = 1000 - 3000$ can be estimated [45] as $\Delta\lambda_{QD} \approx \lambda_{peak}/Q + \Delta\lambda_{cavity} \approx 260 - 780$ pm or approximately $0.5 - 2$ meV ($\Delta\lambda$ indicates the spectral linewidth of the QD or the cavity, as indicated by the subscript). However, this estimated linewidth is much narrower than the reported room-temperature linewidth of single Si QDs, which is in the range of 150 meV [163, 164, 165]. Indeed, for such a large QD linewidth, which is comparable to or greater than the FSR, no modes should be visible in the fluorescence spectra at all.

One possible explanation for this apparent inconsistency is related to spectral diffusion (SD) in the QDs. SD causes the relatively narrow homogeneous linewidth of a single particle to randomly jump or diffuse about a distribution of emission energies, making the time-averaged linewidth appear broad. Spectral diffusion has been well studied in direct-gap QDs [166] and is attributed to a crystal-field distortion arising from charge trapping within excited particles [167]. At low temperature, the time scale for the SD process can be on the order of milliseconds or even seconds in capped QDs [168], although it can be faster depending on the surface conditions [169]. The SD rate increases at elevated temperature, owing partly to thermally activated escape from local trap sites [166]. Thus many studies focus on spectral diffusion at low temperature in order to avoid thermal effects, which tend to dominate at temperatures above 50 K, at least in CdSe QDs [170]. There is one previous report of SD in Si QDs, in which the single-particle linewidth narrowed from 150 to 105

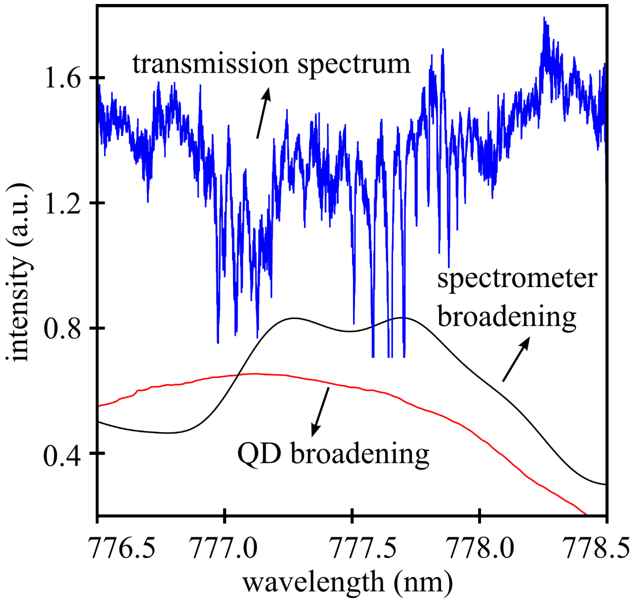

Figure 30. TE transmission spectrum (blue line), shown along with its convolution with the spectrometer transfer function (black line) or with a QD linewidth of 1.6 meV (red line). The results were inverted to simulate a fluorescence spectrum. The spectrometer transfer function results in a broad, double-peaked mode, while a QD linewidth convolved with the transmission spectrum would result in a single, slightly asymmetric fluorescence maximum, similar to the experimental observation.

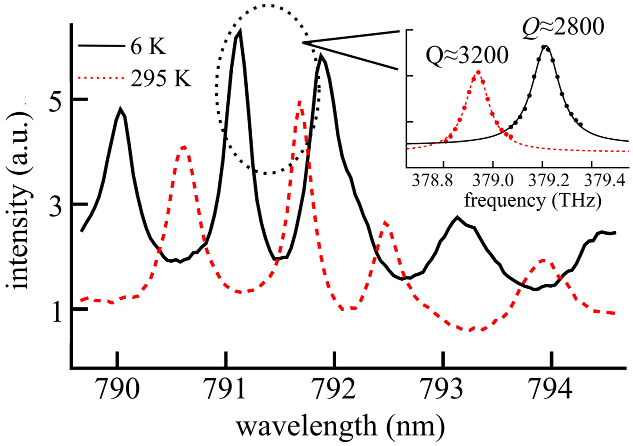

Figure 31. PL spectra of a QD-coated microsphere at 6 K (solid line) and 295 K (dashed line), respectively. The inset shows the Lorentzian fitting of one mode.

meV when the collection time was shortened by a factor of 100, at room temperature. [165]. More recent reports have shown that individual luminescence spectra of Si-QDs can jump over a range of about 100 meV [171, 172]. Thus spectral diffusion could play an important role in the observed fluorescence WGM spectra.

In order to investigate an SD-related explanation for the WGM spectra reported here, a QD-coated microsphere was cooled to 6 K (this was a different microsphere than the one shown above). At low temperature, the line-broadening effects of SD should be minimized. Figure 31 illustrates how the fluorescence spectra changed as a function of temperature in these experiments. First, the WGMs red-shifted as the temperature increased from 6 to 295 K. This effect has been observed before in glass microcavities and is attributed mainly to the positive thermal-optic and thermal expansion coefficients of silica [173, 67]. More interestingly from the point of view of the spectral diffusion hypothesis, the fluorescence Q factor *increased* from ~ 2800 to ~ 3200 on heating from 6 K up to room temperature while the mode visibility (essentially derived from the peak-to-background ratio) also slightly increased.

A higher Q factor at elevated temperatures seems surprising, but it can be explained on the basis of spectral diffusion. At low temperatures, SD is minimized and, in an extreme limiting case, the QD homogeneous emission would be frozen in. Under these conditions, the model [45] developed previously would apply, and a homogeneous QD linewidth about 0.5 meV would be needed to produce the observed low-temperature spectrum, which agrees reasonably well with single-particle spectroscopy results at low temperature [164]. As the temperature is increased, SD processes would become faster and extend over a broader energy range [174]. As previously suggested for dye droplets [175], random spectral diffusion could increase the on-resonance emission probability, since a normally “off resonance” emitter can undergo spectral diffusion toward a resonance, where the emission rate is faster. This changes the smooth probability distribution for emitted photons from the whole QD ensemble, instead giving a rippled distribution in which emission is more likely to occur on a cavity resonance than it would be in the absence of SD.

The possible effect of SD on the cavity luminescence can be illustrated with a simple back-of-the-envelope approximation. In Ref. [45], the ensemble PL spectrum was calculated as a smooth probability function representing an inhomogeneously broadened distribution of emitting particles, which was then perturbed by the cavity resonances. SD would alter the probability function by concentrating it more on resonance. In other words, a given QD is more likely to emit on resonance in the presence of SD than it would otherwise.

By using the model developed in [45] but altering the emission probability toward a cavity resonance, one finds a decrease in the intensity emitted far from the resonance and an apparent sharpening of the mode structure (Figure 32). In the extreme limit, all of the particles would spectrally diffuse to the cavity resonance before they emit, resulting in an effectively single-particle emission spectrum. While one cannot determine how the emission probability distribution really looks from the experimental data, the effect of concentrating the distribution toward the cavity resonances clearly increases the apparent fluorescence Q factor and the mode visibility.

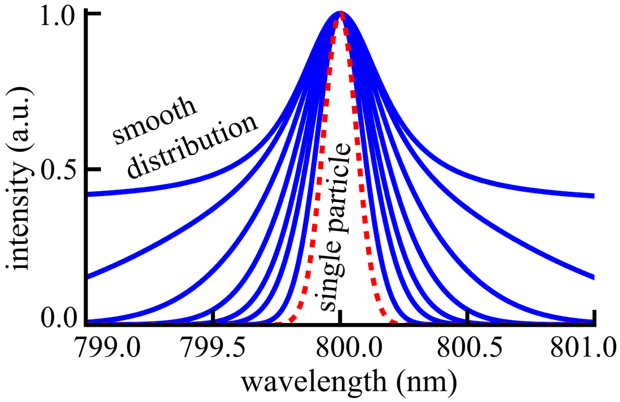

Figure 32. Simulated fluorescence spectrum from a single cavity mode with $Q = 5 \times 10^5$ centered at 800 nm, for a QD linewidth of 0.8 meV. The peak becomes narrower as a greater fraction of the QDs emit closer to the cavity resonance. The spectrum would eventually become equivalent to that for a single particle centered on resonance (dashed red line). The Q factor in that case is close to the estimated value for a single particle, given by $Q = \lambda_{peak}/(\Delta\lambda_{QD} - \Delta\lambda_{cavity})$.

The implications of SD can likely be extended to numerous QD-cavity systems operating at room temperature. For many different kinds of particles, ranging from Si [165] to InGaAs [176], to CdSe [166], the time-averaged single-particle linewidths at room temperature are much too wide to permit the existence of cavity modes in the ensemble fluorescence spectrum, despite the fact that the cavity resonances are almost always observable. Although the effects of SD in fluorescent microcavities were originally suggested many years ago [175] and are probably ubiquitous in these cavity-coupled systems, SD has not been much considered in terms of the basic physics of ensemble QD-cavity interactions in the weak coupling regime. In fact, it seems that without SD, many QD-cavity systems might not show fluorescence WGMs at room temperature at all.

These results have some implications for the development of light emitters and sensors based on Si-QD-coated microcavities. We did not find clear evidence for stimulated emission or lasing under any of the conditions investigated (e.g., no line narrowing or sudden increase in output intensity of certain modes as a function of pump power) up to about 200 mW laser power focused in free-space to the best of our ability onto the microsphere. Since we do not know the laser spot size at the microsphere location, it is difficult to estimate the power density exactly. A previous study using pulsed excitation did report evidence in favor of room-temperature ASE (amplified spontaneous emission) from a microsphere in which Si-QDs were deposited via a PECVD process [177]. While we cannot rule out the possibility of short time-scale stimulated emission from these observations, as also reported in flat films [178], we find that it probably does not occur in these samples under the strongest CW excitation we could reasonably achieve, with cavity Q factors in the range of 10^5. These results also have potential implications in terms of the fluorescence WGM response in sensor-type devices as well, since the ultimate refractometric sensitivity may arise from the combined resonance shift of many underlying cavity modes.

3.4 Conclusions

This work investigated the whispering gallery mode spectrum of a quantum-dot coated microsphere. The bare cavity spectrum was found to have a much more complex structure than the relatively simple fluorescence spectrum. While we have previously attributed similar fluorescence WGM spectra to the first-order radial modes of the cavity, we find that the actual cavity structure consists of families of much high Q resonances. Individual WGMs are split into overlapping groups of resonances due to the slight distortion of the microsphere. The assortment of modes is convolved into the broad resonances observed in the fluorescence spectrum, mainly as a result of the QD linewidth. At room temperature, the linewidth has to be less than 2 meV to produce the observed fluorescence WGM spectrum, for these Si QDs.

We also investigated the WGM structure at low temperature. At 6 K, the fluorescence WGM Q factors are slightly lower than they are at room temperature. This result is consistent with the possibility of spectral diffusion in the silicon QDs, or any other thermal process, which increases the on-resonance emission probability. SD would also explain why it is possible to observe modes at all, when the apparent single-dot linewidths are evidently so wide that they would otherwise have to completely wash out the WGM resonance structure.

These observations are probably applicable to many fluorescent microsphere structures in which the apparently simple fluorescence WGM structure masks a more complicated underlying cavity mode structure. Additionally, spectral diffusion (or a similar process) probably plays an important role in many emitter-cavity systems, since it can reconcile the apparently wide linewidth with the existence of WGMs in the emission spectra.

3.5 Acknowledegments

The authors thank NSERC and AITF iCiNano for funding, and and the Veinot Lab at the University of Alberta for providing some of the materials used in the coated microsphere synthesis. The work of one author (J. V.) was partially supported by the EU-project NASCEnT (FP7-245977). Y. Z. acknowledges partial support from the China Scholarship Council.

4. Tuning a microsphere whispering-gallery-mode sensor for extreme thermal stability

A slightly modified version of this chapter was published in Applied Physics Letters 105, 031902 (2014) by Y. Zhi and A. Meldrum.

Abstract

The reactive sensing application of optical microspheres can be plagued by local temperature fluctuations. Fluctuations due to laser heating or ambient changes in the lab environment cause resonance shifts that appear as noise or an underlying drift in the sensor data. Here, we show that thermal fluctuations can be exactly compensated in virtually any local medium (i.e., “analyte”) by the application of a high-index coating on the surface of the microsphere. The coating precisely controls the extent of the field penetration into the surroundings in such a way that the thermal shifts associated with the three layers (the glass sphere, the coating, and the exterior medium) can be exactly balanced. The conditions required for thermal stability were investigated theoretically; on the basis of these calculations a real sphere was then synthesized that showed excellent stability for aqueous solutions.

Optical microspheres can be used to measure minute changes in the properties of the surrounding medium. If the refractive index of the sphere (typically composed of silica or polystyrene) is higher than that of the surroundings, radiation can be trapped inside the sphere by total internal reflection as it propagates around the circumference. This leads to the development of resonances known as "whispering gallery modes" or WGMs, which in microspheres typically have a quality (Q) factor in the range of 10^5 to 10^9. Part of the electric field of each mode extends outside of the sphere, thus sampling the external medium.

The WGMs can provide a sensitive transduction mechanism for a variety of different sensing applications. The resonant frequency is sensitive to (i) pressure [179] and force [180] (via pressure-induced stress and strain in the sphere material); (ii) the complex refractive index of the surrounding medium [21, 181, 182]; and (iii) the ambient temperature (via thermo-optic and thermal expansion effects) [183, 184, 140, 185, 186]. The second application is particularly attractive because of the extremely small effects that can be detected in a microfluidic environment. In all three, changes in the local index of either the medium or the sphere itself (due to changing pressure, temperature, or composition) are transduced via resonance wavelength shifts. This is sometimes referred to as the "reactive" sensing mechanism [187].

Some of the most sensitive experiments are able to detect single viruses [188], proteins [24], or other biomolecules when they bind to the surface of a microsphere. These experiments typically use a tapered fiber or waveguide to evanescently couple to the WGMs, and a tunable laser to sweep through the mode. While incredibly sensitive, the sensors are fragile and can be difficult to incorporate into a robust transduction device. Fluorescent-type microspheres have also been widely investigated for refractometric sensing applications. These devices require a spectrometer to measure the emission from dye-doped [138, 189, 190, 191, 192] or quantum dot-doped microspheres [139, 193, 18, 153] immersed in the analyte.

Regardless of the measurement method, thermal fluctuations can ultimately limit the ability to detect refractometric changes in the surrounding. For "reactive" sensing, one therefore desires the microcavity to be insensitive to temperature. The same is true for other WGM-type cavity structures such as cylindrical capillaries, for which the thermal shifts have been calculated [173, 194]. While microspheres have been proposed as thermal sensors [183, 184, 140, 185, 186, 195, 41] (in which, contrary to the case for refractometric sensors, one *wants* a large thermal response), the detection limit optimization for refractometric sensing with a microsphere has not been widely investigated until quite recently [196] despite the fact that thermo-optic fluctuations can be a dominant noise source in microsphere resonators [197]. While thermal perturbations induced by variations in the optical pump power can be "self-compensated" under certain conditions [198, 199], an external "laboratory" temperature drift cannot be compensated via optical coupling [198].

The presence of a high-index coating on the surface of a microsphere can have strong effects on the refractometric sensitivity (S) [130, 131] and will affect the thermal sensitivity ($S_{thermal}$) as well. Both sensitivities are controlled by the overall profile of the electric field, while the $S_{thermal}$ is also determined by the thermo-optic and thermal expansion properties of the different layers. Here, we will show theoretically and demonstrate experimentally that a high-index coating can be tailored to provide thermal stability for virtually any exterior medium. Unlike a recent interesting example for a microdisk resonator [200], here we do not require a negative thermo-refractive coating - instead, the positive coating serves both as a fluorescent layer and a means to "lure" the mode field energy into the surrounding fluid. The work also draws on ideas for passive temperature stabilization of one-dimensional photonic cavities [201], in which altering positive and negative thermo-refractive layers could, in theory, completely cancel the thermal response of the structure [201]. Alternative methods such as self-referencing, using oppositely polarized modes in a birefringent cavity, have also been investigated [202].

The thermal sensitivity of a coated microsphere can be calculated based on the fraction of the WGM mode energy in each layer. Starting from the simple relation in which the fractional wavelength shift $d\lambda/\lambda_0$ is proportional to the fractional change in the effective refractive index (m_{eff}) and radius a (i.e., $d\lambda/\lambda_0 = dm_{eff}/m_{eff} + da/a$), one obtains [173]:

$$\begin{aligned} S_{therm} = \frac{d\lambda}{dT} &= \lambda_0(\frac{dm_{eff}}{m_{eff}} + \frac{da}{a})\frac{1}{dT} = \lambda_0(\frac{1}{m_{eff}}\frac{dm_{eff}}{dT} + \frac{1}{a}\frac{da}{dT}) \\ &= \lambda_0(\frac{f_1\kappa_1 + f_2\kappa_2 + f_3\kappa_3}{f_1m_1 + f_2m_2 + f_3m_3} + \alpha_1) \end{aligned}, \quad (117)$$

where m_{eff} can be approximated as $f_1m_1 + f_2m_2 + f_3m_3$, in which f_i corresponds to the energy fraction in the i^{th} layer, $\lambda_0 = 2\pi$ is the resonance wavelength, and the thermo-optic coefficient is $\kappa_i = dm_i/dT$. The subscript refer to the layer number: layer 1→glass microsphere; layer 2→high-index coating; layer 3→external medium.

For reactive sensing applications one wants S_{therm} to be as close as possible to zero. This can, in principle, be achieved if the thermo-optic coefficient of layer 3 (the surrounding medium) is negative, as is the case for many common solvents. If κ_3 is negative, it can potentially balance the positive coefficients of the glass and the quantum dot (QD) coating [173]. Particularly desirable would be a zero thermal sensitivity for water, which is the most common solvent for biosensing applications.

The energy fractions in each layer depend on the polarization:

$$f_{i,TM} = \frac{I_i}{I_1 + I_2 + I_3}, \tag{118a}$$

$$f_{i,TE} = \frac{m_i^2 I_i}{m_1^2 I_1 + m_2^2 I_2 + m_3^2 I_3}, \tag{118b}$$

where I_1, I_2 and I_3 represent the volume-integrated electric field radial functions in each layer:

$$I_1 = \int_0^b A_L^2 [\psi_L(m_1 k_0 r)]^2 dr, \tag{119a}$$

$$I_2 = \int_b^a [B_L \varsigma_L(m_2 k_0 r) + \xi_L(m_L k_0 r)]^2 dr, \tag{119b}$$

$$I_3 = \int_a^\infty D_L^2 [\xi_L(m_3 k_0 r)]^2 dr. \tag{119c}$$

Here, A_L, B_L and D_L, are proportionality factors, and ψ, ξ, and ς refer to the Riccati-Bessel, Riccati-Hankel (type 1), and Riccati-Hankel (type 2) functions of order L. The thickness of the layer is $t = a - b$, where b is the radius of the bare microsphere and a is the radius including the coating.

We follow the methods derived in Refs. [130] and [131] to solve for k_0, S, and the various coefficients for both the TE and TM polarizations. This is done by establishing the appropriate boundary conditions for each polarizations, and using a numerical root solver on the system of spherical equations that describe the radial field functions in each layer. These calculations also provide the electric field radial profile for any desired mode.

Finally, the reactive detection limit due to thermal fluctuations is given by

$$DL_{thermal(TE,TM)} = \frac{d\lambda_{(TE,TM)}}{dT} \cdot \frac{dT}{S_{TE,TM}}. \tag{120}$$

This gives the detection limit for refractometric sensing as imposed by thermal fluctuations only. The term dT/S is the ratio of the thermal fluctuations in the experiment to the refractometric sensitivity. One wants $DL_{thermal}$ as close as possible to zero, or at least to be well below the detection limit imposed by the (noise-limited) wavelength shift resolution of the measurement system ($DL_{sensing} = R/S$, where R is the shift resolution and S is the refractometric sensitivity of the structure).

To estimate the thermal sensitivity and DL of a layered microsphere, we model a microsphere of radius $a = 30$ µm immersed in water. The coating consists of a layer of silicon QDs, which can be easily deposited on a glass microsphere and has a refractive index high enough to strongly modify the electric field profiles [153]. The refractive indices and thermo-optic coefficients used were $m_1 = 1.45$, $\kappa_1 = 11.9 \times 10^{-6}$ K^{-1}, $\alpha_1 = 0.55 \times 10^{-6}$ K^{-1} (silica); $m_2 = 1.67$ [132], $\kappa_2 = 1.0 \times 10^{-5}$ K^{-1} (silicon QDs); $m_3 = 1.33$, $\kappa_3 = -0.8 \times 10^{-4}$ K^{-1}(water). The value κ_2 for the silicon quantum dot layer [203] was taken for a Si-QD film composition that should be similar to the one employed in the experiments [135]. We then solved for the first-order radial modes with angular mode orders having wavelengths near 750 nm.

By solving Equation (117) over a range of QD coating thickness and angular mode order, one can effectively plot a thermal sensitivity "map" for a given microsphere (Figure 33). There is an optimal coating thickness near 80 nm at which the thermal sensitivity is zero for TE modes (dashed line in Figure 33(a)). The thermal sensitivity is also small for the TM-polarized WGMs, eventually reaching zero at a slightly greater film thickness near 140 nm. This result implies that it should be relatively easy to achieve a zero thermal shift for a coated sphere immersed in water simply by controlling the layer thickness, while avoiding the exceptional fragility of thin-walled capillary structures. For a microsphere, the coating thickness needed to cancel the effect of thermal fluctuations appears easily achievable for virtually any radial order, including the first-order modes that naturally dominate the fluorescence spectrum.

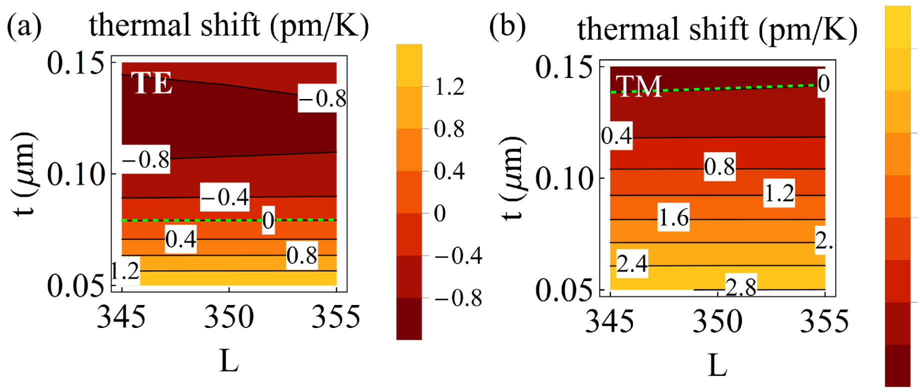

Figure 33. Calculated thermal shift (in pm/K) for a 30-µm-radius microsphere coated with a Si-QD film of thickness t, for the first-radial-order whispering gallery modes with angular orders from 345 to 355 (wavelength range from $\sim$ 750 to $\sim$ 790 nm. Both the (a) TE and (b) TM polarization are shown.

The effect of different solvents on the thermal sensitivity of a microsphere sensor can be visualized by constructing thermal shift maps for a single value of L and t, as functions of κ_3 and m_3. An example is shown in Figure 34, which covers a range of refractive indices from $m_3 = 1.30$ to 1.36 and κ_3 from 0 to -4.5×10^{-4}, for both polarizations (again, for a 30-µm-radius glass sphere with a $t = 80$ nm coating and $L = 350$). These values cover a wide range of common solvents for refractometric or biosensing experiments. For this thickness, the thermal sensitivity for water is zero for the TE polarization, but for other external media the thermal shift can be either positive or negative (e.g., it is negative for ethanol owing mainly to its high refractive index, but would be positive for air). The effects of thermal fluctuations can, in principle, be tuned to zero for any desired external medium, by controlling the layer thickness.

The detection limit imposed by thermal fluctuations can also be mapped, by converting directly from the thermal sensitivity in Figure 34(a1) and (b1) to a detection limit via Equation (120) (Figure 34(a2) and (b2)). The detection limit "maps" illustrate the result for a local temperature fluctuation of 1 K. A "valley" develops where the thermal contribution to the refractometric detection limit is small or even approaches zero. For this particular QD film thickness, water falls precisely within this valley, while solvents such as ethanol and methanol (plotted as dots in Figure 34) cause significant thermal shifts that contribute to the overall detection limit.

Guided by the theory above, we attempted to build a thermally stable (for water) microsphere by melting the end of a tapered fiber, using a CO_2 laser. The microsphere was then dipped into a solution of hydrogen silsesquioxane (HSQ) in a methyl isobutyl ketone solution. The microsphere (which is still attached to the taper) was then annealed at 1100 °C for one hour in flowing N_2+5%H_2 forming gas. This process evaporates the solvent and collapses the HSQ (nominally $Si_8O_{12}H_8$) molecular structure, forming a layer of silicon QDs encapsulated in a silica matrix [133]. The film thickness can be controlled by changing the HSQ concentration in the solvent and by employing a multiple-dip procedure. Films with a thickness on the order of 10^2 nm (close to the "zero valley") can be made with a single-dip fabrication process in a mixture of $\sim$ 15% to 35% HSQ concentration in weight [153].

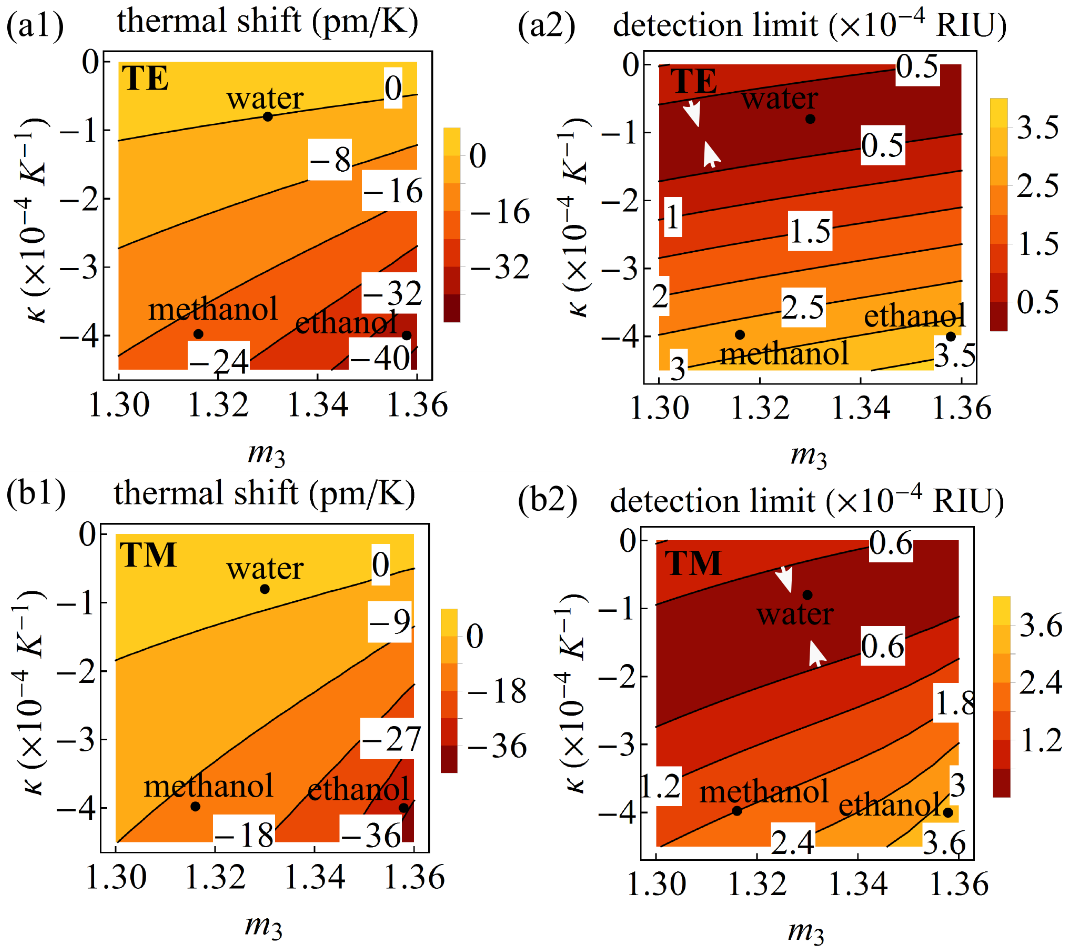

Figure 34. (a1) and (b1): Contour plots showing the thermal sensitivity as a function of the thermo-optic coefficient and refractive index of the surrounding medium, for the (TE) (top) and TM (bottom) polarizations, respectively. Panels (a2) and (b2) show the detection limits calculated using Equation (120), assuming a 1 K fluctuation. Again, we observe that for these conditions, "water" falls into a valley of low detection limits, as indicated by the white arrow.

The resulting microsphere had a nominal radius of 32 µm and was characterized by a bright red fluorescence and a clear WGM resonance structure in the emission spectrum (Figure 35). We have previously characterized the mode structure from similar spheres quite extensively [204]; these modes are the first-radial-order WGMs with the angular order L ranging from ∼ 330-410. The microsphere was then inserted into a square capillary with an inner side length of 700 µm and various fluids were pumped in using a syringe pump. The sensitivity was found to be 87 and 70 nm/RIU for the TE and TM modes, respectively, obtained by linear fitting to the WGM shifts as the solvent was changed from methanol, to water, to ethanol.

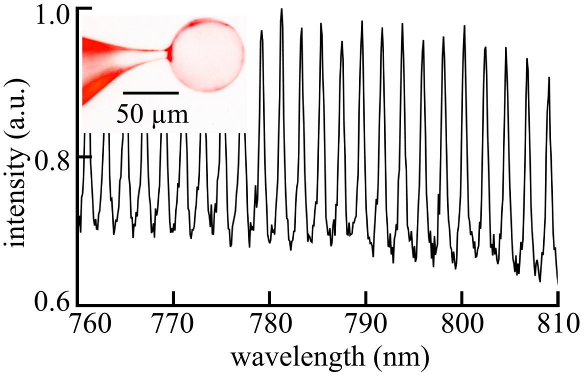

Figure 35. Fluorescence spectrum of the Si-QD-coated microsphere. The inset is a fluorescence image (with the black background converted to a white one) from which one can estimate a microsphere diameter of ∼ 64 µm.

For thermal shift measurement, once the sphere was completely immersed the pumping was stopped. A small resistive heater and thermocouple were placed within ∼ 1 mm of the capillary surface. The microsphere fluorescence spectrum was excited with a 442 nm HeCd laser and was measured as the temperature was ramped at 0.3 °C/min from 25 to 40 °C. The laser was kept at a relatively low power in order to minimize secondary heating effects. The experiments were repeated with air, water, methanol, and ethanol in the capillary channel. The wavelength shift was measured using the Fourier shift theorem [141] to extract the average WGM shift over the whole spectrum.

The observed shifts were -8.5 ± 0.3, and -14.7 ± 0.2 pm/K for methanol and ethanol, respectively (TE modes); whereas for air the shift was $+3.5 \pm 0.2$ pm/K (Figure 36(a)). For TM modes, the shift were -6.3 ± 0.2 pm/K, -11.0 ± 0.3, and $+2.7 \pm 0.1$ pm/K for methanol, ethanol and air, respectively (Figure 36(b)). The sign of the shifts is in agreement with the theory, but their magnitude is only about half of the value predicted by Equation (117) (for reasons discussed below). As predicted by theory, for the case of water the wavelength shifts were almost independent of temperature, with a thermal sensitivity of only $+0.6 \pm 0.3$ pm/K and -0.3 ± 0.1 pm/K for TE and TM modes, respectively. These shifts correspond to a detection limit of $(7.3 \pm 4.2) \times 10^{-6}$ RIU (TE) and $(4.9 \pm 3.6) \times 10^{-6}$ RIU (TM) assuming a temperature fluctuation of 1 K. Thus, a controllable high-index coating can be employed to fine-tune a microsphere for exceptional thermal stability, even down to virtually zero, for the most common bio-solvent (water).

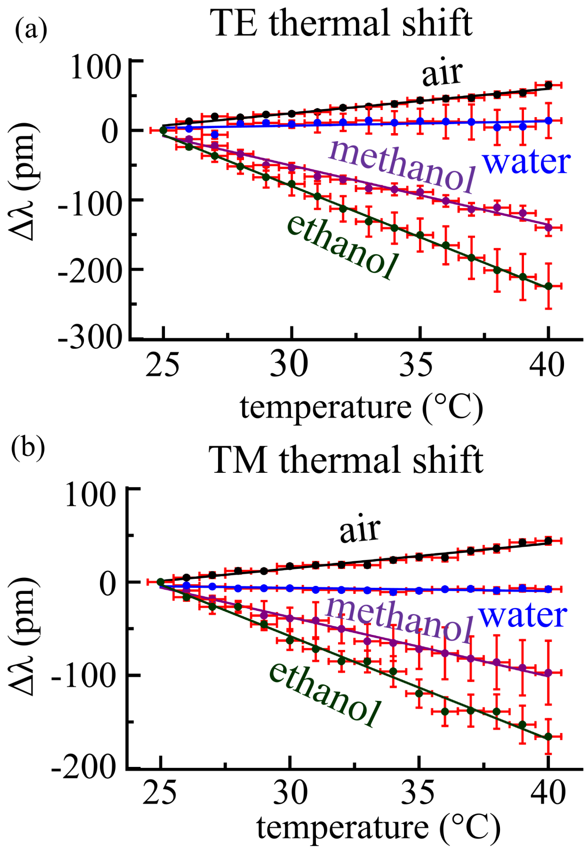

Figure 36. WGM shifts as a function of temperature for air, water, methanol, or ethanol as the external medium. Linear fitting was used to obtain the thermal sensitivity in each case. The shift errors were obtained from the Fourier analysis [141] used to obtain the wavelength shifts, and the temperature errors were based on the observed variations in the thermocouple reading over the course of the measurements.

For the case of a water solvent, the results agree closely (but not exactly) with the theoretical calculations shown above. The reasons for the discrepancy are that the synthesized microsphere is slightly larger than 30 µm, and the film thickness, while likely close to 80 nm [153], cannot be determined precisely. As well, the Fourier method averages the shift over the whole spectrum, and dispersion was not considered in the calculations. Despite these approximations, the results agree reasonably well with the theoretical ones, showing a nearly-perfect thermal stability for a water solvent.

The reason that the measured thermal shifts for ethanol, methanol, and air were smaller than the theoretical values is probably due to the delay in heating the microsphere to the temperature indicated by the thermocouple. Since the microsphere was inserted within a glass capillary, it was effectively shielded from the heating element and would be slow to achieve the ambient temperature. To evaluate this hypothesis, an additional experiment was conducted in which the microsphere was held directly beside the heater without being inserted into a capillary. The thermal sensitivity was found to be $+8.2 \pm 0.1$ pm for TE polarization (measured in air), which is much closer to the theoretical values. This is consistent with the idea that the shifts measured in Figure (36) are smaller than they "should" be as a result of thermal shielding of the microsphere inside the capillary.

To conclude, we showed that a coated microsphere can be designed to have WGMs that are almost perfectly insensitive to thermal fluctuations for virtually any specific local medium. We then synthesized a microsphere that approximated the ideal condition for a water solvent (the most important solvent for biosensing applications) and measured the thermal shift. For water, the temperature-induced shifts were indeed very close to zero, indicating that microsphere WGM-based sensors can be constructed to be insensitive to local temperature fluctuations. In this device, the positive thermo-optic coefficients of the glass sphere and the coating layer almost exactly balanced the negative thermo-optic coefficient of the water solvent for a first-radial-order WGM. Thus, by layering a microsphere with a high-index coating with a specific thickness, one can achieve robust structure, tuned for virtually any analyte, in which local temperature fluctuations do not adversely affect the sensing performance.

Acknowledgements

We thank NSERC and AITF IciNano for funding, and the Veinot lab for assistance in the preparation of the coated microsphere.

5. Refractometric sensing with silicon quantum dots coupled to a microsphere

A slightly modified version of this chapter was published in Plasmonics 8, 71-78 (2013) by Y. Zhi, C. P. K. Manchee, J. W. Silverstone, Z. Zhang, and A. Meldrum.

Abstract

Quantum dots (QDs) coupled to an optical microsphere can be used as fluorescent refractometric sensors. The QD emission couples to the whispering gallery resonances of the microsphere, leading to sharp, periodic maxima in the fluorescence spectrum. Silicon QDs (Si-QDs) are especially attractive fluorophores because of their low toxicity and ease of handling. In this work, a thin layer of Si-QDs was coated onto the surface of a microsphere made by melting the end of a tapered optical fiber. Refractometric sensing experiments were conducted using two methods. First, the sphere was immersed directly into a cuvette containing methanol-water mixtures. Second, the sphere was inserted into a silica capillary and the solutions were pumped through the capillary channel. The latter method enables microfluidic operation. In both geometries, high-visibility ($V = 0.83$) modes were observed with Q factors up to $1,700$. Using standard signal processing methods applied to the whispering gallery mode (WGM) spectrum, sensorgram-type measurements were conducted using single Si-QD-coated microspheres. The WGM resonances shifted as a function of the refractive index of the analyte solution, giving sensitivities ranging from 30 to 100 nm/refractive index unit (RIU) for different microspheres and a detection limit on the order of 10^{-4} RIU.

5.1 Introduction

Fluidic devices capable of detecting a desired analyte in lab-on-a-chip or "small device" configurations could meet the need for a wide range of sensing applications, from drug delivery to clinical diagnosis and field-based environmental monitoring [205, 206]. Surface plasmon resonance (SPR)-based systems are among the most advanced optical technologies at this point. Several biosensor devices based on SPR physics are now available on the market [207]. These sensors feature established surface functionalization chemistries that have enabled the specific detection of many different analytes. Although demonstrating numerous attractive characteristics, commercial SPR sensors are generally based on robust but bulky prism coupling configurations to detect the reflected light. Considerable effort is currently being focused on fiber- or waveguide-based SPR devices that have a smaller footprint [208].

Optical microspheres provide an intriguing potential alternative to SPR-based sensing methods [21]. These structures offer many similar benefits, including potentially high sensitivity and label-free sensing of specific target biomarkers [209]. Fluorescent microspheres (sometimes called "active" microspheres if lasing can be achieved) [210] can reduce experimental complexity associated with evanescent wave measurement systems. In these structures, whether active or passive, the light from a fluorophore such as a laser dye or quantum dots located in the near-surface region of the microsphere interacts with the optical resonances known as the whispering gallery modes (WGMs). WGMs are electromagnetic field resonances with a large amplitude near the equator of the microsphere and an evanescent tail extending into the surrounding medium. This evanescent component of the WGM responds to changes in the optical constants of the local medium, resulting in a shift of the resonant frequencies or a change in the quality factor Q (where $Q = f/\Delta f$ defines the "sharpness" of the resonance).

There are two general methods by which WGM-based optical sensors can operate, using either evanescent coupling or fluorescence spectroscopy (Figure 37). In the evanescent case, light from a tunable laser is transferred to a microsphere, typically using a tapered fiber brought within a few hundred nanometers of the sphere boundary (Figure 37(a)). The evanescent field couples into the sphere and the WGMs appear as dips in the transmission spectrum. While the detection limit of these measurements is low due to the high resolution of tunable laser systems, this method requires costly and delicate apparatus. In contrast, the WGMs can be observed as peaks in the fluorescence spectra if the microsphere is doped with a suitably emissive

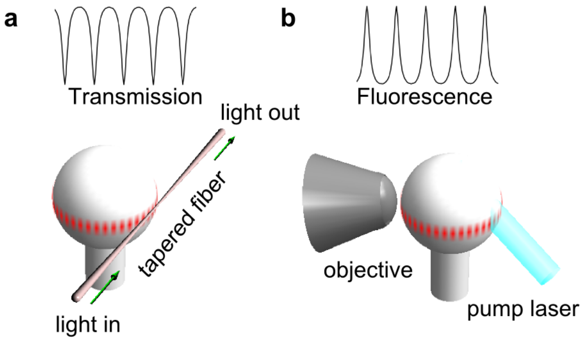

Figure 37. Illustration of the two main methods for measuring the WGMs of a microsphere. In (a), the mode spectrum is obtained by coupling light from a tuneable laser into a single mode tapered fiber held within $100-500$ nm from the microsphere surface. The WGMs appear as minima in the laser transmission spectrum. In the fluorescence case depicted in (b), the WGMs are measured by exciting a fluorophore (here, Si-QDs) with a blue laser, collecting the light with a microscope objective, and analyzing it with a spectrometer. The WGMs are measured as maxima in the fluorescence spectrum.

material (Figure 37(b)). In this case, the sensitivities are limited by the lower resolution of spectrometer-based measurements; however, the sensor structures can be more durable, robust, and more readily incorporated into different sensing geometries. Both designs (evanescent and fluorescent) may compete with SPR technologies when focusing on device miniaturization [211, 190].

In this work, a thin layer of fluorescent silicon quantum dots (Si-QDs) was coated on the surface of a silica microsphere fabricated by melting the end of a tapered fiber. Si-QDs have quantum yields claimed to be as high as 60% [117]. They show a good resistance to photobleaching [212], and they are inherently compatible with silicon-based microphotonic systems. For sensing applications, Si-QDs also have low toxicity [127] and their oxides can be surface functionalized [73], making them amenable for biosensing applications. The main objectives of this work were, therefore: (a) to determine the refractive index sensitivity and detection limits for Si-QD-layered microspheres; (b) to examine possible microfluidic coupling of such structures; and (c) to demonstrate real-time data collection and analysis (i.e., sensorgrams), as typically performed in SPR devices.

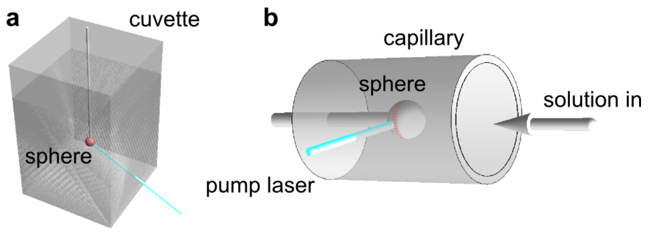

Figure 38. Diagram of the experimental setups. (a) The bulk setup, in which a single microsphere was dipped into the solution for measurement. (b) The “microfluidic” setup in which the sphere was inserted into the channel of a microcapillary.

5.2 Experimental methods

The silica microspheres were made by melting a tip of an optical fiber, using a CO_2 laser. The unfused part of the fiber acts as a stem that supports the microsphere for insertion into the fluid chamber (Figure 38). A layer of Si-QDs was then formed on the surface of the microsphere, using a coating method we described in detail previously [133, 213]. In brief, the microsphere was first dipped into a solution of hydrogen silsesquioxane (HSQ) dissolved in methyl isobutyl ketone for about 30 s. Removing the microsphere from the HSQ solution leaves a thin layer that uniformly coats the sphere surface. The microsphere was then annealed at 1, 100 °C for 1 h in an atmosphere of $95\%N_2{+}5\%H_2$ in order to segregate the film into a two-phase mixture of silicon nanocrystals and amorphous SiO_2. This procedure results in a submicron coating consisting of Si-QDs embedded in a silica matrix [213].

In both setups, the Si-QD fluorescence was excited with either the 488-nm line of an Ar^+ laser with an incident power on the sample of about 45 mW or with a 445-nm “laser pointer” with an incident power of about 700 mW. The fluorescence was collected through a microscope objective and sent to a standard Czerny–Turner spectrometer (the SGS from the Santa Barbara Instruments Group). The CCD was calibrated for both wavelength and intensity, using an HgAr lamp and a standard blackbody radiator, respectively.

5.3 Modeling and simulation

Basic Theory

The WGMs were modeled using methods developed by Teraoka and Arnold, for three-layered systems with spherical geometry [131, 130]. This method solves for the roots of the characteristic equation describing the electric field in a layered sphere:

$$E_l(r) = \begin{cases} A_l\Psi(n_1kr) & r < a-t \\ B_l\Psi(n_2kr) + C_lX_l(n_2kr) & a-t < r < a \\ D_lX_l(n_3kr) & r > a \end{cases} \tag{121}$$

In Equation (121), n_1, n_2, and n_3 are the refractive indices of the microsphere, the QD film, and fluid medium, respectively, Ψ_l and X_l are the l^{th} cylindrical Riccati-Bessel and Riccati-Neumann functions, and A_l, B_l, C_l, and D_l are coefficients. The solutions to these expressions are obtained by setting the boundary conditions as usual (e.g., the transverse electric (TE)-polarized field must be continuous across both interfaces) and solving for the roots of the resulting expression. These expressions, while too long for reproduction here, can be solved by numerical integration and rootfinding methods in standard mathematical software packages. This leads to the resonant wavevector and sensitivity for any given resonance of the sphere.

While Equation(121) can be used to quickly find the wavelength and refractometric sensitivity for a single n, l mode for any set of refractive indices, and film thickness, full spectral modeling requires the use of finite difference time domain (FDTD) simulation. Matching the simulation with experiment permits complete mode identification for all WGMs in the spectrum and provides an independent estimate of the QD film thickness, refractive index, and extinction coefficient. FDTD simulations were performed with the commercial software package OmniSim, from Photon Design. Standard methods with respect to grid size, the number of time steps, absorption coefficient, and matching layers were used to ensure that the effects of artifacts in the simulation were minimized [214].

Comparison with experiment

The WGMs were clearly developed in the fluorescence spectrum of the Si-QD-coated microspheres. Both TE and TM modes were present, with the TE polarization tending to show a higher visibility ($V_{TE} = 0.83$ vs. $V_{TM} = 0.56$, for the best spheres). For this reason, the TE resonances (Figure 39) were used for refractometric sensing measurements and Figure 39(b) shows the photoluminescence image. The resonance Q factors of these modes were as high as 1,700, the free spectral range was ~ 3 nm, and the finesse was typically on the order of 3. A secondary family of maxima with a lower intensity and slightly larger free spectral range was also present.

Simulation and modeling were employed to characterize the resonances and to

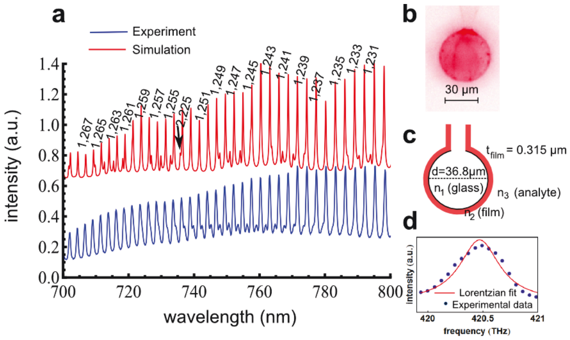

Figure 39. (a) Comparison of TE-polarized experimental (blue) and FDTD-simulated spectra (red) for the parameters shown in (c), in which n_3 is for water. The mode numbers are labeled just above the simulated spectra. The arrow points to one of the second-order radial modes. The agreement between experiment and theory is reasonably good across the entire spectral range. The mode visibility was approximately 0.4 for this sphere. (b) Fluorescence image of a real sphere held in water, corresponding to the diagram in (c). (d) The experimental data for a single mode taken from (a), along with a Lorentzian fit. This shows two issues associated with conventional peak shift measurements: the spectrum is not well-defined by a Lorentzian, and the sampling rate (0.1 nm/pixel) is rather low for this mode ($Q \approx 1,000$).

refine the estimates of the film thickness t_{film} and microsphere diameter d_{sphere}. First, Equation (121) was used to estimate these parameters, by assuming a known film and glass refractive index of 1.67 [132] and 1.452, respectively, and varying t_{film} and d_{sphere} until the wavelength of two adjacent TE modes agreed with experiment. These results were input into the FDTD simulations and further refined until the experimental and simulated spectra matched closely (Figure 39(a)). For these simulations, we used an absorption coefficient of 0.94 cm^{-1} as measured for flat QD films that were made by an identical process [215].

There is good overall agreement between the experiment and simulation, in terms of the resonant wavelengths, free spectral range, Q factors, and the position of the secondary family of maxima (Figure 39(a)). These results permit the mode numbers to be unambiguously assigned in the spectrum and predict a refractometric sensitivity of 40.7 nm/refractive index unit (RIU) for the TE-polarized field with an external refractive index of 1.322 (i.e., that of the average of water and methanol at $\lambda = 775.9$ nm), for reasons given below. The main peaks were found to be first-order radial modes, while the secondary family of smaller peaks represents the second-order modes. As discussed in the following section, this overlap of different radial mode families can present a problem for measuring the mode shifts associated with the refractive index changes.

Mode shift measurement

In order to determine the resonance shifts ($\delta\lambda$) due to a change in the external refractive index, one must obtain a good estimate of the WGM peak position. In our opinion, this key aspect of WGM fluorescence sensing is not always considered in sufficient detail. One of several methods will typically be used to determine the central wavelength:

- Simply picking the highest point in the peak may work well if the modes are well sampled and the signal-to-noise ratio (SNR) is high [215].
- Parametric waveform analysis (i.e., curve fitting) can be accurate even for fairly low SNR, as long as one has an accurate mathematical model describing the peak shape [141].
- Autocorrelation with respect to the original spectrum can be effective if the SNR is sufficiently high [189].
- Least squares mathematical modeling of the entire WGM spectrum [18] can be sensitive to very small shifts but appears difficult and time-consuming to implement.

The relatively high luminescence Q factor combined with the 0.1 nm/pixel pitch of our spectrometer results in a poor sampling of the WGMs (Figure 39(d)). The mode shape does not appear Lorentzian, possibly owing to overlap between the first- and second-radial-order mode families. Furthermore, the SNR is approximately 37 dB (for a 100 s collection time), which is low compared to measurements made with evanescent coupling setups. Thus, none of the above methods would seem well-suited for obtaining accurate mode shift information from these spectra.

We instead used standard Fourier signal processing methods to obtain the mode shifts. The periodic nature of the WGM spectrum makes it a perfect candidate for waveform shift measurements based on the discrete Fourier transform (DFT). This method has the secondary advantage that it is simple to incorporate for “live time” sensorgram measurements. The basic steps were as follows: the spectra were first converted into frequency units in order to ensure a constant period (i.e., a uniform free spectral range); they were then resampled using linear interpolation methods to obtain uniform frequency spacing [216] and finally transformed to obtain the power and phase spectra of the Fourier series.

The resulting phase shifts (for all phases) were calculated, and a linear regression was performed on the shifts $\Delta\phi$ for each Fourier component p (i.e., the "shift theorem") and weighted according to the corresponding power of each component. This assumes that the spectra are shift invariant, which should be a reasonable assumption at least for small refractive index changes. The frequency shift is then given by $\Delta f \approx \Delta\varphi_p(f_{max} - f_{min})/2\pi$, with $\Delta\varphi_p$ equal to the slope of the weighted fit and f_{min} and f_{max} representing the spectral range. Filtering was performed in order to remove the high and low frequency components of the spectrum prior to fitting. While the choice of filtering is arbitrary, removal of high-frequency noise and long-wavelength oscillations (e.g., the underlying non-cavity-coupled fluorescence) is a standard procedure in many fields [217]. With this method, the spectral shifts are obtained from the entire spectrum, not from any individual peak. The method is insensitive to noise, can detect small shifts, does not require mathematical modeling of complicated peak shapes, is not greatly hindered by overlapping mode families, and is based on entirely standard signal processing methods that are easily incorporated into any analysis system.

5.4 Refractometric measurements

"Bulk" system analysis

Refractometric measurements were then performed on a set of water-methanol solutions. Each solution was injected sequentially into a 3.5-mL cuvette, the fluorescence spectrum was collected, and the solution was subsequently removed with the same syringe before the cuvette was refilled with the next solution. The resulting fluorescence spectra are shown in Figure 40. The WGM spectrum remains largely unchanged in all solutions, except for a slight mode shift due to the different solution refractive indices. The mode shifts, $\delta\lambda$, appear non-monotonic; initially, there appears to be a redshift as the methanol concentration increased, followed by a subsequent blueshift for the highest methanol concentrations.

Although these non-monotonic spectral shifts may seem surprising, this behavior is in fact expected for mixtures of methanol and water. Both molecules are polar and form an "associate" that becomes the major component of the overall mixture at intermediate compositions [218]. This associate phase has a higher refractive index than either pure water or methanol and therefore a higher index than any linear combination of the two. Thus, the non-monotonic resonance shifts (Figure 40) are closely consistent with the expected evolution of the refractive index as a function of

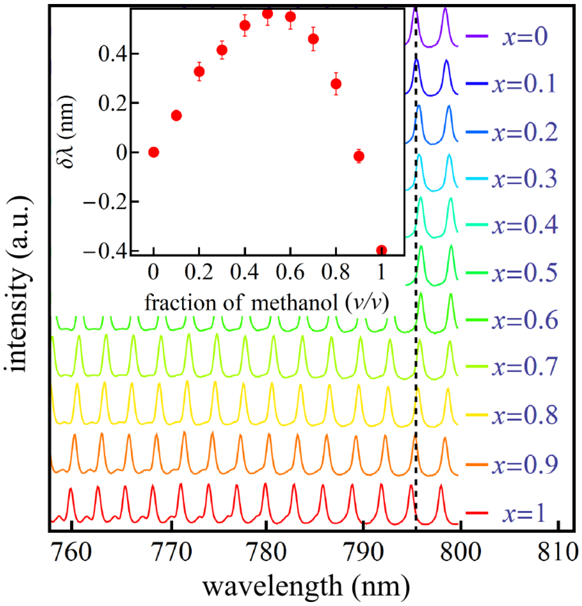

Figure 40. Fluorescence spectra from a microsphere held in a cuvette, for a variety of different methanol-water mixtures. The spectra are cropped horizontally and vertically offset for clarity. The label x represents the volume fraction of methanol, and the vertical dashed line is a reference point from which the mode shifts can be more easily seen. The inset shows the shifts calculated from the Fourier analysis of the spectra shown in the main panel; the error bars are the uncertainties from the weighted fit to phase shifts of each Fourier component within the filtering range.

methanol concentration in the solution [219].

The microsphere sensitivity can be measured using the pure phases, since their refractive indices can be calculated at any wavelength using the known Cauchy parameters for methanol [220] and water [221]. Accordingly, the average sensitivity of this microsphere over the refractive index range from pure methanol to water was found to be 30 nm/RIU, which is somewhat lower than the theoretical average calculated above. The overall resolution (i.e., minimum detectable wavelength shift) can be estimated as 3σ of the errors in the weighted least squares fit of the Fourier phase shifts. With a best case uncertainty on the order of 10 pm, the detection limit is in the range of 10^{-4} RIU.

Microfluidic with a microsphere

Having established that the Si-QD-coated microsphere has a good WGM structure in its fluorescence spectrum and a reasonable sensitivity and detection limit (for a fluorescent device), we next attempted to determine whether it can work in a microfluidic setup. To achieve this, the microsphere was inserted into the channel of a microcapillary. One end of the capillary was attached to a micro-syringe pump and the other end, through which the sphere was inserted, was used for fluid disposal.

The greatest difficulty in this work was found to be in the focusing of the sphere when the solutions were pumped into the channel. Essentially, the capillary acts as a diverging lens for any point away from the exact center of the channel. In practice, we found that focusing the microsphere onto the spectrometer slit tended to be difficult, requiring repeated manipulation of the experimental setup and of the microsphere's horizontal and vertical position inside the capillary. In the future, square profile capillaries should be a better option to minimize lensing effects; however, in a few cases at least, it was possible to achieve reasonably well-focused spectra. An example is shown in Figure 41, in which we see a fluorescent microsphere inserted into a capillary, with water contained in the channel.

A set of methanol-water mixtures was then pumped into the capillary channel and the WGM resonance shifts of the microsphere were sequentially measured. The overall trend followed closely the results of the previous section, except that the fluorescence spectra are somewhat weaker and noisier than in the previous case, and the uncertainties in the spectral shifts are therefore larger. Nevertheless, these results show that microfluidic operation via single microsphere insertion into a capillary is a viable option for these QD-coated fluorescent microcavity devices.

Sensorgrams

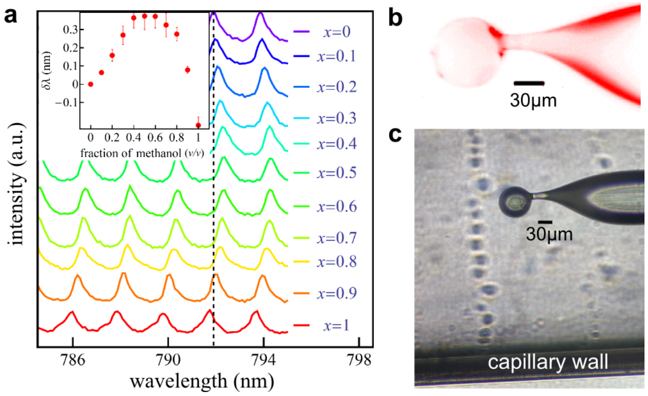

Figure 41. (a) A section of the fluorescence WGM spectra collected from a microsphere inserted into a glass capillary, as a function of the methanol concentration, x, by volume. The dashed vertical line is a guide to the eye, for tracing the shifts $\delta\lambda$. The inset shows $\delta\lambda$ as a function of methanol concentration obtained from a Fourier analysis of the fluorescence WGM spectra. The error bars represent the uncertainty from the weighted fits to the Fourier series phase shifts. (b) A fluorescence image of the microsphere in the capillary. (c) A transmitted light image of the same microsphere.

The Fourier methods for finding the spectral shifts readily enable sensorgram operation for fluorescent microspheres. To demonstrate this, a newly made Si-QD-coated microsphere was inserted into a cuvette and immersed in 2 mL of deionized water. Then, 0.3 mL of ethanol was added to the cuvette, using the micropumping system described above. Over this range of concentration from 0 to 13.0% (v/v) ethanol in the analyzed solution, the refractive index varies nearly linearly with composition [222], and the net mode shift estimated theoretically from Equation (121) should be less than half a free spectral range. The latter is necessary to prevent the phase from "jumping" by one wavelength when the total forward Fourier phase shift exceeds a value of π. The injection tube nozzle was approximately 2 cm from the sphere and the volume flow rate was 0.005 mL/min, corresponding to a fluid speed of 0.143 mm/s in the tube. The total flow time was 1 h.

Spectral images were collected continuously as the water-ethanol solution was injected into the cuvette. A 100-s collection time was used for each image, automatically collected over a period of 4.9 h. The resonance shifts obtained from the Fourier transform of the WGM mode spectra are plotted in Figure 42. Initially, there was a gradual blueshift of approximately 50 pm, over a period of 105 min. The initial blueshift is likely caused by a small temperature rise of the water solution, as a result of the pump laser. The thermo-optic coefficient of water is on the order of -10^{-4} K^{-1} in this range [219]. Based on the measured sensitivity of 107 nm/RIU for this sphere,

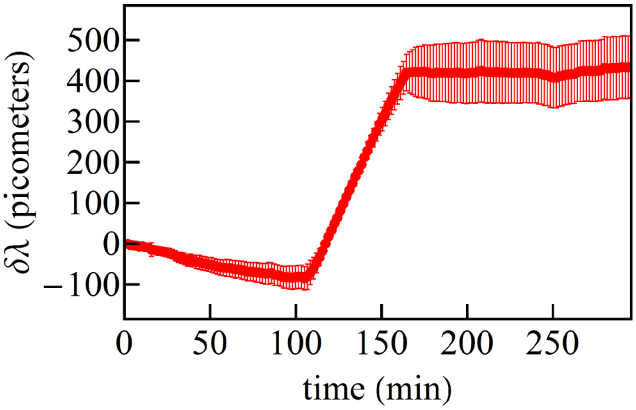

Figure 42. Sensorgram showing the evolution of the spectral shift, $\delta\lambda$, as a function of time. As usual, the error bars represent the uncertainty from the weighted fits to the Fourier series phase shifts.

a 50-pm blueshift corresponds to a temperature increase of about 7.9° in the cuvette. Consistent with this interpretation, in experiments using a low laser power, this initial blueshift was not observed. We note that the higher sensitivity for this sphere is almost certainly due to differences in diameter and especially QD film thickness, which can have a profound effect on the sensitivity of a three-layered spherical cavity [130, 214].

After 117 min, the WGM spectra underwent a sudden rapid redshift. This happened at the point in time when the injected ethanol reached the microsphere. The spectral shift attained a value of 420 pm before leveling off to a constant value. The time taken for this process to occur is due to a combination of diffusion of ethanol in water and the initial injection speed of 0.143 mm/s. Based on the diffusion coefficient for ethanol in water of 1.23×10^{-5} cm^2/s [223], the ethanol should be detectable in about 90 h if the motion is purely diffusional. The 52-min timescale required in this case was therefore mainly controlled by initial fluid injection velocity.

5.5 Conclusions

Fluorescent silica microspheres coated with a layer of silicon quantum dots are promising as microfluidic sensor devices. In this work, we found a well-developed whispering gallery mode structure with Q factors over $1,500$. The refractometric sensitivity $\delta\lambda/dn$ is enhanced by the presence of a high-index surface layer, reaching values up to 107 nm/RIU in one sample. In future work, we will attempt to control the QD film thickness to enhance the overall sensitivity (currently, the thickness of the QD film is not a controlled parameter). Using standard signal processing methods, spectral shifts as small as a few picometers can be resolved, even with a standard small-footprint spectrometer with a pitch of 0.1 nm/pixel and a nominal resolution of 0.24 nm. With these values, the detection limit should be on the order of 10^{-4} RIU.

This work demonstrated microfluidic and sensorgram-type operation of single QD-coated fluorescent microspheres. Microfluidic measurements were demonstrated by inserting individual sphere into the channel of a microcapillary and then pumping various fluids into the capillary while monitoring the WGM spectrum. Measurements were found to be rather difficult in this geometry, as a result of capillary lensing effects; in future work, therefore, square profile capillaries will be employed instead. Sensorgrams were also demonstrated by applying simple Fourier methods to a set of continuously collected WGM spectra. Here, each time point was 100 s, but much faster results could be obtained if the signal-to-noise remains sufficiently high for Fourier series analysis of the data, within acceptable errors. While the sensitivity remains lower than for competing SPR-based devices, these structures could be used for live time measurement of the temperature, diffusion coefficients, or mixing speeds for any mixture of transparent fluids. Additionally, the QD coating should readily permit surface functionalization for specific detection of target analytes in sensorgram format, as recently shown for the detection of biotin and streptavidin [224]. The method is additionally robust, experimentally inexpensive, and readily compatible with microfluidic analysis.

6. Silicon quantum dot coated microspheres for microfluidic refractive index sensing

A slightly modified version of this chapter was published in the Journal of the Optical Society of America B 30(1), 51-56 (2013) by Y. Zhi, T. Thiessen, and A. Meldrum.

Abstract

The electromagnetic resonances of optical microspheres - the so-called whispering gallery modes (WGMs) - can be used for refractometric sensing of surrounding fluids. Microspheres are attractive because they offer high sensitivity and can be utilized with fluorescent dyes or quantum dots. One issue with microspheres, however, is that they are difficult to integrate into microfluidic systems. Here, we develop a microfluidic structure that permits sensing applications using a single microsphere in a capillary. To achieve this, a microsphere formed on the end of a tapered fiber was first coated with fluorescent silicon quantum dots (QDs). The sphere was then inserted into a microcapillary and the fluorescence WGMs were monitored as different fluids were pumped through the channel. The sensitivity and detection limits for this sphere-in-a-capillary device were measured for several different QD film thicknesses and for two different microsphere sizes. Because of the relatively high-visibility mode structure, the sensitivity and detection limit can be defined by Fourier analysis of the free spectral range and WGM spectral shifts.

6.1 Introduction

Combining optical sensors with microfluidic systems could lead to the development of miniaturized "on-chip" detection devices [225, 226]. Microscale optical sensors can permit the analysis of subnanoliter volumes of fluid; such devices can also meet the necessities of small size, low cost, and short analysis times associated with Lab-on-a-Chip (LoC) based technologies [227]. Optical microcavities such as photonic crystals [228], microcapillaries [229], and microdisks [230] are naturally compatible with LoC systems and have been investigated for refractometric sensing [231, 232].

In microcavities with a circular symmetry (microspheres, disks, and cylinders) light circulates by total internal reflection around the equator of the structure, leading to the formation of electromagnetic resonances known as the whispering gallery modes (WGMs). A fraction of the electric field profile of the WGMs extends into the medium outside the structure, forming the basis of the sensing mechanism. The WGMs are characterized by both the resonant frequency, f_0, and the Q factor ($Q = f_0/\Delta f$, with Δf being the resonance linewidth). Both f_0 and Q can be sensitive to changes in the surrounding medium [209, 19]. In microspheres, the WGMs can have extraordinarily high Q factors, which (within data-sampling-related limits) makes them attractive for sensing applications [233].

Microspheres generally require an external analyte chamber [234], and are therefore difficult to integrate into LoC-type designs that require both optical and fluidic access to the sensor [235]. One suggested solution uses optical tweezers to position the sphere near the analyte [236], although at the cost of experimental complexity. Special fluid cells [152] may present another option. In addition, coupling into the WGMs can require delicate tapered optical fibers [237], accurate positioning of a waveguide and a fluid channel with respect to the sphere surface [235], or the use of bulky prism couplers [238]. These issues can hamper the application of microspheres in LoC-type analysis devices.

In this work, we demonstrate a single fluorescent microsphere utilized as a microfluidic sensor. Dye- or quantum-dot-doped microspheres [14, 239, 139] operate in the fluorescence mode, obviating the need for an evanescent coupling apparatus. The basic method is to deposit a uniform layer of silicon quantum dots (Si-QDs) on the surface of a microsphere, which is held on the end of a fiber taper. The microsphere is inserted into a capillary (Figure 43), and different fluids are then pumped through the channel while monitoring the WGMs in real time. This method represents one way to solve the external chamber issue and permit "live-time" sensorgram analysis.

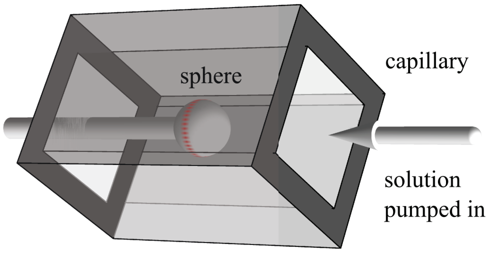

Figure 43. Microfluidic setup. A single microsphere coated with a layer of Si-QDs is inserted into a square capillary. The fluorescence WGMs are activated by a blue laser and collected via an objective just below the capillary. The solution is injected into the capillary using a microsyringe pump.

6.2 Experimental

First, a microsphere was made by melting the end of an SMF-28 optical fiber, using a CO_2 laser. A film of silicon QDs was then formed on the microsphere surface by a dip-coating method that we recently developed [132, 240]. Briefly, the sphere was held in a solution of hydrogen silsesquioxane (HSQ) dissolved in methyl isobutyl ketone. Upon removal from the solution, a thin film remains on surface of the microsphere. Annealing the film at 1100 °C for 70 min in a $95\%N_2+5\%H_2$ ambient causes the evaporation of excess solvent and the collapse of the HSQ cage-structure molecules, to form well-passivated Si-QDs embedded in a glassy matrix [241]. The end result is a uniform fluorescent Si-QD coating on the surface of the microsphere. Although the exact film thickness per coating could not be determined in the present case, we assume similar sub-micrometer thicknesses as for fibers and free surfaces coated by the same method [221]. Two spheres were tested, referred to as spheres 1 and 2 with diameters of 64 and 59 µm, respectively. The effect of the QD layer thickness was investigated by repeating the QD film coating step several times.

The microspheres were inserted into the channel of a square capillary with a 700 µm inner cross-sectional length (see Figure 43). The capillary was interfaced on one end to a microsyringe pump. Excess fluid pumped through the capillary was captured at the opposite end, in a small disposal container. The Si-QDs were excited using the 445 nm line of a high-power diode laser. The 700 mW beam was incident in free space through the side of the square capillary, which was placed on the stage of an epifluorescence microscope. The QD fluorescence was collected through a 10× microscope objective (numerical aperture of 0.22) and sent either to a color camera (Retiga EX) or to a spectrometer with a nominal resolution of 0.24 nm and a pitch

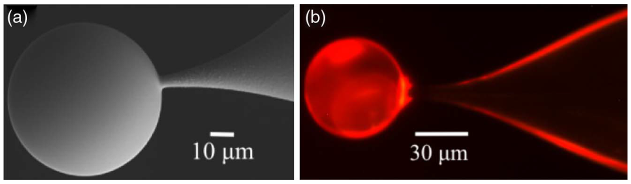

Figure 44. SEM image of a microsphere with a single-QD coating. (a) The sphere appears smooth and featureless at this magnification. (b) Fluorescence image of sphere 2 (diameter: 59 µm), with a quadruple-coating of Si-QDs. The sphere is immersed in water, inside a capillary channel (the channel walls are outside the image). The stem also fluoresces, since the microsphere was dipped to a depth of several mm during the QD fabrication procedure.

of 0.1 nm/pixel (the SGS from Santa Barbara Instruments Group). Spectra were collected continuously as three solutions were pumped sequentially into the capillary: first ethanol, then a 1 : 1 by volume ethanol:water mixture, and finally pure water. The refractive index used to estimate the device sensitivity for these three solutions was 1.3589, 1.3568, and 1.3326, respectively [221, 222]. All fluorescence spectra were calibrated for wavelength and intensity by using an HgAr lamp (manufactured by CVI) and a blackbody radiator (Ocean Optics).

6.3 Results and analysis

The Si-QD coating was smooth and uniform (Figure 44(a)). When excited with a blue laser, a red emission typical of oxide-embedded Si-QDs [242, 243] was observed in the fluorescence images (Figure 44(b)). The use of a square capillary as opposed to the normal circular ones was found to greatly reduce the lensing problems that made fluorescence imaging and spectroscopy otherwise very difficult. Clear and well-focused fluorescence images such as that in Figure 44(b) were easily obtainable for all three solutions in the capillary.

The corresponding spectral image of a double-QD-coated microsphere is shown in Figure 45. The mode structure appeared especially well developed near the sphere edges, and was clearly divided into the TE and TM polarizations, as determined by inserting an analyzer into the light path. Here, we refer to the polarization direction with respect to the plane of the WGMs; hence, the TE modes have the electric field polarized parallel to the fiber stem, as shown in Figure 45(a). The TM modes were weaker and extended further into the fluid medium surrounding the sphere (Figure 45(c)).

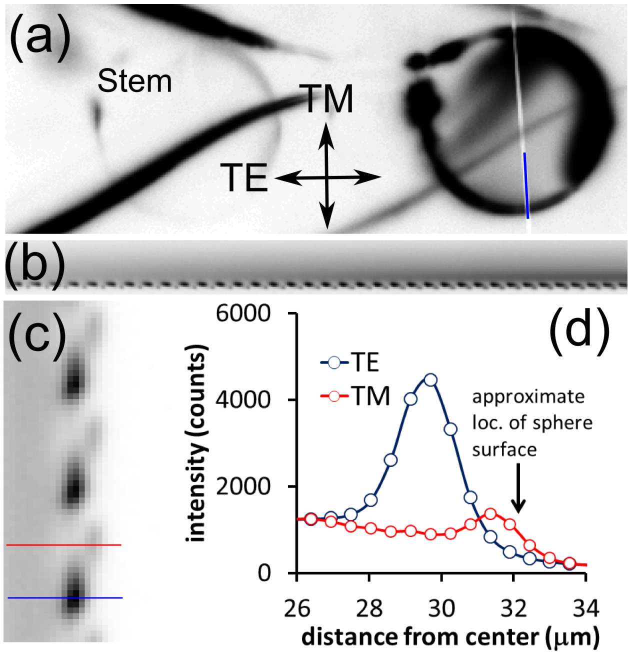

Figure 45. (a) Fluorescence “tracking” image of sphere 1, with a double-coating of Si-QDs (monochrome, inverted contrast; diameter: 64 μm; a faint double-image is visible). The E-field directions for the TE and TM polarizations are shown, and the spectrometer slit is observable bisecting the microsphere at a slight angle. (b) A spectral image taken from a region corresponding to the blue line in the slit image in (a). (c) A magnification of a small part of the spectral image (rotated 90°). The blue (dark) and red (light) lines in (c) correspond to the TE and TM intensity profiles in (d).

The fluorescence spectra showed a set of closely-spaced high-visibility modes ($V \approx 0.74$), where the visibility is defined as usual as $(I_{max} - I_{min})/(I_{max} + I_{min})$ and Q factors up to ~ 2000 (Fig. 46(a)). The overall fluorescence intensity was strongly increased upon the application of a second QD coating. The Q factors are probably limited by the linewidth of the individual QDs [45], since our previous tunable-laser transmission measurements through a fiber taper yielded Q factors in the range of 10^5. The TE-polarized WGMs were more intense than the corresponding TM modes (Fig. 46(b)). Numerical modeling [130, 131] and finite difference time domain simulations suggested that the observed WGMs are first-order radial modes having angular numbers on the order of 400 for sphere 1 and 350 for the smaller sphere 2. The precise angular number for each mode could not be determined unambiguously, due to uncertainties in the refractive index and size of the sphere, and the QD layer thickness.

The central wavelength for each WGM is difficult to determine by standard Lorentzian curve fitting, due to sampling problems (i.e., each peak is defined by only a few data points, as shown in the inset to Figure 46(b)). Furthermore, overlapping second-order radial modes can complicate the curve-fitting procedure [158]. Therefore, the mode shifts caused by changing the refractive index of the fluid in the channel were measured by converting to frequency units and using Fourier methods over the entire spectrum [141], rather than by attempting to fit a Lorentzian function to individual WGMs. The method has been discussed in detail previously [141], and will only be outlined briefly here. The wavelength shifts obtained in this way are properties of the whole spectrum, as opposed to a single mode.

Essentially, a discrete Fourier transform is taken for all fluorescence spectra, to obtain both the Fourier power and phase spectra. The shift theorem states that, assuming a pure shift, all p Fourier components are shifted in phase by an amount proportional to the component, i.e., $\Delta\phi = \Delta\phi_p p$ where $\Delta\phi$ is the phase shift of the pth component and $\Delta\phi_p$ is a proportionality constant that depends on the real shift. A pure shift is a reasonable assumption for high-angular-order WGM spectra, in which the sensitivity does not vary much over the wavelength range investigated. In order to find $\Delta\phi_p$, we take a weighted linear fit to the phase differences for the main components of the power spectrum, with the weighting of each component proportional to its power. Then the real shift, in frequency units, is $\delta f = \Delta\phi_p(f_{max} - f_{min})/(2\pi)$, where $f_{max} - f_{min}$ is the spectral range of the measurement. All phase differences are taken with respect to the (arbitrary) initial spectrum. The resulting δf (or $\delta\lambda$, with appropriate conversion) represents a shift over the whole spectrum.

In order to ensure that the frequency shifts and the free spectral range (FSR)

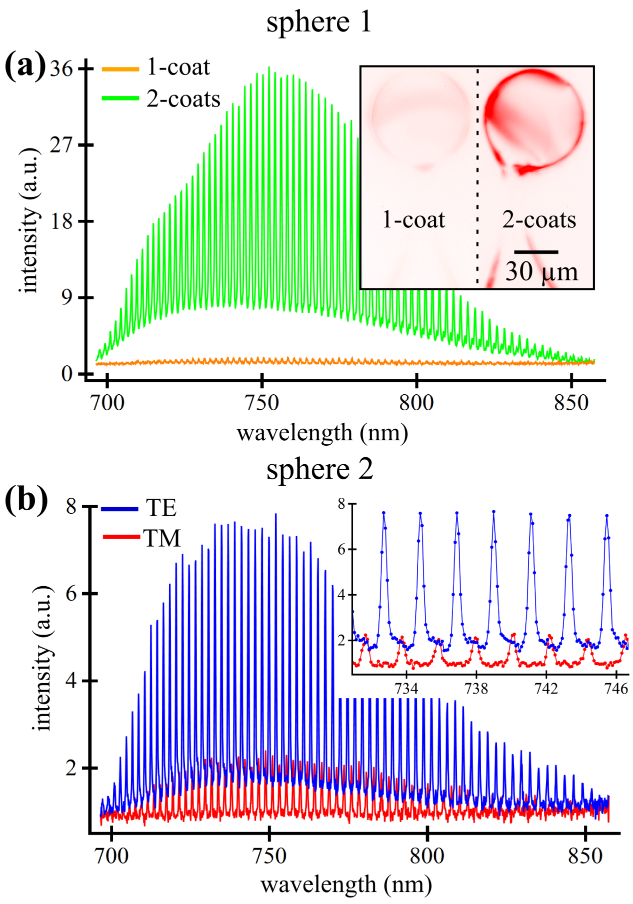

Figure 46. PL spectra for sphere 1, with a single (dark orange) and double (light green) Si-QD coating (a). The inset shows the PL image of the sphere with a single coating (left) and double coating (right). The images have been inverted from black to white contrast but have not been enhanced; thus, the single coating (left image in inset) is very faint. (b) TE (dark blue) and TM (light red) polarized WGM spectra for sphere 2 (double coating). The inset shows the mode structure and data sampling more closely.

are measured correctly, several issues must be taken into account in the analysis, as illustrated in Figure 47. One issue is the selection of the Fourier components used for the shift measurements; here, we selected only the components having a power greater than 25% of the main one, as shown in Figure 47(b). While this selection is arbitrary, it does eliminate high-frequency noise and broad background fluorescence, and establishes some consistency amongst different analyses. When converting the spectra from wavelength to frequency, we used a linear interpolation algorithm to ensure that the data was spaced uniformly in frequency units. One unavoidable difficulty with the method, especially for large shifts, is the possibility of "2π rollover" that must be corrected when the shifts are larger than π. In other words, a phase shift of $\pi + \phi$ will appear as a shift of $-\pi + \phi$.

The resulting wavelength shifts for sphere 1 (double-coating, TE polarized) are shown in Figure 47(d). The error bars represent the uncertainty in the weighted linear fitting and are effectively a measure of the uncertainty in the sensitivity of the device. For this sample, the average sensitivity, $S = \delta\lambda/\delta n$, over the range of refractive index between water and ethanol was $S_{TE} = 38 \pm 4$ nm/refractive index unit (RIU), ignoring any error associated with the refractive indices of water and ethanol.

The variation in the shift for a given compound in the capillary is, however, much smaller than the uncertainty in the overall shift. This error is a measure of the detection limits of the device. One standard deviation of the uncertainty in the peak position over the first 30 measurements of the time series was ~ 5 pm for all three solutions in the capillary. Within a 3σ degree of certainty [215], the minimum detectable wavelength shift, δf, is therefore 15 pm and the most probable detection limit is $\delta n = \delta f/S = 4.3 \times 10^{-4}$ RIU for this device.

The sensitivity of the TM modes ($S_{TM} = 44 \pm 8$ nm/RIU) appeared slightly greater than for the TE case, consistent with the greater extension of the TM-polarized field into the fluid medium surrounding the sphere (Figure 45). A greater sensitivity for the TM polarization is also consistent with the perturbation-theory approach developed by Teraoka and Arnold [130, 131]. Despite the probable greater sensitivity, however, the TM modes were always much weaker than the TE ones, and demonstrated lower Q factors ($Q_{TM} = 1040$; $Q_{TE} = 1830$ in Figure 46(b)). The TM modes concentrate more toward the film and external fluid medium, and therefore suffer greater optical losses, but have a greater sensitivity.

The sensorgrams for the TE-polarized spectra for sphere 2 (diameter 59 µm) are shown in Figure 48. Consistent with its smaller size, sphere 2 appeared more sensitive than sphere 1 (50 ± 20 nm/RIU for a double QD coating, as compared to 38 ± 4

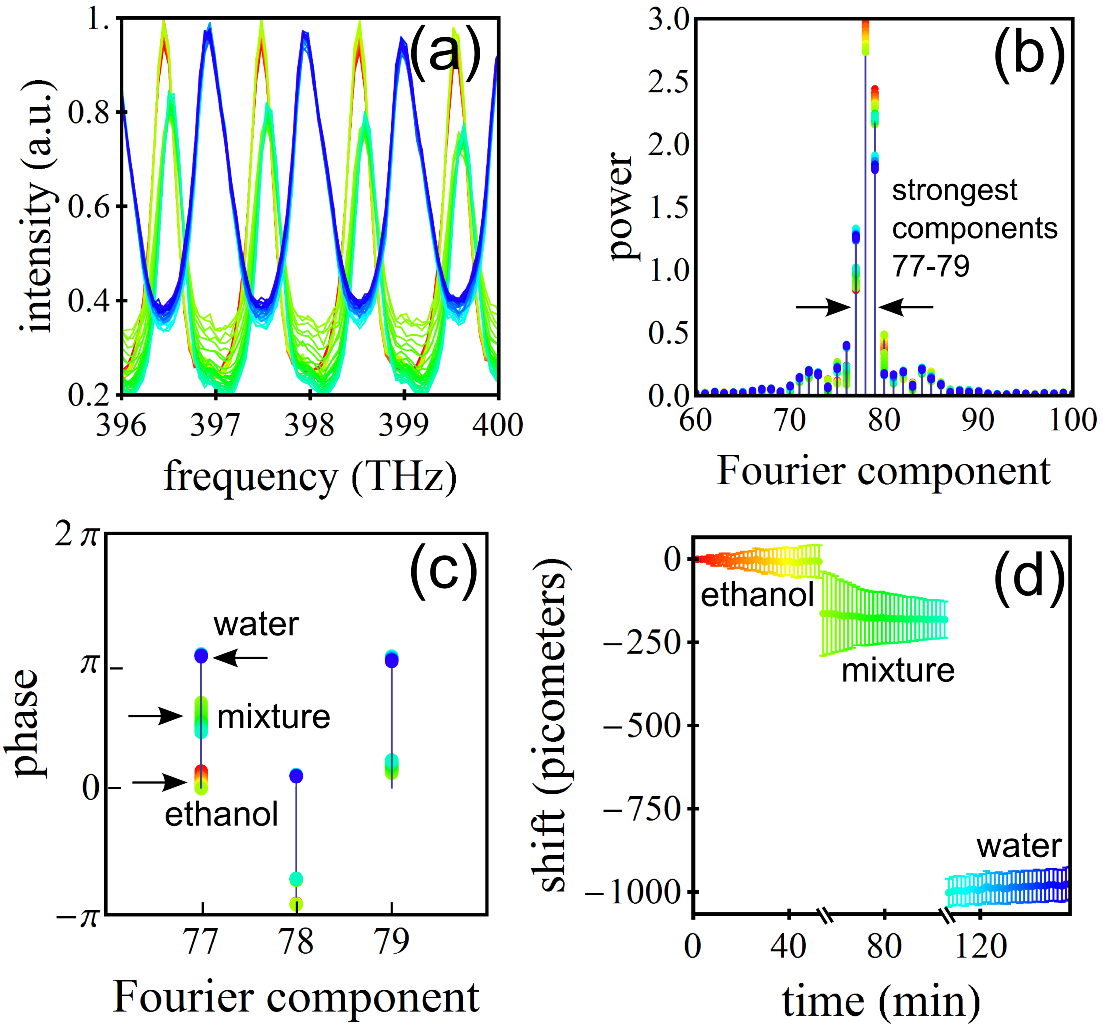

Figure 47. Part of the WGM spectrum (sphere 1, double- QD-coating, TE polarization) for 90 consecutive measurements (light red to dark blue) as ethanol, then a water–ethanol mixture, then water were pumped into the capillary (a). (b) The corresponding Fourier power spectra, showing the strongest components. (c) The phase spectra for the strongest components. (d) The resulting shift spectra, calculated from a weighted linear fitting of the phase differences in (c), and converted back into wavelength units. The breaks on the time axis indicate times when the pumping was stopped in order to change syringes. The error bars represent the 1σ uncertainty in the weighted fitting of the selected Fourier components.

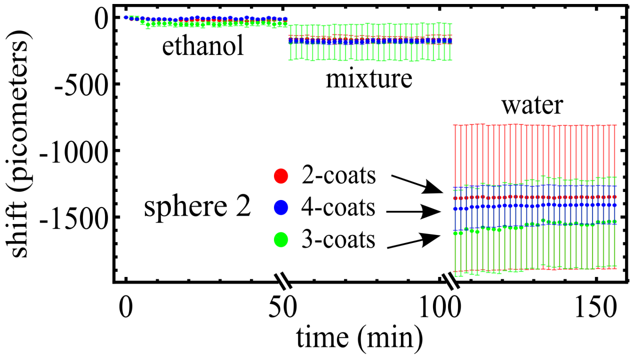

Figure 48. Sensorgram showing the WGM spectral shifts as different solutions were pumped through the capillary. Results are shown for sphere 2, with different numbers of QD coatings. The breaks on the time axis indicate time when the pumping was stopped in order to change syringes.

nm/RIU), although the error is large. In this microsphere, the uncertainties associated with the weighted linear fitting of the main Fourier components were significant (Figure 48), leading to the large uncertainty in the overall sensitivity. Still, the 3σ wavelength shift errors remained small (these ranged from 11 to 19 pm in the double- and quadruple-coated cases, to a maximum of 46 pm in the triple-coated sample). The most probable detection limits in the case of sphere 2 were 2.2×10^{-4}, 7.9×10^{-4}, and 3.4×10^{-4} RIU for the double, triple, and quadruple-coated cases. From these results, it appears that there is little advantage to coating the sphere with more than two QD layers, and that the detection limit is optimally close to 10^{-5} RIU, which is competitive for a fluorescence-based device.

The Fourier shift treatment of the WGM spectra permits the FSR to be used as an alternative sensorgram measurement (Figure 49). The FSR has a 3σ error of less than 200 MHz (~ 0.4 pm) in the best cases. Error bars are not shown in Figure 49, since a weighted fitting of the Fourier components is not required to calculate the FSR. In all samples, the FSR increased on going from ethanol, to the mixture, to water in the capillary, and it decreased progressively by ~ 4 GHz (a few pm) for each subsequent QD coating.

An alternative sensitivity and detection limit strategy can be defined by the change in the FSR as a function of the analyte index. The FSR sensitivity for sphere 1 (for a double-QD-coating) is $S_{FSR} = \delta f_{FSR}/\delta n = 75.3$ GHz/RIU; for sphere 2 it was 457.8 GHz/RIU. The increase in S_{FSR} on going from sphere 1 to 2 is larger than the corresponding increase in the shift sensitivity. Like the shift sensitivity [130, 131], the FSR sensitivity should have a nonlinear and coating-thickness-dependent relationship with the sphere size and layer thickness, so the large change in the FSR sensitivity

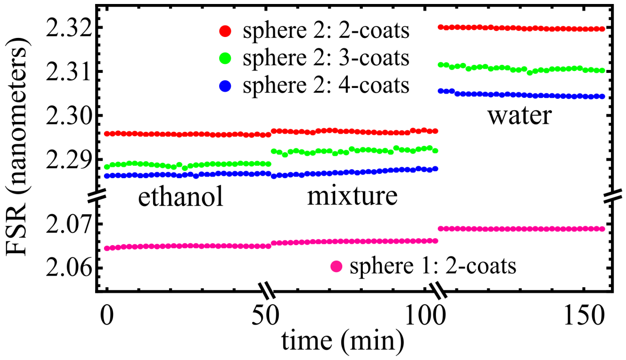

Figure 49. FSR sensorgram for sphere 1 (pink dots) and 2 (red, green, and blue dots). These values were calculated using the same rules as for the shift sensorgrams: all components smaller than 25% of the maximum filtered out in the analysis. The FSR was converted to wavelength units for visual convenience and comparison with Figure 46. The breaks on the time axis indicate time when the pumping was stopped in order to change syringes.

may be realistic. It could also be, in part, a result of experimental variations such as the exact location on the sphere from which the measurements were taken, or film thickness. Finally, the related detection limits are $\delta n_{FSR} = \delta f_{FSR}/S_{FSR}$, leading to an FSR-related detection limit of 2.7×10^{-3} and 4.4×10^{-4} RIU for spheres 1 and 2, respectively.

The sensorgram measurements indicate that there is little temperature-induced shift of the resonance wavelengths that could contribute to errors in the measurements, despite the high laser power of 700 mW. This is unlike the case for cuvette-based measurement using similar QD-coated microspheres [158] in which a WGM blueshift was observed as a function of time, owing mainly to the negative thermo-optic coefficient of water. While some measurements did show apparent drifts [for example, see the FSR results for sphere 2 (quadruple-coated—blue dots) in the center of Figure 49], generally we did not observe consistent drifts in the mode positions as a function of laser exposure time. This is probably because, unlike for a cuvette, these measurements use a continuous fluid flow in the capillary channel.

6.4 Conclusions

A microfluidic refractometric sensor structure was built by inserting a quantum-dot-coated microsphere into a square-profile microcapillary. The device eliminates the lensing issues that exist for imaging structures inside a fluid-filled circular-profile capillary. It also solves the “external chamber problem” associated with microsphere-based refractometric sensing methods and permits the operation of a microsphere in a microfluidic environment. Two spheres of different radii and quantum-dot layer thicknesses (i.e., number of coatings) were compared. Both spheres showed a red fluorescence with WGM Q factors up to ~ 2000 for the TE polarization.

The spheres were inserted into a square capillary, several different solutions were pumped through the channel, and the overall spectral shifts and FSRs were measured using Fourier analysis of the WGM spectra. The 3σ shift detection limits in these structures are close to 10^{-5} RIU. The FSR can be used as an alternative measure of the refractive index changes in the capillary. These "sphere-in-a-capillary" devices are promising for true microfluidic biosensing applications, since the Si-QD coatings can be functionalized to detect biomolecules such as biotin and streptavidin [224]. The method is robust and repeatable, and experimentally simple compared to other strategies for the microfluidic integration of microspheres for refractometric or biosensing applications.

6.5 Acknowledgements

We thank NSERC and CSC (File No. 2008605099) for funding this research, and the Veinot group for chemistry help and assistance.

7. Conclusions and outlook

The main objectives of this work were to investigate in detail the WGM mode structure of a fluorescent microsphere with a high-index quantum-dot coating, and to investigate the application of such structures for reactive sensing. The work started with a broad overview of the theory associated with the whispering gallery modes of a sphere, beginning with first priciples and ending with the calculation of the key mode parameters such as the resonance wavelength, Q factor, and refractometric sensitivity. The main loss mechanisms and their influence on the overall Q factor were investigated, as well as the effect of the high-index coating thickness.

Having reviewed the basic theory of the WGMs in a layered microsphere, we next discussed the methods used in this work to fabricate a quantum-dot-coated microsphere. This involved melting a tapered optical fiber and then using a "dip-coating" method to fabricate a layer of fluorescent silicon QDs uniformly over the surface of the sphere. The methods used were elaborated in detail, since the process was not completely trivial and required a fair bit of trial and error to get it to work well.

The main body of the thesis was then composed of a set of papers that investigated the properties of these coated microspheres. Several aspects were investigated, including the basic whispering gallery mode structure, the thermal response of the WGMs, and various refractometric sensing applications. These investigations should produce a fairly complete picture of the properties of QD-coated microspheres. Several interesting experimental features were reported, as well as some of the main challenges and frustrations associated with sensor-type applications (one of the worst difficulties being mechanical drift). Compared to the surface plasmon resonance (SPR)-type sensors, which can often require bulky coupling configurations, the WGM-type sensor can be readily interfaced to a micro-fluidic system. Each of the main results can be summerized briefly here, and we will then finish with a discussion of the future outlook for coated microsphere-type sensors.

Chapter 3 discussed the PL WGM structure of a fluorescent microsphere by comparing it to the "intrinsic" cavity modes obtained via evanescent measurements. The results showed that the fluorescence WGMs were broad single peaks, while the underlying cavity modes were much more complicated. In the "cold" cavity spectrum, the first- and second-radial-order modes appeared and were split into several families of non-degenerate modes, due to a slight eccentricity of the sphere. The fluorescence WGMs represented a broadening of the much high-Q "intrinsic" cavity modes. The broadening was mainly a result of the wide linewidth associated with the individual QDs. The observed behaviour of the fluorescence WGMs at cryogenic temperatures was attributed to spectral diffusion, which alters the QD linewidth.

In the next paper (Chapter 4) we looked at the thermal response of the fluorescence WGMs. The resonant wavelengths shift as a result of local temperature changes, mainly due to the thermo-refractive effect in the glass sphere and the QD coating. These materials have refractive indices that increase with temperature, so any warming causes a mode red-shift. This can be problematic for reactive sensing applications, because thermal fluctuations can cause underlying noise or gradually continuous drifts in the data. Some amount of heating is virtually unavoidable, simply due to absorption of the pump laser. Thus, we aimed to find out whether the effect could be minimized.

A mathematical analysis of the thermal shifts showed that it should be theoretically possible to build a microsphere with near-perfect stability against thermal fluctuations. The basis of the method was to balance the positive thermal-refractive effect of the glass sphere with the negative one of the outside solvent (ideally, water). Theory suggested that this could be achieved for a first-order radial mode with a QD film thickness near 100 nm for a 30 µm-radius-sphere. The basic idea is that the high-index coating on the sphere can be used to control the extent of the field penetration into each of the layers (glass sphere, QD coating, outside medium). If the film could be tailored to the desired thickness, a zero thermal shift should be achievable. We then built a microsphere that was quite near these conditions (admittedly, it was somewhat lucky that the coating method naturally produces film near the ideal thickness). The microsphere showed only very small thermal shifts - in fact they were so small that the detection limit would likely be imposed by other problems such as mechanical drift or the detector shift resolution.

Chapter 5 focused on refractometric sensing experiments in both bulk- and microfluidic environments. The basic fluorescence WGM structure of a QD-coated microsphere was first characterized in terms of the Q factor, FSR, and mode visibility. The microspheres showed excellent fluorescence WGM characteristics including a high visibility ($V > 0.5$) and a Q factor of $\sim 10^3$. In order to test the bulk sensing capability, a single sphere was then inserted into a cuvette containing various solutions of methanol-water mixtures. The results showed that the sphere-in-a-cuvette setup could be used fairly easily for refractometric sensing, although the sphere did tend to drift during the addition or removal of fluid, mainly due to the large volumes involved. Attempts were then made to perform sensing experiments inside a standard round capillary in this chapter, but lensing effects were found to be too severe to obtain well-focused spectra in most cases. Therefore, for the rest of the work a square capillary was used instead. Fluids were pumped through the capillary and the microsphere was operated to produce sensorgram-type data. The sphere sensitivity could be as high as ~ 100 nm/RIU, and for these experiments the detection limit was $\sim 10^{-5}$ RIU.

In Chapter 6 the effect of the QD coating thickness on the sensor performance was investigated. While the Q factors were not much affected by increasing the thickness of the QD film, the overall fluorescence intensity increased considerably. The mode visibility reached values as high as ~ 0.7, indicating a very strong, pronounced WGM structure that was far above the fluorescence background. The refractometric sensitivities were increased by double-coating the microsphere, consistent with the theory developed in Chapter 1 for films below the optimal thickness. Finally, the FSR was found to represent an alternative sensor mechanism, since it also responds to changes in the external medium. Again, however, Fourier methods were needed to resolve the FSR at the picometer scale.

Future work

While this thesis demonstrated several of the basic properties of QD coated microspheres, the door is open for future work. This could start with basic optimization, but some of the main advances in relation to coated fluorescent microspheres will probably be in the area of specific sensing applications. Some of the basic advances I would suggest for future work include:

1. Improve the mechanical stability. A typical sensorgram experiment can currently last several hours, mainly limited by the time required to pump fluids through the capillary channel (this is itself an issue for improvement as discussed below). We found that if the sphere drifts even by one pixel on the CCD (keeping in mind that one is measuring fluorescence WGM shifts on the scale of picometers), one can have artificial shifts develop in the spectrum. Better mechanical stability in the holder, better control over local air movements, and minimization of temperature fluctuations (which can also induce mechanical motion) may help to solve this problem. Self-referencing (i.e., comparing the shift of one mode to that of another one) has also been used to cancel the effects of noise and drift [244, 245]; such strategies could possibly be used in spheres as well.

2. Improve analysis speed. As mentioned above, an experiment can take few hours mainly because of the time required to "settle" into relative mechanical stability and because one has to pump through long tubing lengths. Faster collection

times (e.g., by using shorter tubing lengths and faster pumping rates) should therefore be advantageous. In fact, a complete "packaging solution" of the type shown in Ref [69] could address issues 1 and 2. In that work, a microsphere was mechanically integrated into a single portable unit that featured a microfabricated channel. While this kind of packaging issue was not investigated here, such solutions do exist and could be a promising way to eliminate problems associated with analysis speed and drift.

3. Fabricate smaller microspheres. The size of the microspheres used in this thesis ranged from 30-70 µm. Small spheres are somewhat more difficult to fabricate, however, they have a larger FSR, and can thus accommodate larger shifts. For example, if the mode shifts by half an FSR the Fourier method gets confused (i.e., it cannot distinguish a shift of $\pi + \varphi$ from a shift of $-\pi + \varphi$). Second, smaller spheres have more of the field energy in the outside medium and thus have higher sensitivity.

4. Live-time analysis. Currently, the data are all collected for a given sensorgram run, and then they are analyzed and the sensorgram is produced. One does not know if problems occurred until after the experiment is complete. In future work, one might re-write the analysis software so that it can show results "in situ", point-by-point. Then the experimenter would know immediately in live time how the experiment is going.

5. Biosensing. In this thesis, a basic characterization of the WGMs associated with QD-coated single microspheres was performed. This work hopefully sets the stage for future experiments in which these microspheres will be used for biosensing experiments. This means that the surface of the spheres needs to be functionalized to react with a specific analyte. A considerable amount of literature exists for how to do this, mostly involving silanization of the silica surface [74, 23]. These techniques should be applicable for Si-QD-coated microspheres as well, since the QD coating is itself silica based. This will almost certainly be one of the next steps in our group. This thesis laid the groundwork in terms of how to make highly fluorescent QD-coated microspheres, how to setup a microfluidic-type sensor apparatus, and performed a complete characterization of the relevant mode properties.

Finally, a brief comparison can be made in terms of WGM vs. surface plasmon resonance (SPR) optical sensors. SPR-based methods are probably the most advanced at this stage, and there are commercial devices available [246]. The physics behind SPR sensors has been widely discussed in several review papers [208, 247, 248] and will therefore not be repeated in detail. The basic method generally involves coupling white light to a gold film, on one side of which the analyte fluid will be pumped, and the other side is generally used for delivery of the white light, e.g., via a prism. The advantages of SPR-based sensing methods are: i) low detection limit ([247]), ii) established surface chemistry for bio-molecular recognition, such as amine or pegylation chemistry, iii) the excitation light is not limited to lasers, iv) mobile instruments have already been developed [249].

Obviously SPR-based sensing is far ahead of WGM-based methods. However, WGM sensors have some attractive properties as well. First, they are often inherently micro-fluidic, minimizing the requirement for micro-fabrication which can be necessary for the miniaturization of plasmonic sensors. Second, WGMs can be used to measure changes due to the binding of single particles (i.e., a single virus) [209]. Admittedly, single protein detection has also been demonstrated by localized surface plasmon resonance of individual gold bipyramids [250]. However, a fluidic environment needed to be built and the spectra collection time was over 12 h. Also, only the unbinding of the molecules were detected, because the binding process was too fast for the SPR-sensor to capture. Third, the WGM-type sensors fabricated using only Si and SiO_2 can be easily integrated into CMOS-compatible devices.

As a last word, then, microsphere-based sensing is a rapidly developing field. Researchers are detecting ever smaller shifts, using a variety of methods, and can now detect the binding of single virus [209]. One rapidly expanding area couples SPR technology to WGMs, for example by using gold particles to enhance the WGM field at a desired location, thereby increasing the sensitivity [251]. Another uses radiation forces to “trap” particles in an “optical carousel” around the equator of a sphere [252]. Based on these recent developments, we may be just beginning to see the range of possibilities associated with microsphere-based sensing.

References

[1] J. W. S. Rayleigh, "The problem of the whipering gallery," *Philosophical Magazine*, vol. 20, pp. 1001–1004, 1910.

[2] J. W. S. Rayleigh, "Further applications of bessel's functions of high order to the whispering gallery and allied problems," *Philosophical Magazine*, vol. 27, pp. 100–109, 1914.

[3] J. W. S. Rayleigh, *The Theory of Sound.* New York: Dover, 1945.

[4] G. Mie, "Contributions to the optics of turbid media, particularly of colloidal metal solutions," *Annalen der Physik*, vol. 330(3), p. 377, 1908.

[5] J. J. Thomson, *Notes on recent researches in electricity and magnetism, intended as a sequel to Professor Clerk-Maxwell's 'Treatise on Electricity and Magnetism'.* Oxford, The Clarendon press, 1893.

[6] A. Clebsch, "Über die reflexion an einer kugelfläche," *Journal für die reine und angewandte Mathematik*, vol. 61, pp. 195–262, 1863.

[7] L. Lorenz, *Œuvres scientifiques de L. Lorenz. Revues et annotèes par H. Valentiner*, ch. Sur la lumière réfléchie et réfractée par une sphère (surface) transparente, pp. 403–529. Libraire Lehmann & Stage, Copenhague, 1898.

[8] L. Lorenz, "Lysbevaegelsen i og uden for en af plane lysbolger belyst kugle," *Det Kongelige Danske Videnskabernes Selskabs Skrifter*, vol. 6, pp. 1–62, 1890.

[9] P. Debye, "Der lichtdruck auf kugeln von beliebigem material," *Annalen der Physik*, vol. 30, pp. 57–136, 1909.

[10] H. Horvath, "Gustav mie and the scattering and absorption of light by particles: Historic developments and basics," *Journal of Quantitative Spectroscopy and Radiative Transfer*, vol. 110, no. 11, pp. 787 – 799, 2009. Light Scattering: Mie and More Commemorating 100 years of Mie's 1908 publication.

[11] T. W. Wolfram Hergert, *The Mie Theory Basics and Applications*, vol. 169, ch. Chapter 2: Mie Theory: A Review, pp. 53–71. Springer Series in Optical Sciences, 2012.

[12] C. G. B. Garrett, W. Kaiser, and W. L. Bond, “Stimulated emission into optical whispering modes of spheres,” *Physical Review*, vol. 124, pp. 1807–1809, Dec 1961.

[13] K. Srinivasan, M. Borselli, O. Painter, A. Stintz, and S. Krishna, “Cavity Q, mode volume, and lasing threshold in small diameter AlGaAs microdisks with embedded quantum dots,” *Optics Express*, vol. 14, pp. 1094–1105, Feb 2006.

[14] S. Götzinger, L. de S Menezes, O. Benson, D. V. Talapin, N. Gaponik, H. Weller, A. L. Rogach, and V. Sandoghdar, “Confocal microscopy and spectroscopy of nanocrystals on a high- q microsphere resonator,” *Journal of Optics B: Quantum and Semiclassical Optics*, vol. 6, no. 2, pp. 154–158, 2004.

[15] S. I. Shopova, G. Farca, A. T. Rosenberger, W. M. S. Wickramanayake, and N. A. Kotov, “Microsphere whispering-gallery-mode laser using HgTe quantum dots,” *Applied Physics Letters*, vol. 85, no. 25, pp. 6101–6103, 2004.

[16] P. Bianucci, J. R. Rodriguez, C. M. Clements, J. G. C. Veinot, and A. Meldrum, “Silicon nanocrystal luminescence coupled to whispering gallery modes in optical fibers,” *Journal of Applied Physics*, vol. 105, no. 2, p. 023108, 2009.

[17] V. L. Seguin, “Whispering-gallery mode lasers with doped silica microspheres,” *Optical Materials*, vol. 11, pp. 153–165, 1999.

[18] M. Charlebois, A. Paquet, L. Verret, K. Boissinot, M. Boissinot, M. Bergeron, and C. Allen, “Toward automatic label-free whispering gallery modes biodetection with a quantum dot-coated microsphere population,” *Nanoscale Research Letters*, vol. 5, no. 3, pp. 524–532, 2010.

[19] H. A. Huckabay and R. C. Dunn, “Whispering gallery mode imaging for the multiplexed detection of biomarkers,” *Sensors and Actuators B: Chemical*, vol. 160, no. 1, pp. 1262–1267, 2011.

[20] I. White, H. Zhu, J. Suter, X. Fan, and M. Zourob, “Label-free detection with the liquid core optical ring resonator sensing platform,” in *Biosensors and Biodetection* (A. Rasooly and K. Herold, eds.), vol. 503 of *Methods in Molecular Biology*, pp. 139–165, Humana Press, 2009.

[21] S. Soria, S. Berneschi, M. Brenci, F. Cosi, G. Nunzi Conti, S. Pelli, and G. C. Righini, “Optical microspherical resonators for biomedical sensing,” *Sensors*, vol. 11, no. 1, pp. 785–805, 2011.

[22] H. Zhu, I. M. White, J. D. Suter, and X. Fan, “Phage-based label-free biomolecule detection in an opto-fluidic ring resonator,” *Biosensors and Bioelectronics*, vol. 24, no. 3, pp. 461–466, 2008.

[23] F. Vollmer, D. Braun, A. Libchaber, M. Khoshsima, I. Teraoka, and S. Arnold, “Protein detection by optical shift of a resonant microcavity,” *Applied Physics Letters*, vol. 80, no. 21, pp. 4057–4059, 2002.

[24] S. Arnold, M. Khoshsima, I. Teraoka, S. Holler, and F. Vollmer, “Shift of whispering-gallery modes in microspheres by protein adsorption,” *Optics Letters*, vol. 28, pp. 272–274, Feb 2003.

[25] L. A. Krivitsky, J. J. Wang, Z. Wang, and B. Luk’yanchuk, “Locomotion of microspheres for super-resolution imaging,” *Scientific Reports*, vol. 3, DEC 16 2013.

[26] D. O’Shea, C. Junge, J. Volz, and A. Rauschenbeutel, “Fiber-optical switch controlled by a single atom,” *Physical Review Letters*, vol. 111, p. 193601, Nov 2013.

[27] I. Teraoka and S. Arnold, “Resonance shifts of counterpropagating whispering-gallery modes: degenerate perturbation theory and application to resonator sensors with axial symmetry,” *Journal of the Optical Society of America B*, vol. 26, pp. 1321–1329, Jul 2009.

[28] D. F. McCammon and S. T. McDaniel, “Surface reflection: On the convergence of a series solution to a modified helmholtz integral equation and the validity of the kirchhoff approximation,” *The Journal of the Acoustical Society of America*, vol. 79, no. 1, pp. 64–70, 1986.

[29] B. V. Budaev and D. B. Bogy, “Novel solutions of the helmholtz equation and their application to diffraction,” *Proceedings: Mathematical, Physical and Engineering Sciences*, vol. 463, pp. 1005–1027, Apr. 2007.

[30] L. Qiu, M. V. de Hoop, and A. S. Barreto, “Modelling of time-harmonic seismic data with the helmholtz equation and scattering series,” *Society of Exploration Geophysicists*, pp. 3103–3109, 2010.

[31] J.-M. Jin, *Theory and Computation of Electromagnetic Fields.* Wiley-IEEE Press, 1 ed., 2010.

[32] B. R. Johnson, “Theory of morphology-dependent resonances: shape resonances and width formulas,” *Journal of the Optical Society of America A*, vol. 10, pp. 343–352, Feb 1993.

[33] M. L. Gorodetsky, A. A. Savchenkov, and V. S. Ilchenko, “Ultimate Q of optical microsphere resonators,” *Optics Letters*, vol. 21, pp. 453–455, Apr 1996.

[34] M. Andachi, T. Nakayama, M. Kawasaki, S. Kurokawa, and H.-P. Loock, “Fiber-optic ring-down spectroscopy using a tunable picosecond gain-switched diode laser,” *Applied Physics B*, vol. 88, no. 1, pp. 131–135, 2007.

[35] “http://web.mit.edu/8.02t/www/materials/StudyGuide/guide12.pdf.”

[36] I. Agha, J. Sharping, M. Foster, and A. Gaeta, “Optimal sizes of silica microspheres for linear and nonlinear optical interactions,” *Applied Physics B*, vol. 83, no. 2, pp. 303–309, 2006.

[37] W. Kim, c. K. Özdemir, J. Zhu, and L. Yang, “Observation and characterization of mode splitting in microsphere resonators in aquatic environment,” *Applied Physics Letters*, vol. 98, no. 14, p. 141106, 2011.

[38] V. N. Astratov, S. Yang, S. Lam, B. D. Jones, D. Sanvitto, D. M. Whittaker, A. M. Fox, M. S. Skolnick, A. Tahraoui, P. W. Fry, and M. Hopkinson, “Whispering gallery resonances in semiconductor micropillars,” *Applied Physics Letters*, vol. 91, no. 7, p. 071115, 2007.

[39] O. Painter, R. K. Lee, A. Scherer, A. Yariv, J. D. O’Brien, P. D. Dapkus, and I. Kim, “Two-dimensional photonic band-gap defect mode laser,” *Science*, vol. 284, no. 5421, pp. 1819–1821, 1999.

[40] S. Götzinger, D. Press, S. Reitzenstein, K. Hofmann, A. Löffler, M. Kamp, A. Forchel, and Y. Yamamoto, “Strong coupling of single quantum dots to micropillars,” *Proceedings of SPIE*, vol. 6593, pp. 65932E–65932E–8, 2007.

[41] Y.-Z. Yan, C.-L. Zou, S.-B. Yan, F.-W. Sun, Z. Ji, J. Liu, Y.-G. Zhang, L. Wang, C.-Y. Xue, W.-D. Zhang, Z.-F. Han, and J.-J. Xiong, “Packaged silica microsphere-taper coupling system for robust thermal sensing application,” *OPTICS EXPRESS*, vol. 19, pp. 5753–5759, MAR 28 2011.

[42] M. Fox, *Quantum Optics : An Introduction.* Oxford Master Series in Physics, Oxford University Press, 2006.

[43] H. Mabuchi and A. C. Doherty, “Cavity quantum electrodynamics: Coherence in context,” *Science*, vol. 298, no. 5597, pp. 1372–1377, 2002.

[44] E. M. Purcell, “Spontaneous emission probabilities at radio frequencies,” *Physical Review*, vol. 69, p. 681, 1946.

[45] A. Meldrum, P. Bianucci, and F. Marsiglio, “Modification of ensemble emission rates and luminescence spectra for inhomogeneously broadened distributions of quantum dots coupled to optical microcavities,” *Optics Express*, vol. 18, pp. 10230–10246, May 2010.

[46] G. S. Solomon, M. Pelton, and Y. Yamamoto, “Single-mode spontaneous emission from a single quantum dot in a three-dimensional microcavity,” *Physical Review Letters*, vol. 86, pp. 3903–3906, Apr 2001.

[47] J. Vučković, D. Fattal, C. Santori, G. S. Solomon, and Y. Yamamoto, “Enhanced single-photon emission from a quantum dot in a micropost microcavity,” *Applied Physics Letters*, vol. 82, no. 21, pp. 3596–3598, 2003.

[48] J. Gérard, B. Legrand, B. Gayral, E. Costard, B. Sermage, R. Kuszelewicz, D. Barrier, V. Thierry-Mieg, T. Rivera, and J. Marzin, “InAs quantum boxes in GaAs/AlAs pillar microcavities: from spectroscopic investigations to spontaneous emission control,” *Physica E: Low-dimensional Systems and Nanostructures*, vol. 2, no. 1-4, pp. 804–808, 1998.

[49] B. Gayral, J. M. Gérard, A. Lemaître, C. Dupuis, L. Manin, and J. L. Pelouard, “High-Q wet-etched gaas microdisks containing inas quantum boxes,” *Applied Physics Letters*, vol. 75, no. 13, pp. 1908–1910, 1999.

[50] O. Benson, S. Götzinger, A. Mazzei, G. Zumofen, V. Sandoghdar, and L. S. Menezes, “Nanophotonics with microsphere resonators,” in *VLSI Micro- and Nanophotonics*, pp. 5–1–5–28, CRC Press, Sept. 2010.

[51] V. N. Astratov, “Fundamentals and Applications of Microsphere Resonator Circuits,” in *Photonic Microresonator Research and Applications* (Chremmos, I and Schwelb, O and Uzunoglu, N, ed.), vol. 156 of *Springer Series in Optical Sciences*, pp. 423–457, Springer, 2010.

[52] A. Kavokin, *Microcavities.* Series on semiconductor science and technology: 16, Oxford : Oxford University Press, 2007.

[53] P. Bianucci, X. Wang, J. G. Veinot, and A. Meldrum, "Silicon nanocrystals on bottle resonators: Mode structure, loss mechanisms and emission dynamics," *Optics Express*, vol. 18, pp. 8466–8481, Apr 2010.

[54] F. Payne and J. Lacey, "A theoretical analysis of scattering loss from planar optical waveguides," *Optical and Quantum Electronics*, vol. 26, no. 10, pp. 977–986, 1994.

[55] R. E. Smith, L. A. Molter, and M. Dutta, "Evaluation of refractive-index approximations used for mode determination in multiple quantum-well slab waveguides," *IEEE Journal of Quantum Electronics*, vol. 27, pp. 1119–1122, MAY 1991.

[56] N. Lin, L. Jiang, S. Wang, H. Xiao, Y. Lu, and H.-L. Tsai, "Design and optimization of liquid core optical ring resonator for refractive index sensing," *Applied Optics*, vol. 50, pp. 3615–3621, Jul 2011.

[57] "http://www.crystran.co.uk/optical-materials/silica-glass-sio2."

[58] R. D. Kekatpure and M. L. Brongersma, "Fundamental photophysics and optical loss processes in Si-nanocrystal-doped microdisk resonators," *Physical Review A*, vol. 78, p. 023829, Aug 2008.

[59] N. Daldosso, M. Melchiorri, L. Pavesi, G. Pucker, F. Gourbilleau, S. Chausserie, A. Belarouci, X. Portier, and C. Dufour, "Optical losses and absorption cross-section of silicon nanocrystals," *Journal of Luminescence*, vol. 121, pp. 344–348, Dec. 2006.

[60] J. D. Jackson, *Classical Electrodynamics.* Wiley, New York, NY, 1998.

[61] J. R. Rodriguez, J. G. C. Veinot, P. Bianucci, and A. Meldrum, "Whispering gallery modes in hollow cylindrical microcavities containing silicon nanocrystals," *Applied Physics Letters*, vol. 92, no. 13, p. 131119, 2008.

[62] "http://www.lifetechnologies.com/order/catalog/en/US/adirect/lt?cmd=IVGNcatDisplayCategory&catKey=89001."

[63] F. Lissillour, D. Messager, G. Stéphan, and P. Féron, "Whispering-gallery-mode laser at 1.56 μm excited by a fiber taper," *Optics Letters*, vol. 26, pp. 1051–1053, Jul 2001.

[64] C.-H. Dong, Y.-F. Xiao, Z.-F. Han, G.-C. Guo, X. Jiang, L. Tong, C. Gu, and H. Ming, "Low-threshold microlaser in Er : Yb phosphate glass coated microsphere," *Photonics Technology Letters, IEEE*, vol. 20, pp. 342–344, March 2008.

[65] M. Cai, O. Painter, K. J. Vahala, and P. C. Sercel, "Fiber-coupled microsphere laser," *Optics Letters*, vol. 25, pp. 1430–1432, Oct 2000.

[66] V. Sandoghdar, F. Treussart, J. Hare, V. Lefèvre-Seguin, J.-M. Raimond, and S. Haroche, "Very low threshold whispering-gallery-mode microsphere laser," *Physical Review A*, vol. 54, pp. R1777–R1780, SEP 1996.

[67] A. Tewary, M. J. F. Digonnet, J.-Y. Sung, J. H. Shin, and M. Brongersma, "Silicon-nanocrystal-coated silica microsphere thermooptical switch," *Selected Topics in Quantum Electronics, IEEE Journal of*, vol. 12, no. 6, pp. 1476–1479, 2006.

[68] H. C. Tapalian, J. P. Laine, and P. Lane, "Thermooptical switches using coated microsphere resonators," *Photonics Technology Letters, IEEE*, vol. 14, no. 8, pp. 1118–1120, 2002.

[69] S. L. Westcott, J. Zhang, R. K. Shelton, N. M. K. Bruce, S. Gupta, S. L. Keen, J. W. Tillman, L. B. Wald, B. N. Strecker, A. Rosenberger, R. R. Davidson, W. Chen, K. G. Donovan, and J. V. Hryniewicz, "Broadband optical absorbance spectroscopy using a whispering gallery mode microsphere resonator," *Review of Scientific Instruments*, vol. 79, no. 3, pp. 033106–033106–9, 2008.

[70] N. Zammatteo, L. Jeanmart, S. Hamels, S. Courtois, P. Louette, L. Hevesi, and J. Remacle, "Comparison between different strategies of covalent attachment of DNA to glass surfaces to build DNA microarrays," *Analytical Biochemistry*, vol. 280, no. 1, pp. 143–150, 2000.

[71] R. M. Pasternack, S. Rivillon Amy, and Y. J. Chabal, "Attachment of 3-(aminopropyl)triethoxysilane on silicon oxide surfaces: Dependence on solution temperature," *Langmuir*, vol. 24, no. 22, pp. 12963–12971, 2008. PMID: 18942864.

[72] N. Aissaoui, L. Bergaoui, J. Landoulsi, J.-F. Lambert, and S. Boujday, "Silane layers on silicon surfaces: Mechanism of interaction, stability, and influence on protein adsorption," *Langmuir*, vol. 28, no. 1, pp. 656–665, 2012.

[73] S. Tsoi, E. Fok, J. C. Sit, and J. G. C. Veinot, "Superhydrophobic, high surface area, 3-D SiO_2 nanostructures through siloxane-based surface functionalization," *Langmuir*, vol. 20, no. 24, pp. 10771–10774, 2004. PMID: 15544415.

[74] B. Kranz, J. Bürck, M. Franzreb, R. Köster, and A. S. Ulrich, "Circular dichroism analysis of penicillin G acylase covalently immobilized on silica nanoparticles," *Journal of Colloid and Interface Science*, vol. 316, no. 2, pp. 413–419, 2007.

[75] I. Teraoka, S. Arnold, and F. Vollmer, "Perturbation approach to resonance shifts of whispering-gallery modes in a dielectric microsphere as a probe of a surrounding medium," *Journal of the Optical Society of America B*, vol. 20, pp. 1937–1946, Sep 2003.

[76] I. Teraoka and S. Arnold, "Theory of resonance shifts in TE and TM whispering gallery modes by nonradial perturbations for sensing applications," *Journal of the Optical Society of America B*, vol. 23, pp. 1381–1389, Jul 2006.

[77] F. Vollmer and S. Arnold, "Optical microcavities: single virus detection and nanoparticle trapping," *Proceedings of SPIE*, vol. 7397, pp. 739702–1–739702–9, 2009.

[78] H.-C. Ren, F. Vollmer, S. Arnold, and A. Libchaber, "High-Q microsphere biosensor - analysis for adsorption of rodlike bacteria," *Optics Express*, vol. 15, pp. 17410–17423, Dec 2007.

[79] F. L. Pedrotti, L. S. Pedrotti, and L. M. Pedrotti, *Introduction to Optics (3rd Edition)*. Pearson Prentice Hall, 3 ed., 2006.

[80] B. E. Little, J.-P. Laine, H. A. Haus, and L. Fellow, "Analytic theory of coupling from tapered fibers and half-blocks into microsphere resonators," *Journal of Lightwave Technology*, vol. 17, p. 704, Apr 1999.

[81] J. M. Ward, A. Maimaiti, V. H. Le, and S. N. Chormaic, "Optical Micro- and Nanofiber Pulling Rig," *ArXiv e-prints*, Feb. 2014.

[82] M.-C. M. Lee and M. C. Wu, "Tunable coupling regimes of silicon microdisk resonators using mems actuators," *Optics Express*, vol. 14, pp. 4703–4712, May 2006.

[83] L. Pavesi, L. Dal Negro, C. Mazzoleni, G. Franzò, and F. Priolo, "Optical gain in silicon nanocrystals," *Nature*, pp. 440–444, 2000.

[84] G. Schmid, ed., *Nanoparticles From Theory to Application Second, Completely Revised and Updated Edition.* WILEY-VCH Verlag, 2010.

[85] S. V. Gaponenko, *Optical properties of semiconductor nanocrystals*, vol. 23. Cambridge university press, 1998.

[86] A. P. Alivisatos, W. Gu, and C. Larabell, "Quantum dots as cellular probes," *Annual Review of Biomedical Engineering*, vol. 7, no. 1, pp. 55–76, 2005. PMID: 16004566.

[87] X. Ma and S. John, "Switching dynamics and ultrafast inversion control of quantum dots for on-chip optical information processing," *Physical Review A*, vol. 80, p. 063810, Dec 2009.

[88] M. Nogami, K. Nagaska, and E. Kato, "Preparation of small-particle-size, semiconductor cds-doped silica glasses by the sol-gel process," *Journal of the American Ceramic Society*, vol. 73, no. 7, pp. 2097–2099, 1990.

[89] F. T. Quinlan, J. Kuther, W. Tremel, W. Knoll, S. Risbud, and P. Stroeve, "Reverse micelle synthesis and characterization of znse nanoparticles," *Langmuir*, vol. 16, no. 8, pp. 4049–4051, 2000.

[90] S. L. Cumberland, K. M. Hanif, A. Javier, G. A. Khitrov, G. F. Strouse, S. M. Woessner, and C. S. Yun, "Inorganic clusters as single-source precursors for preparation of cdse, znse, and cdse/zns nanomaterials," *Chemistry of Materials*, vol. 14, no. 4, pp. 1576–1584, 2002.

[91] "http://farside.ph.utexas.edu/teaching/qmech/Quantum/node81.html."

[92] D. Kovalev, H. Heckler, M. Ben-Chorin, G. Polisski, M. Schwartzkopff, and F. Koch, "Breakdown of the k-conservation rule in si nanocrystals," *Physical Review Letters*, vol. 81, pp. 2803–2806, Sep 1998.

[93] V. Burdov, "Dependence of the optical gap of Si quantum dots on the dot size," *Semiconductors*, vol. 36, no. 10, pp. 1154–1158, 2002.

[94] V. A. Belyakov, V. A. Burdov, R. Lockwood, and A. Meldrum, "Silicon nanocrystals: Fundamental theory and implications for stimulated emission," *Advances in Optical Technologies*, vol. 2008, p. 32, 2008.

[95] S. Öğüt, J. R. Chelikowsky, and S. G. Louie, "Quantum confinement and optical gaps in Si nanocrystals," *Physical Review Letters*, vol. 79, pp. 1770–1773, Sep 1997.

[96] C. Delerue, G. Allan, and M. Lannoo, "Theoretical aspects of the luminescence of porous silicon," *Physical Review B*, vol. 48, pp. 11024–11036, Oct 1993.

[97] N. A. Hill and K. B. Whaley, "Size dependence of excitons in silicon nanocrystals," *Physical Review Letters*, vol. 75, pp. 1130–1133, Aug 1995.

[98] A. Mimura, M. Fujii, S. Hayashi, D. Kovalev, and F. Koch, "Photoluminescence and free-electron absorption in heavily phosphorus-doped Si nanocrystals," *Physical Review B*, vol. 62, pp. 12625–12627, Nov 2000.

[99] T. van Buuren, L. N. Dinh, L. L. Chase, W. J. Siekhaus, and L. J. Terminello, "Changes in the electronic properties of Si nanocrystals as a function of particle size," *Physical Review Letters*, vol. 80, pp. 3803–3806, Apr 1998.

[100] S. Takeoka, M. Fujii, and S. Hayashi, "Size-dependent photoluminescence from surface-oxidized Si nanocrystals in a weak confinement regime," *Physical Review B*, vol. 62, pp. 16820–16825, Dec 2000.

[101] S. Guha, S. B. Qadri, R. G. Musket, M. A. Wall, and T. Shimizu-Iwayama, "Characterization of Si nanocrystals grown by annealing SiO_2 films with uniform concentrations of implanted Si," *Journal of Applied Physics*, vol. 88, no. 7, pp. 3954–3961, 2000.

[102] G. Ledoux, O. Guillois, D. Porterat, C. Reynaud, F. Huisken, B. Kohn, and V. Paillard, "Photoluminescence properties of silicon nanocrystals as a function of their size," *Physical Review B*, vol. 62, pp. 15942–15951, Dec 2000.

[103] A. Hryciw, A. Meldrum, K. Buchanan, and C. White, "Effects of particle size and excitation spectrum on the photoluminescence of silicon nanocrystals formed by ion implantation," *Nuclear Instruments and Methods in Physics Research Section B: Beam Interactions with Materials and Atoms*, vol. 222, pp. 469–476, 2004.

[104] J. A. McGuire, J. Joo, J. M. Pietryga, R. D. Schaller, and V. I. Klimov, "New aspects of carrier multiplication in semiconductor nanocrystals," *Accounts of Chemical Research*, vol. 41, no. 12, pp. 1810–1819, 2008.

[105] S. M. Prokes, “Light emission in thermally oxidized porous silicon: Evidence for oxide-related luminescence,” *Applied Physics Letters*, vol. 62, no. 25, pp. 3244–3246, 1993.

[106] T. K. Sham, D. T. Jiang, I. Coulthard, J. W. Lorimer, X. H. Feng, K. H. Tan, S. P. Frigo, R. A. Rosenberg, D. C. Houghton, and B. Bryskiewicz, “Origin of luminescence from porous silicon deduced by synchrotron-light-induced optical luminescence,” *Nature*, vol. 363, pp. 331–334, May 1993.

[107] A. J. Kontkiewicz, A. M. Kontkiewicz, J. Siejka, S. Sen, G. Nowak, A. Hoff, P. Sakthivel, K. Ahmed, P. Mukherjee, S. Witanachchi, and J. Lagowski, “Evidence that blue luminescence of oxidized porous silicon originates from sio2,” *Applied Physics Letters*, vol. 65, pp. 1436–1438, Sep 1994.

[108] Y. Kanemitsu, T. Ogawa, K. Shiraishi, and K. Takeda, “Visible photoluminescence from oxidized Si nanometer-sized spheres: Exciton confinement on a spherical shell,” *Physical Review B*, vol. 48, pp. 4883–4886, Aug 1993.

[109] M. V. Wolkin, J. Jorne, P. M. Fauchet, G. Allan, and C. Delerue, “Electronic states and luminescence in porous silicon quantum dots: The role of oxygen,” *Physical Review Letters*, vol. 82, pp. 197–200, Jan 1999.

[110] F. Zhou and J. D. Head, “Role of Si=O in the photoluminescence of porous silicon,” *The Journal of Physical Chemistry B*, vol. 104, no. 43, pp. 9981–9986, 2000.

[111] B. Garrido, M. López, O. González, A. Pérez-Rodríguez, J. R. Morante, and C. Bonafos, “Correlation between structural and optical properties of Si nanocrystals embedded in SiO_2: The mechanism of visible light emission,” *Applied Physics Letters*, vol. 77, no. 20, pp. 3143–3145, 2000.

[112] M. J. Sailor and E. J. Lee, “Surface chemistry of luminescent silicon nanocrystallites,” *Advanced Materials*, vol. 9, no. 10, pp. 783–793, 1997.

[113] R. Lockwood, J. G. C. Veinot, and A. Meldrum, “Sensing Water and Alcohol Vapors with Freestanding Silicon Quantum Dots,” *Sensor Letters*, vol. 11, pp. 1535–1540, Aug. 2013.

[114] I. Vasiliev, J. R. Chelikowsky, and R. M. Martin, “Surface oxidation effects on the optical properties of silicon nanocrystals,” *Physical Review B*, vol. 65, p. 121302, Mar 2002.

[115] Y. J. Chabal, K. Raghavachari, X. Zhang, and E. Garfunkel, “Silanone (Si=O) on Si (100): intermediate for initial silicon oxidation,” *Physical Review B*, vol. 66, p. 161315, Oct 2002.

[116] S. Kuai and A. Meldrum, “High-speed color-switching silicon leds,” *Advanced Materials*, vol. 20, no. 20, pp. 3844–3847, 2008.

[117] D. Jurbergs, E. Rogojina, L. Mangolini, and U. Kortshagen, “Silicon nanocrystals with ensemble quantum yields exceeding 60%,” *Applied Physics Letters*, vol. 88, no. 23, p. 233116, 2006.

[118] M. C. A. Nidhal Mousa Abdul-Ameer, “Direct Optical Energy Gap in Amorphous Silicon Quantum Dots,” *Journal of Modern Physics*, vol. 2, pp. 1530–1537, 2011.

[119] R. Lockwood and A. Meldrum, “Luminescence simulations of ensembles of silicon nanocrystals,” *physica status solidi (a)*, vol. 206, no. 5, pp. 965–968, 2009.

[120] K. A. Littau, P. J. Szajowski, A. J. Muller, A. R. Kortan, and L. E. Brus, “A luminescent silicon nanocrystal colloid via a high-temperature aerosol reaction,” *The Journal of Physical Chemistry*, vol. 97, no. 6, pp. 1224–1230, 1993.

[121] J. P. Wilcoxon, G. A. Samara, and P. N. Provencio, “Optical and electronic properties of si nanoclusters synthesized in inverse micelles,” *Physical Review B*, vol. 60, pp. 2704–2714, Jul 1999.

[122] J. D. Holmes, K. J. Ziegler, R. C. Doty, L. E. Pell, K. P. Johnston, and B. A. Korgel, “Highly luminescent silicon nanocrystals with discrete optical transitions,” *Journal of the American Chemical Society*, vol. 123, no. 16, pp. 3743–3748, 2001.

[123] R. M. Sankaran, D. Holunga, R. C. Flagan, and K. P. Giapis, “Synthesis of blue luminescent si nanoparticles using atmospheric-pressure microdischarges,” *Nano Letters*, vol. 5, no. 3, pp. 537–541, 2005.

[124] Y. Zhong, F. Peng, F. Bao, S. Wang, X. Ji, L. Yang, Y. Su, S.-T. Lee, and Y. He, “Large-scale aqueous synthesis of fluorescent and biocompatible silicon nanoparticles and their use as highly photostable biological probes,” *Journal of the American Chemical Society*, vol. 135, no. 22, pp. 8350–8356, 2013.

[125] H. Jang, L. E. Pell, B. A. Korgel, and D. S. English, “Photoluminescence quenching of silicon nanoparticles in phospholipid vesicle bilayers,” *Journal of Photochemistry and Photobiology A: Chemistry*, vol. 158, pp. 111–117, 2003.

[126] J. Liu, F. Erogbogbo, K.-T. Yong, L. Ye, J. Liu, R. Hu, H. Chen, Y. Hu, Y. Yang, J. Yang, I. Roy, N. A. Karker, M. T. Swihart, and P. N. Prasad, “Assessing clinical prospects of silicon quantum dots: Studies in mice and monkeys,” *ACS Nano*, vol. 7, no. 8, pp. 7303–7310, 2013.

[127] J. Salonen, A. M. Kaukonen, J. Hirvonen, and V.-P. Lehto, “Mesoporous silicon in drug delivery applications,” *Journal of Pharmaceutical Sciences*, vol. 97, no. 2, pp. 632–653, 2008.

[128] J. H. Warner, A. Hoshino, K. Yamamoto, and R. D. Tilley, “Water-soluble photoluminescent silicon quantum dots,” *Angewandte Chemie*, vol. 117, no. 29, pp. 4626–4630, 2005.

[129] A. Fiory and N. Ravindra, “Light emission from silicon: Some perspectives and applications,” *Journal of Electronic Materials*, vol. 32, no. 10, pp. 1043–1051, 2003.

[130] I. Teraoka and S. Arnold, “Enhancing the sensitivity of a whispering-gallery mode microsphere sensor by a high-refractive-index surface layer,” *Journal of the Optical Society of America B*, vol. 23, pp. 1434–1441, Jul 2006.

[131] I. Teraoka and S. Arnold, “Whispering-gallery modes in a microsphere coated with a high-refractive index layer: polarization-dependent sensitivity enhancement of the resonance-shift sensor and te-tm resonance matching,” *Journal of the Optical Society of America B*, vol. 24, pp. 653–659, Mar 2007.

[132] C. P. K. Manchee, V. Zamora, J. W. Silverstone, J. G. C. Veinot, and A. Meldrum, “Refractometric sensing with fluorescent-core microcapillaries,” *Optics Express*, vol. 19, pp. 21540–21551, Oct 2011.

[133] C. M. Hessel, M. A. Summers, A. Meldrum, M. Malac, and J. G. C. Veinot, “Direct patterning, conformal coating, and erbium doping of luminescent nc-Si/SiO_2 thin films from solution processable hydrogen silsesquioxane,” *Advanced Materials*, vol. 19, no. 21, pp. 3513–3516, 2007.

[134] M. A. Brook, *Silicon in Organic, Organometallic and Polymer Chemistry.* John Wiley & Sons, New York, 2000.

[135] C. M. Hessel, E. J. Henderson, and J. G. C. Veinot, "Hydrogen silsesquioxane: A molecular precursor for nanocrystalline Si-SiO_2 composites and freestanding hydride-surface-terminated silicon nanoparticles," *Chemistry of Materials*, vol. 18, no. 26, pp. 6139–6146, 2006.

[136] S. P. Withrow, C. W. White, A. Meldrum, J. D. Budai, D. M. Hembree, and J. C. Barbour, "Effects of hydrogen in the annealing environment on photoluminescence from Si nanoparticles in SiO_2," *Journal of Applied Physics*, vol. 86, no. 1, pp. 396–401, 1999.

[137] A. Francois and M. Himmelhaus, "Optical sensors based on whispering gallery modes in fluorescent microbeads: Size dependence and influence of substrate," *Sensors*, vol. 9, no. 9, pp. 6836–6852, 2009.

[138] S. Pang, R. E. Beckham, and K. E. Meissner, "Quantum dot-embedded microspheres for remote refractive index sensing," *Applied Physics Letters*, vol. 92, no. 22, p. 221108, 2008.

[139] H. Beier, G. Coté, and K. Meissner, "Whispering gallery mode biosensors consisting of quantum dot-embedded microspheres," *Annals of Biomedical Engineering*, vol. 37, no. 10, pp. 1974–1983, 2009.

[140] Q. Ma, T. Rossmann, and Z. Guo, "Whispering-gallery mode silica microsensors for cryogenic to room temperature measurement," *Measurement Science and Technology*, vol. 21, no. 2, p. 025310, 2010.

[141] J. Silverstone, S. McFarlane, C. Manchee, and A. Meldrum, "Ultimate resolution for refractometric sensing with whispering gallery mode microcavities," *Optics Express*, vol. 20, pp. 8284–8295, Apr 2012.

[142] C. Santori, D. Fattal, J. Vučković, G. S. Solomon, and Y. Yamamoto, "Indistinguishable photons from a single-photon device," *Nature*, vol. 419, pp. 594–597, 2002.

[143] A. Kiraz, M. Atatüre, and A. Imamoğlu, "Quantum-dot single-photon sources: Prospects for applications in linear optics quantum-information processing," *Physical Review A*, vol. 69, p. 032305, Mar 2004.

[144] A. Dousse, J. Suffczyński, A. Beveratos, O. Krebs, A. Lemaître, I. Sagnes, J. Bloch, P. Voisin, and P. Senellart, "Ultrabright source of entangled photon pairs," *Nature*, vol. 466, pp. 217–220, 2010.

[145] T. D. Ladd and Y. Yamamoto, “Simple quantum logic gate with quantum dot cavity qed systems,” *Physical Review B*, vol. 84, p. 235307, Dec 2011.

[146] E. Elena del Valle, S. Zippilli, F. P. Laussy, A. Gonzalez-Tudela, G. Morigi, and C. Tejedor, “Two-photon lasing by a single quantum dot in a high-Q microcavity,” *Physical Review B*, vol. 81, p. 035302, Jan 2010.

[147] F. Albert, T. Braun, T. Heindel, C. Schneider, S. Reitzenstein, S. Hofling, L. Worschech, and A. Forchel, “Whispering gallery mode lasing in electrically driven quantum dot micropillars,” *Applied Physics Letters*, vol. 97, no. 10, p. 101108, 2010.

[148] G. Xing, Y. Liao, X. Wu, S. Chakrabortty, X. Liu, E. K. L. Yeow, Y. Chan, and T. C. Sum, “Ultralow-threshold two-photon pumped amplified spontaneous emission and lasing from seeded CdSe/CdS nanorod heterostructures,” *ACS Nano*, vol. 6, no. 12, pp. 10835–10844, 2012.

[149] K. T. Posani, V. Tripathi, S. Annamalai, N. R. Weisse-Bernstein, S. Krishna, R. Perahia, O. Crisafulli, and O. J. Painter, “Nanoscale quantum dot infrared sensors with photonic crystal cavity,” *Applied Physics Letters*, vol. 88, no. 15, p. 151104, 2006.

[150] A. Francois and M. Himmelhaus, “Whispering gallery mode biosensor operated in the stimulated emission regime,” *Applied Physics Letters*, vol. 94, no. 3, p. 031101, 2009.

[151] H. T. Beier, G. L. Coté, and K. E. Meissner, “Modeling whispering gallery modes in quantum dot embedded polystyrene microspheres,” *Journal of the Optical Society of America B*, vol. 27, pp. 536–543, Mar 2010.

[152] H. Zhu, J. D. Suter, I. M. White, and X. Fan, “Aptamer based microsphere biosensor for thrombin detection,” *Sensors*, vol. 6, no. 8, pp. 785–795, 2006.

[153] Y. Zhi, T. Thiessen, and A. Meldrum, “Silicon quantum dot coated microspheres for microfluidic refractive index sensing,” *Journal of the Optical Society of America B*, vol. 30, pp. 51–56, Jan 2013.

[154] T. Yu, Y.-Q. Ji, A.-D. Zhu, H.-F. Wang, and S. Zhang, “Robust teleportation and multipartite entanglement analyzers via quantum-dot spins in weak-coupling cavity quantum electrodynamics regime,” *Journal of the Optical Society of America B Optical Physics*, vol. 29, pp. 2029–2034, Aug. 2012.

[155] B. Gayral and J. M. Gerard, “Photoluminescence experiment on quantum dots embedded in a large purcell-factor microcavity,” *Physical Review B*, vol. 78, p. 235306, Dec 2008.

[156] A. Pitanti, M. Ghulinyan, D. Navarro-Urrios, G. Pucker, and L. Pavesi, “Probing the spontaneous emission dynamics in si-nanocrystals-based microdisk resonators,” *Physical Review Letters*, vol. 104, p. 103901, Mar 2010.

[157] M. D. Barnes, W. B. Whitten, S. Arnold, and J. M. Ramsey, “Homogeneous linewidths of rhodamine 6G at room temperature from cavity-enhanced spontaneous emission rates,” *The Journal of Chemical Physics*, vol. 97, no. 10, pp. 7842–7845, 1992.

[158] Y. Zhi, C. Manchee, J. Silverstone, Z. Zhang, and A. Meldrum, “Refractometric sensing with silicon quantum dots coupled to a microsphere,” *Plasmonics*, vol. 8, no. 1, pp. 71–78, 2013.

[159] P. Bianucci, Y. Zhi, F. Marsiglio, J. Silverstone, and A. Meldrum, “Microcavity effects in ensembles of silicon quantum dots coupled to high-q resonators,” *physica status solidi (a)*, vol. 208, no. 3, pp. 639–645, 2011.

[160] “http://www.wolfram.com..”

[161] G. Chen, S. C. Hill, M. M. Mazumder, Y. R. Chemla, A. Serpengüzel, and R. K. Chang, “Wavelength variation of laser emission along the entire rim of slightly deformed microdroplets,” *Optics Letters*, vol. 18, pp. 1993–1995, Dec 1993.

[162] G. Lin, B. Qian, F. Oručević, Y. Candela, J.-B. Jager, Z. Cai, V. Lefèvre-Seguin, and J. Hare, “Excitation mapping of whispering gallery modes in silica microcavities,” *Optics Letters*, vol. 35, pp. 583–585, Feb 2010.

[163] J. Valenta, R. Juhasz, and J. Linnros, “Photoluminescence spectroscopy of single silicon quantum dots,” *Applied Physics Letters*, vol. 80, no. 6, pp. 1070–1072, 2002.

[164] I. Sychugov, R. Juhasz, J. Valenta, and J. Linnros, “Narrow luminescence linewidth of a silicon quantum dot,” *Physical Review Letters*, vol. 94, p. 087405, Mar 2005.

[165] J. Martin, F. Cichos, and C. von Borczyskowski, “Spectral diffusion of quasi localized excitons in single silicon nanocrystals,” *Journal of Luminescence*, vol. 132, no. 8, pp. 2161–2165, 2012.

[166] S. A. Empedocles and M. G. Bawendi, "Influence of spectral diffusion on the line shapes of single cdse nanocrystallite quantum dots," *The Journal of Physical Chemistry B*, vol. 103, no. 11, pp. 1826–1830, 1999.

[167] A. Majumdar, E. D. Kim, and J. Vučković, "Effect of photogenerated carriers on the spectral diffusion of a quantum dot coupled to a photonic crystal cavity," *Physical Review B*, vol. 84, p. 195304, Nov 2011.

[168] P. Borri, W. Langbein, S. Schneider, U. Woggon, R. L. Sellin, D. Ouyang, and D. Bimberg, "Ultralong dephasing time in ingaas quantum dots," *Physical Review Letters*, vol. 87, p. 157401, Sep 2001.

[169] G. Sallen, A. Tribu, T. Aichele, R. André, L. Besombes, C. Bougerol, M. Richard, S. Tatarenko, K. Kheng, and J.-P. Poizat, "Subnanosecond spectral diffusion measurement using photon correlation," *Nature Photonics*, vol. 4, pp. 696–699, 2010.

[170] M. J. Fernée, T. Plakhotnik, Y. Louyer, B. N. Littleton, C. Potzner, P. Tamarat, P. Mulvaney, and B. Lounis, "Spontaneous spectral diffusion in cdse quantum dots," *The Journal of Physical Chemistry Letters*, vol. 3, no. 12, pp. 1716–1720, 2012.

[171] I. Sychugov, J. Valenta, K. Mitsuishi, and J. Linnros, "Exciton localization in doped si nanocrystals from single dot spectroscopy studies," *Physical Review B*, vol. 86, p. 075311, Aug 2012.

[172] J. Valenta, A. Fucikova, F. Vácha, F. Adamec, J. Humpolíčková, M. Hof, I. Pelant, K. Kůsová, K. Dohnalová, and J. Linnros, "Light-emission performance of silicon nanocrystals deduced from single quantum dot spectroscopy," *Advanced Functional Materials*, vol. 18, no. 18, pp. 2666–2672, 2008.

[173] J. D. Suter, I. M. White, H. Zhu, and X. Fan, "Thermal characterization of liquid core optical ring resonator sensors," *Applied Optics*, vol. 46, pp. 389–396, Jan 2007.

[174] J. Müller, J. M. Lupton, A. L. Rogach, J. Feldmann, D. V. Talapin, and H. Weller, "Monitoring surface charge migration in the spectral dynamics of single CdSe/CdS nanodot/nanorod heterostructures," *Physical Review B*, vol. 72, p. 205339, Nov 2005.

[175] H. Yukawa, S. Arnold, and K. Miyano, “Microcavity effect of dyes adsorbed on a levitated droplet,” *Physical Review A*, vol. 60, pp. 2491–2496, Sep 1999.

[176] K. Matsuda, T. Saiki, H. Saito, and K. Nishi, “Room-temperature photoluminescence spectroscopy of self-assembled $In_{0.5}Ga_{0.5}As$ single quantum dots by using highly sensitive near-field scanning optical microscope,” *Applied Physics Letters*, vol. 76, no. 1, pp. 73–75, 2000.

[177] H. Chen, J.-Y. Sung, A. Tewary, M. Brongersma, J.-H. Shin, and P. Fauchet, “Evidence for stimulated emission in silicon nanocrystal microspheres,” in *Group IV Photonics, 2005. 2nd IEEE International Conference on*, pp. 99–101, Sept 2005.

[178] J. Ruan, P. M. Fauchet, L. Dal Negro, M. Cazzanelli, and L. Pavesi, “Stimulated emission in nanocrystalline silicon superlattices,” *Applied Physics Letters*, vol. 83, no. 26, pp. 5479–5481, 2003.

[179] T. Ioppolo and M. V. Ötügen, “Pressure tuning of whispering gallery mode resonators,” *Journal of the Optical Society of America B*, vol. 24, pp. 2721–2726, Oct 2007.

[180] T. Ioppolo, M. Kozhevnikov, V. Stepaniuk, M. V. Ötügen, and V. Sheverev, “Micro-optical force sensor concept based on whispering gallery mode resonators,” *Applied Optics*, vol. 47, pp. 3009–3014, Jun 2008.

[181] F. Vollmer and L. Yang, “Review label-free detection with high-Q microcavities: a review of biosensing mechanisms for integrated devices,” *Nanophotonics*, vol. 1, no. 3-4, pp. 267–291, 2012.

[182] D. V. Strekalov, R. J. Thompson, L. M. Baumgartel, I. S. Grudinin, and N. Yu, “Temperature measurement and stabilization in a birefringent whispering gallery mode resonator,” *Optics Express*, vol. 19, pp. 14495–14501, Jul 2011.

[183] B. Özel, R. Nett, T. Weigel, G. Schweiger, and A. Ostendorf, “Temperature sensing by using whispering gallery modes with hollow core fibers,” *Measurement Science and Technology*, vol. 21, no. 9, p. 094015, 2010.

[184] A. Chiba, H. Fujiwara, J. ichi Hotta, S. Takeuchi, and K. Sasaki, “Resonant frequency control of a microspherical cavity by temperature adjustment,” *Japanese Journal of Applied Physics*, vol. 43, no. 9R, p. 6138, 2004.

[185] C.-H. Dong, L. He, Y.-F. Xiao, V. R. Gaddam, S. K. Ozdemir, Z.-F. Han, G.-C. Guo, and L. Yang, "Fabrication of high-Q polydimethylsiloxane optical microspheres for thermal sensing," *Applied Physics Letters*, vol. 94, no. 23, p. 231119, 2009.

[186] L. L. Martín, C. Pérez-Rodríguez, P. Haro-González, and I. R. Martín, "Whispering gallery modes in a glass microsphere as a function of temperature," *Optics Express*, vol. 19, pp. 25792–25798, Dec 2011.

[187] F. Vollmer and S. Roy, "Optical resonator based biomolecular sensors and logic devices," *Journal of the Indian Institute of Science*, vol. 92, no. 2, pp. 233–251, 2012.

[188] F. Vollmer, S. Arnold, and D. Keng, "Single virus detection from the reactive shift of a whispering-gallery mode," *Proceedings of the National Academy of Sciences*, vol. 105, no. 52, pp. 20701–20704, 2008.

[189] A. Francois and M. Himmelhaus, "Optical biosensor based on whispering gallery mode excitations in clusters of microparticles," *Applied Physics Letters*, vol. 92, no. 14, p. 141107, 2008.

[190] A. Weller, F. Liu, R. Dahint, and M. Himmelhaus, "Whispering gallery mode biosensors in the low-q limit," *Applied Physics B*, vol. 90, no. 3-4, pp. 561–567, 2008.

[191] E. Nuhiji and P. Mulvaney, "Detection of unlabeled oligonucleotide targets using whispering gallery modes in single, fluorescent microspheres," *Small*, vol. 3, no. 8, pp. 1408–1414, 2007.

[192] P. Zijlstra, K. L. van der Molen, and A. P. Mosk, "Spatial refractive index sensor using whispering gallery modes in an optically trapped microsphere," *Applied Physics Letters*, vol. 90, no. 16, p. 161101, 2007.

[193] D. E. Gómez, I. Pastoriza-Santos, and P. Mulvaney, "Tunable whispering gallery mode emission from quantum-dot-doped microspheres," *Small*, vol. 1, no. 2, pp. 238–241, 2005.

[194] N. Lin, L. Jiang, S. Wang, H. Xiao, Y. Lu, and H.-L. Tsai, "Design and optimization of liquid core optical ring resonator for refractive index sensing," *Applied Optics*, vol. 50, pp. 3615–3621, Jul 2011.

[195] G. Guan, S. Arnold, and V. Otugen, “Temperature measurements using a microoptical sensor based on whispering gallery modes,” *AIAA Journal*, vol. 44, pp. 2385–2389, Oct. 2006.

[196] M. R. Foreman, W.-L. Jin, and F. Vollmer, “Optimizing detection limits in whispering gallery mode biosensing,” *Optics Express*, vol. 22, pp. 5491–5511, Mar 2014.

[197] A. Chijioke, Q.-F. Chen, A. Y. Nevsky, and S. Schiller, “Thermal noise of whispering-gallery resonators,” *Physical Review A*, vol. 85, p. 053814, May 2012.

[198] T. Carmon, L. Yang, and K. Vahala, “Dynamical thermal behavior and thermal self-stability of microcavities,” *Optics Express*, vol. 12, pp. 4742–4750, Oct 2004.

[199] I. Teraoka, “Analysis of thermal stabilization of whispering gallery mode resonance,” *Optics Communications*, vol. 310, no. 0, pp. 212–216, 2014.

[200] B. Guha, J. Cardenas, and M. Lipson, “Athermal silicon microring resonators with titanium oxide cladding,” *Optics Express*, vol. 21, pp. 26557–26563, Nov 2013.

[201] F. Michelotti and E. Descrovi, “Temperature stability of bloch surface wave biosensors,” *Applied Physics Letters*, vol. 99, no. 23, p. 231107, 2011.

[202] L. M. Baumgartel, R. J. Thompson, and N. Yu, “Frequency stability of a dual-mode whispering gallery mode optical reference cavity,” *Optics Express*, vol. 20, pp. 29798–29806, Dec 2012.

[203] S.-Y. Seo, J. Lee, J. H. Shin, E.-S. Kang, and B.-S. Bae, “The thermo-optic effect of Si nanocrystals in silicon-rich silicon oxidethin films,” *Applied Physics Letters*, vol. 85, no. 13, pp. 2526–2528, 2004.

[204] Y. Zhi, J. Valenta, and A. Meldrum, “Structure of whispering gallery mode spectrum of microspheres coated with fluorescent silicon quantum dots,” *Journal of the Optical Society of America B*, vol. 30, pp. 3079–3085, Nov 2013.

[205] P. V. Lambeck, “Integrated optical sensors for the chemical domain,” *Measurement Science and Technology*, vol. 17, no. 8, p. R93, 2006.

[206] K. E. Herold and A. Rasooly, *Lab-on-a-Chip Technology (Vol. 1): Fabrication and Microfluidics.* Caister Academic Press, 2009.

[207] “http://www.biacore.com/lifesciences/index.html.”

[208] H. N. Daghestani and B. W. Day, “Theory and applications of surface plasmon resonance, resonant mirror, resonant waveguide grating, and dual polarization interferometry biosensors,” *Sensors*, vol. 10, no. 11, pp. 9630–9646, 2010.

[209] F. Vollmer and S. Arnold, “Whispering-gallery-mode biosensing: label-free detection down to single molecules,” *Nature Methods*, vol. 5, no. 7, pp. 591–596, 2008.

[210] J. Yang and L. Guo, “Optical sensors based on active microcavities,” *Selected Topics in Quantum Electronics, IEEE Journal of*, vol. 12, pp. 143–147, Jan 2006.

[211] B. P. N. Jennifer M. Brockman and R. M. Corn, “Surface plasmon resonance imaging measurements of ultrathin organic film,” *Annual Review of Physical Chemistry*, vol. 51, pp. 41–63, 2000.

[212] J. H. Warner, A. Hoshino, K. Yamamoto, and R. D. Tilley, “Water-soluble photoluminescent silicon quantum dots,” *Angewandte Chemie International Edition*, vol. 44, no. 29, pp. 4550–4554, 2005.

[213] P. Bianucci, J. R. Rodríguez, F. C. Lenz, J. G. C. Veinot, and A. Meldrum, “Mode structure in the luminescence of Si-nc in cylindrical microcavities,” *Physica E Low-Dimensional Systems and Nanostructures*, vol. 41, pp. 1107–1110, may 2009.

[214] A. V. Boriskin, S. V. Boriskina, A. Rolland, R. Sauleau, and A. I. Nosich, “Test of the fdtd accuracy in the analysis of the scattering resonances associated with high-Q whispering-gallery modes of a circular cylinder,” *Journal of the Optical Society of America A*, vol. 25, pp. 1169–1173, May 2008.

[215] I. M. White and X. Fan, “On the performance quantification of resonant refractive index sensors,” *Optics Express*, vol. 16, pp. 1020–1028, Jan 2008.

[216] N. Lomb, “Least-squares frequency analysis of unequally spaced data,” *Astrophysics and Space Science*, vol. 39, no. 2, pp. 447–462, 1976.

[217] A. A. Mrinal Mandal, *Continuous and discrete time signals and systems.* Cambridge University Press, Cambridge, 2007.

[218] R. P. W. Scott, “The thermodynamic properties of methanol-water association and its effect on solute retention in liquid chromatography,” *Analyst*, vol. 125, pp. 1543–1547, 2000.

[219] D. R. Lide, ed., *The CRC handbook of chemistry and physics.* CRC Press, New York, 2005.

[220] H. El-Kashef, “The necessary requirements imposed on polar dielectric laser dye solvents,” *Physica B: Condensed Matter*, vol. 279, no. 4, pp. 295–301, 2000.

[221] M. Daimon and A. Masumura, “Measurement of the refractive index of distilled water from the near-infrared region to the ultraviolet region,” *Applied Optics*, vol. 46, pp. 3811–3820, Jun 2007.

[222] J. Herráez and R. Belda, “Refractive indices, densities and excess molar volumes of monoalcohols + water,” *Journal of Solution Chemistry*, vol. 35, no. 9, pp. 1315–1328, 2006.

[223] L. Hao and D. G. Leaist, “Binary mutual diffusion coefficients of aqueous alcohols. methanol to 1-heptanol,” *Journal of Chemical & Engineering Data*, vol. 41, no. 2, pp. 210–213, 1996.

[224] S. McFarlane, C. P. K. Manchee, J. W. Silverstone, J. G. C. Veinot, and A. Meldrum, “Feasibility of a fluorescent-core microcapillary for biosensing applications,” *Sensor Letters*, vol. 11, no. 8, pp. 1513–1518, 2013.

[225] H. Stone, A. Stroock, and A. Ajdari, “Engineering flows in small devices,” *Annual Review of Fluid Mechanics*, vol. 36, no. 1, pp. 381–411, 2004.

[226] M. A. Dittrich, Petra S., “Lab-on-a-chip: microfluidics in drug discovery,” *Nature Reviews Drug Discovery*, vol. 5, no. 3, pp. 210–218, 2006.

[227] D. Mark, S. Haeberle, G. Roth, F. von Stetten, and R. Zengerle, “Microfluidic lab-on-a-chip platforms: requirements, characteristics and applications,” *Chemical Society Reviews*, vol. 39, pp. 1153–1182, 2010.

[228] Y. Zou, S. Chakravarty, W.-C. Lai, C.-Y. Lin, and R. T. Chen, “Methods to array photonic crystal microcavities for high throughput high sensitivity biosensing on a silicon-chip based platform,” *Lab Chip*, vol. 12, pp. 2309–2312, 2012.

[229] I. M. White, H. Oveys, and X. Fan, “Liquid-core optical ring-resonator sensors,” *Optics Letters*, vol. 31, pp. 1319–1321, May 2006.

[230] S. Yegnanarayanan, W. Roman, M. Soltani, G. Cremona, H. Lu, and A. Adibi, “On-chip integration of microfluidic channels with ultra-high Q silicon microdisk resonators for lab-on-a-chip sensing applications,” in *Lasers and Electro-Optics Society, 2007. LEOS 2007. The 20th Annual Meeting of the IEEE*, pp. 50–51, Oct 2007.

[231] G.-D. Kim, G.-S. Son, H.-S. Lee, K.-D. Kim, and S.-S. Lee, “Refractometric sensor utilizing a vertically coupled polymeric microdisk resonator incorporating a high refractive index overlay,” *Optics Letters*, vol. 34, pp. 1048–1050, Apr 2009.

[232] T. Xu, N. Zhu, M. Y.-C. Xu, L. Wosinski, J. S. Aitchison, and H. E. Ruda, “Pillar-array based optical sensor,” *Optics Express*, vol. 18, pp. 5420–5425, Mar 2010.

[233] N. M. Hanumegowda, C. J. Stica, B. C. Patel, I. White, and X. Fan, “Refractometric sensors based on microsphere resonators,” *Applied Physics Letters*, vol. 87, no. 20, pp. 201107–201107–3, 2005.

[234] J. Lutti, W. Langbein, and P. Borri, “A monolithic optical sensor based on whispering-gallery modes in polystyrene microspheres,” *Applied Physics Letters*, vol. 93, no. 15, p. 151103, 2008.

[235] Y. Panitchob, G. S. Murugan, M. N. Zervas, P. Horak, S. Berneschi, S. Pelli, G. N. Conti, and J. S. Wilkinson, “Whispering gallery mode spectra of channel waveguide coupled microspheres,” *Optics Express*, vol. 16, pp. 11066–11076, Jul 2008.

[236] J. Lutti, W. Langbein, and P. Borri, “High Q optical resonances of polystyrene microspheres in water controlled by optical tweezers,” *Applied Physics Letters*, vol. 91, no. 14, p. 141116, 2007.

[237] S. Arnold, M. Khoshsima, I. Teraoka, S. Holler, and F. Vollmer, “Shift of whispering-gallery modes in microspheres by protein adsorption,” *Optics Letters*, vol. 28, pp. 272–274, Feb 2003.

[238] G. Conti, S. Berneschi, F. Cosi, S. Pelli, S. Soria, G. Righini, P. H. Merrer, M. Dispenza, and A. Secchi, “Coupling of angle polished waveguides to high-q whispering gallery mode resonators,” in *Lasers and Electro-Optics Europe (CLEO EUROPE/EQEC), 2011 Conference on and 12th European Quantum Electronics Conference*, pp. 1–1, May 2011.

[239] X. Fan, P. Palinginis, S. Lacey, H. Wang, and M. C. Lonergan, "Coupling semiconductor nanocrystals to a fused-silica microsphere: a quantum-dot microcavity with extremely high q factors," *Optics Letters*, vol. 25, pp. 1600–1602, Nov 2000.

[240] P. Bianucci, J. R. Rodríguez, C. Clements, C. M. Hessel, J. G. C. Veinot, and A. Meldrum, "Whispering gallery modes in silicon nanocrystal coated microcavities," *physica status solidi (a)*, vol. 206, no. 5, pp. 973–975, 2009.

[241] C. M. Hessel, E. J. Henderson, and J. G. C. Veinot, "An investigation of the formation and growth of oxide-embedded silicon nanocrystals in hydrogen silsesquioxane-derived nanocomposites," *The Journal of Physical Chemistry C*, vol. 111, no. 19, pp. 6956–6961, 2007.

[242] A. Meldrum, A. Hryciw, A. N. MacDonald, C. Blois, K. Marsh, J. Wang, and Q. Li, "Photoluminescence in the silicon-oxygen system," *Journal of Vacuum Science & Technology A*, vol. 24, no. 3, pp. 713–717, 2006.

[243] L. Ferraioli, M. Wang, G. Pucker, D. Navarro-Urrios, N. Daldosso, C. Kompocholis, and L. Pavesi, "Photoluminescence of silicon nanocrystals in silicon oxide," *Journal of Nanomaterials*, vol. 2007, p. 43491, 2007.

[244] X. Zhang, L. Liu, and L. Xu, "Ultralow sensing limit in optofluidic micro-bottle resonator biosensor by self-referenced differential-mode detection scheme," *Applied Physics Letters*, vol. 104, no. 3, p. 033703, 2014.

[245] J. Knittel, J. Swaim, and W. Bowen, "A self-referencing detection technique for whispering gallery mode biosensors," in *Lasers and Electro-Optics Europe (CLEO EUROPE/EQEC), 2011 Conference on and 12th European Quantum Electronics Conference*, pp. 1–1, May 2011.

[246] "http://www.biacore.com/lifesciences/index.html."

[247] I. Abdulhalim, M. Zourob, and A. Lakhtakia, "Surface plasmon resonance for biosensing: A mini-review," *Electromagnetics*, vol. 28, no. 3, pp. 214–242, 2008.

[248] J. Homola, "Surface plasmon resonance sensors for detection of chemical and biological species," *Chemical Reviews*, vol. 108, no. 2, pp. 462–493, 2008.

[249] P. Preechaburana, M. C. Gonzalez, A. Suska, and D. Filippini, "Surface plasmon resonance chemical sensing on cell phones," *Angewandte Chemie International Edition*, vol. 51, no. 46, pp. 11585–11588, 2012.

[250] K. M. Mayer, F. Hao, S. Lee, P. Nordlander, and J. H. Hafner, “A single molecule immunoassay by localized surface plasmon resonance,” *Nanotechnology*, vol. 21, no. 25, p. 255503, 2010.

[251] S. Arnold, V. R. Dantham, C. Barbre, B. A. Garetz, and X. Fan, “Periodic plasmonic enhancing epitopes on a whispering gallery mode biosensor,” *Optics Express*, vol. 20, pp. 26147–26159, Nov 2012.

[252] S. Arnold, D. Keng, S. I. Shopova, S. Holler, W. Zurawsky, and F. Vollmer, “Whispering gallery mode carousel – a photonic mechanism for enhanced nanoparticle detection in biosensing,” *Optics Express*, vol. 17, pp. 6230–6238, Apr 2009.

Appendix

Publications:

1. Y. Zhi, C. Manchee, J. Silverstone, Z. Zhang, and A. Meldrum, "Refractometric sensing with silicon quantum dots coupled to a microsphere," *Plasmonics,* vol. 8, no. 1, pp. 71-78, 2013.
2. Y. Zhi, J. Valenta, and A. Meldrum, "Structure of whispering gallery mode spectrum of microspheres coated with fluorescent silicon quantum dots," *Journal of the Optical Society of America B,* vol. 30, pp. 3079-3085, Nov 2013.
3. Y. Zhi, T. Thiessen, and A. Meldrum, "Silicon quantum dot coated microspheres for microfluidic refractive index sensing," *Journal of the Optical Society of America B,* vol. 30, pp. 51-56, Jan 2013.
4. Y. Zhi and A. Meldrum, "Tuning a microsphere whispering-gallery-mode sensor for extreme thermal stability," *Applied Physics Letters,* vol. 105, no. 3, p. 031902, 2014.
5. Y. Zhi and A. Meldrum, "Resonance structure of quantum-dot-coated microspheres for microfluidic sensing," *the proceedings of the SPIE,* vol. 9288, p. 92880Y, 2014.
6. P. Bianucci, Y. Zhi, F. Marsiglio, J. Silverstone, and A. Meldrum, "Microcavity effects in ensembles of silicon quantum dots coupled to high-q resonators," *physica status solidi (a),* vol. 208, no. 3, pp. 639-645, 2011.
7. Z. Yang, M. Dasog, A. R. Dobbie, R. Lockwood, Y. Zhi, A. Meldrum, and J. G. C. Veinot, "Highly luminescent covalently linked silicon Nanocrystal/Polystyrene hybrid functional materials: Synthesis, properties, and processability," *Advanced Functional Materials,* vol. 24, no. 10, pp. 1345-1353, 2014.

Submitted manuscripts:

1. S. Lane, F. Marsiglio, Y. Zhi, and A. Meldrum, "Refractometric sensitivity and thermal stabilization of fluorescent core microcapillary sensors: theory and experiment," *Applied Optics,* 2014. (submitted).